A wealth of interacting galaxies in the interacting cluster A2670

Franco Camilo Piraino Cerda

Instituto de Física y Astronomía
Facultad de Ciencias

Universidad de Valparaíso
Magíster en Astrofísica

Marzo 2023
Valparaíso. Chile.

..... for my father.

This thesis is solely my own composition,

except where specifically indicated in the text.

Total or partial reproduction, for scientific or academic purposes,
is authorised including a bibliographic reference to this documment.

Franco Camilo Piraino Cerda
Marzo 2023.
Valparaíso. Chile.

Acknowledgements

I would really like to acknowledge my supervisor, Dr. Yara Jaffé, for her extraordinary guidance throughout my time at UV. I'm grateful to the people from the jellyfish group at UV for advising me during this work and for taking the time to participate in the classification of interacting galaxies and the measurement of the jellyfish galaxy tails. I deeply appreciate Dr. Yun-Kyeong Sheen and Dr. Duho Kim for their enthusiasm to collaborate with us on this project and provide us their catalogue for the cluster A2670. Special thanks to Dr. Jacob Crossett for sharing the initial tail classification script and Ana Lourenço for helping us with the substructure analyses and providing us the X-ray morphology contours from Chandra. I am also grateful to the thesis committee composed by Dr. Patricia Arévalo and Dr. Sergio Torres for the revision and for their useful comments on the manuscript. I would also like to acknowledge my family, in particular, my parents and brothers to support my career. Acknowledgments for the availability of catalogs from SDSS and Legacy Surveys DR9.

Abstract

Galaxy clusters are among the largest and most massive known gravitationally bound structures in the Universe, that continue growing through the accretion of galaxies from field, groups and even other clusters. It is thus expected that the evolution of galaxies depends on interactions with their evolving environments and that cluster mergers accelerate galaxy evolution as they present violent environments where ram-pressure and galaxy-galaxy interactions can be enhanced.

To understand how galaxies evolve across cosmic environment, we study in great detail the growth of the interacting system A2670, a massive nearby galaxy cluster (M_{200} = 8.5 ± $1.2 \times 10^{14} M_{\odot}$, z = 0.0763, R_{200} = 1.91 ± 0.1 Mpc), with clear evidences of past interactions. We built a complete and homogeneous photometric catalogue using public data from Legacy Survey (LS) DR9 for galaxies within the cluster and out to its infall region ($5 \times R_{200}$) and public spectroscopic data from Sloan Digital Sky Survey (SDSS) were also collected, available for some galaxies in this large area explored. We use 2D and 3D methods to identify substructures using the positions collected and velocities when these were available.

We find a wealth of substructures, including the main cluster core, a large infalling group at the same velocity and several other smaller substructures. Then, to study the impact of these substructures on the evolution of member galaxies, we visually examine the optical morphologies of 843 galaxies brighter than $M_r = -20$ in and around the cluster through custom-made codes and algorithms. We found 236 interacting galaxies, with $\sim 42 - 63\%$ of those being ram-pressure stripping (RPS) candidates and $\sim 31 - 37\%$ possible gravitational interactions (GRAV). Interestingly, the interacting galaxies follow the substructures found, with the richest structures having more interacting galaxies, with a mild indication that RPS is dominant at the cluster core but also clearly present at the outskirts, close to $5 \times R_{200}$. Overall, the fraction of RPS candidates found is the largest to date for a single system, making A2670 a unique environment to study pre and post-processing.

Finally, we measured the visible tails angle in RPS candidates (a.k.a "jellyfish" galaxies) to use it as a proxy of the direction of motion. We find a not as clear trend as seen in regular clusters, likely due to the combined effect of pre- and post-processing, revealing a complex dynamical behavior, with a mixture of radial and non-radial infall into the main cluster.

Contents

Chapter 1

Introduction

1.1 Galaxy Evolution Scenarios

Galaxies have been classified according to their different shapes and morphology, e.g. (Hubble 1936, Fig. 1.1 Hubble's 'tuning fork' Adapted from: (Kormendy & Bender, 1996)), indicating a large morphological segregation among the different population of galaxies, however those classifications are not enough to explain other kind of galaxies whose morphology is out of the ordinary, going together with an extreme formation and evolution. However, some signatures in their star formation rate can give us some ideas of the evolution and formation of those galaxies. The Hubble's classification suggests two clear populations of galaxies according to its morphology. On one side, we can find spiral galaxies (S), often referred to as late-type galaxies, rich in gas and actively star-forming. On the other side, we have elliptical galaxies (E), generally early-type galaxies, poor in gas and without star formation in course. In a color magnitude diagram, late-type galaxies, tend to located in a "blue cloud" and early type galaxies tend to form a "red sequence" along the luminosity or mass axis (see Figure 1.2), (Kormendy & Bender, 2012). Essentially, we should consider these populations as two points of galaxy evolution, where a transition from the "blue cloud" to the "red sequence" is suggested for those galaxies that are experiencing a star formation quenching, passing first through a transition region located between these two populations (known as the "green valley"), dominated generally by lenticular galaxies (S0 in Hubble's "tuning fork") that exhibits properties intermediate between blue cloud and red sequence galaxies.

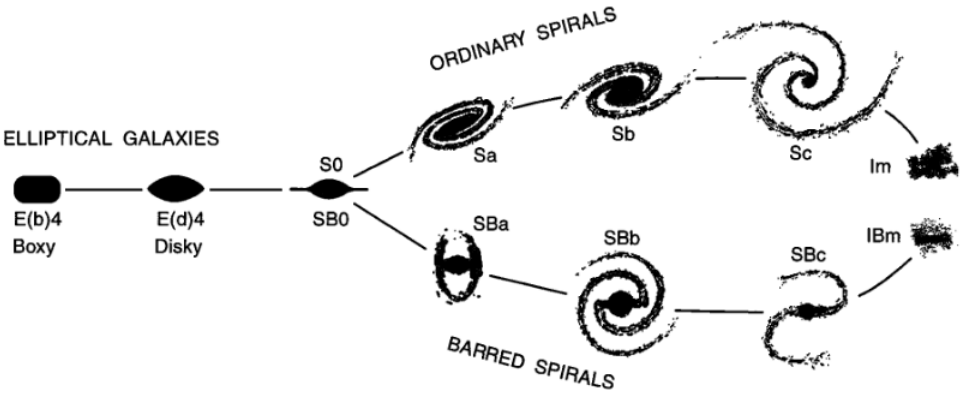

Figure 1.1: Morphological scheme classification provided by Hubble's 'tuning fork'. Adapted from: (Kormendy & Bender, 1996))

Understanding the main ways of the formation and evolution of galaxies and the main mechanisms of star formation quenching with those transitions seen in Figure 1.2, have been one the most important challenges for the astronomers through the years. This discussion could be summarized in only one question: nature or nurture? (Peng et al., 2010) This put on the table the debate about if the formation and evolution of the galaxies can be determined by internal processes within the galaxies (nature) or by different interaction mechanisms with the environment during their life (nurture) (Boselli & Gavazzi, 2006). On one hand, there are several physical mechanisms that drive the star formation quenching when nature is involved. The internal feedback related to the star-formation process that removes cold ISM from galaxies is often described via supernova feedback or to the presence of an active galactic nucleus (AGN) at the centre of galaxies (Cortese et al., 2021). In both cases, cold gas could be ejected from the disk and/or heated up, becoming unavailable for star formation.

On the other hand, many physical mechanisms have been proposed to explain the star formation quenching evolution and the sudden morphological change of the galaxies because of extreme environments. The environment is very important, mainly in less massive galaxies, as we see in Figure 1.3 (LEFT, Goto et al., 2003), where the fraction of types of galaxies according their morphology has a significant dependence on local densities within clusters. For example, for the late-type spiral galaxies (Sc) it can be seen that the fraction of these galaxies has a notable decrease in high local densities. On the other hand, for E type galaxies, it is observed that in regions of high density of galaxies the fraction of these is increasing. Within the density-morphology relationship, the fraction of galaxies presents a strong dependence as a function of the radius of the cluster (Figure 1.3 RIGHT). Keeping in mind the distance to the center of the cluster (R/R_{virial}), E type galaxies present a clear increase in the fraction

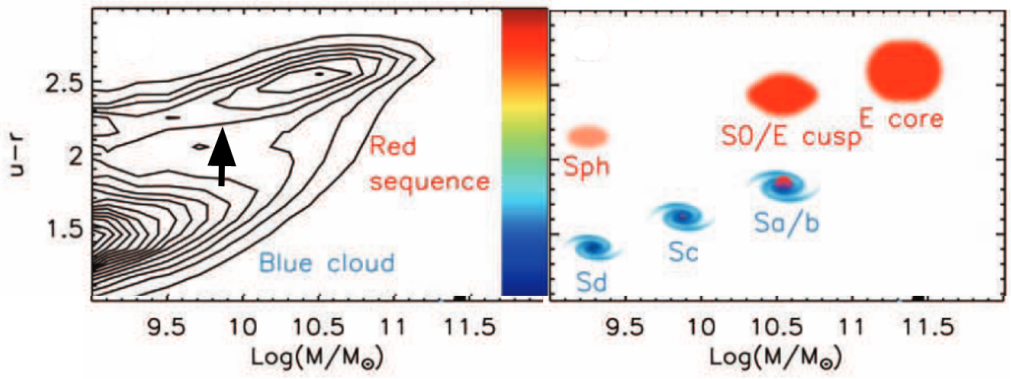

Figure 1.2: Left: It shows the narrow "red sequence" of mostly-non-star-forming galaxies and the broader "blue cloud" of actively-star-forming galaxies. **Right:** It shows some morphological types from Figure 1.1 that dominate in various parts of the left panel. Adapted from (Kormendy & Bender, 2012)

when we approach to the center. It is interesting to emphasize a mutual dependence of these relationships, where E-type galaxies present an increase in fraction at higher local densities and at low R/R_{virial} distances, implying that the fraction of E-type galaxies is very high dense in places near the center of the clusters. If we restrict ourselves to distances very close to the center, such as $R \lesssim 0.3R_{\text{virial}}$, due to morphological transformations from lenticular to elliptical, we see a strong decrease and increase of S0 and E, respectively. The change of the fraction of galaxies in function of cluster centre distance and galaxy density seem to be correlated with processes of star formation quenching. In the same way that the transition from late-type galaxies (blue) to early-type galaxies (red), as we saw in CMD from Figure 1.2, several interaction mechanisms with the environment, could allow star-forming galaxies such as spiral galaxies to evolve to S0 type galaxies and then to become E type galaxies.

The main physical mechanisms where the environment is involved, can be divided into two main categories: **(1) gravitational** and **(2) hydrodynamical**. Both purely gravitational interactions that affect all the components of the galaxies and hydrodynamical that affect only the gas, change dramatically the morphology and physical properties of the galaxies and could be the most likely path to the formation of normal elliptical galaxies, that we found in the inner part of galaxy clusters. As previously stated, the fraction of E-type galaxies can become very dense in places close to the center of the cluster, which suggests that Sc-type galaxies in external regions lose part of their gas during their trajectory towards the center.

Examples for the **first category** can be:

- **Galaxy merger:** Strong ongoing mergers between galaxies of similar masses resulting in a very disturbed system. During a merger, dissipation in gas and ensuing star formation

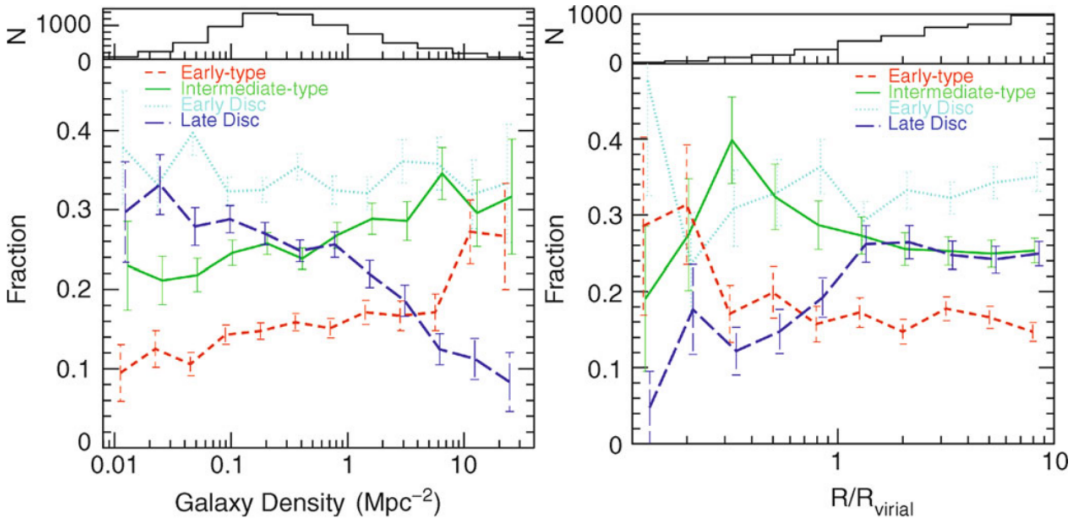

Figure 1.3: The numerical fraction of galaxies of different morphologies is plotted as a function of local galaxy density (left panel), and as a function of distance from the cluster center (right panel) ($R/R_{\rm virial}$) (Goto et al., 2003)

leave behind a dense stellar core in the remnant (Mihos & Hernquist, 1994). Mergers of gas-rich disk galaxies may not have contributed greatly to the population of present-day ellipticals. However, lenticular galaxies with intermediate bulge-to-disk ratios, can be formed from the merging of two equal-mass galaxies (where the subsequent gas cooling forms disks; (Diaferio et al., 2001)), by unequal-mass mergers of disk galaxies (where disk destruction is not complete and some rotation is retained), or by minor mergers between spirals and their companions (the disk is heated but not destroyed). Galaxy mergers are relatively rare and unlikely to happen in rich clusters (Makino & Hut, 1997) where velocities are too high.

- **Tidal interactions:** Tidal interactions among galaxy pairs act on gas, dust, and stars, as well as on dark matter, with an efficiency depending on the gravitational bounding of the various components. This produces selective morphological transformations (Boselli & Gavazzi, 2006). Since tidal forces act as M/R^3 , if the typical galaxy radii are not too small compared to the average separation between galaxies, tidal interactions can be quite efficient at removing matter from galactic halos (Spitzer & Baade, 1951; Farouki & Shapiro, 1981). It is expected that the frequency of these interactions is higher in clusters (Binney & Tremaine, 1987), although the high relative velocities of cluster galaxies make the encounters rather short.

- **Harassment:** Proposed by (Moore et al., 1996, 1998, 1999), the evolution of the galaxies

is governed through the accumulation of several high speed encounters and the interaction with the potential of clusters. The observable effect in these mechanisms is an increasing of the velocity dispersion and decreasing the angular momentum; meanwhile, they cause the gas to sink toward the galaxy center because of the multiple high velocity encounters.

Examples for the **second category** can be:

- **Ram-pressure stripping:** It is expected to be one of the most dominant mechanisms within clusters, responsible for removing the cold gas from the Interstellar medium (ISM) located in the galactic disc in their first fall toward the clusters (Cortese et al., 2021; Jaffé et al., 2015). According to (Gunn & Gott, 1972), galaxies may lose the ISM while falling into a cluster when the ram pressure from the intracluster medium (ICM) exceeds the anchoring pressure by the potential of a galaxy.

$$\rho_{\rm IGM} V_{\rm gal}^2 \geq 2\pi G \Sigma_{\rm star} \Sigma_{\rm gas} \tag{1.1}$$

  where $\rho_{\rm ICM}$ is the ICM density, $V_{\rm gal}$ is the galaxy velocity inside the cluster, $\Sigma_{\rm star}$ is the star surface density, and $\Sigma_{\rm gas}$ is the gas surface density.

  These interactions only affect the gas in the galaxy, as convincingly shown by HI observations of cluster galaxies (Chung et al., 2009). The gas stripping can sometimes lead to star-formation in the striped gas, giving rise to the spectacular "jellyfish" galaxies observed in Optical/UV wavelengths (Smith et al., 2010; Ebeling et al., 2014; Fumagalli et al., 2014; Poggianti et al., 2016, 2017). After the stripping phase, the galaxies are expected to become quenched (Jaffé et al., 2016; Vulcani et al., 2020). In particular, RPS can remove a significant amount of gas from cluster galaxies early, on during the first infall into the cluster (Jaffé et al., 2015), particularly for radially infalling galaxies (Jaffé et al., 2018, 2019). In support of the key role of RPS in clusters, recent studies have shown that a significant fraction of the star-forming galaxies inside clusters have "jellyfish" morphology (up to ∼35% Vulcani et al., 2022), which indicates they are in transition to become gas-poor, passive galaxies. Milder and less frequent cases of RPS galaxies have also been found in groups and perhaps even filaments (Roberts et al., 2021; Vulcani, 2021; Kolcu et al., 2022).

- **Starvation/strangulation:** Removal of the gas that comes from an extended gas reservoir quenching their star formation activity. Process proposed to explain the transformation of spiral galaxies into lenticulars (Larson et al., 1980).

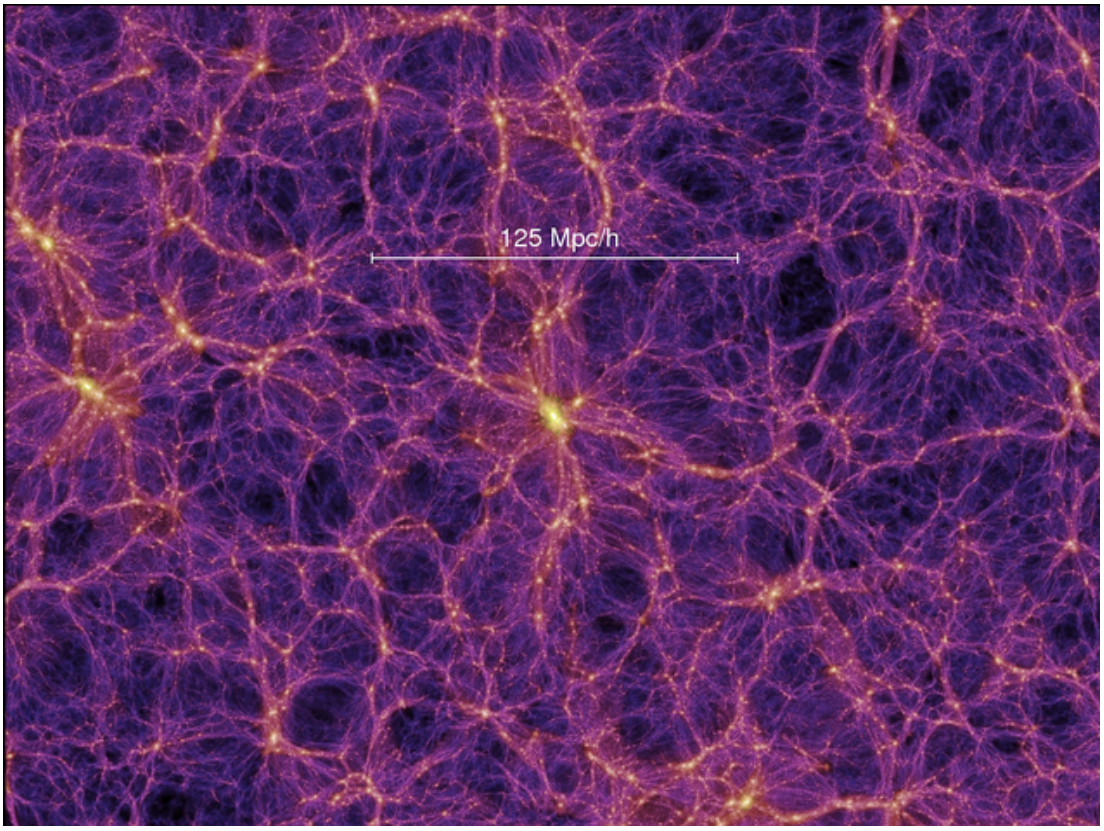

Figure 1.4: Simulation of the dark matter distribution. Clusters grow from a continuous accretion of galaxies from filaments, groups and even other clusters. Credit: Millennium Simulation

1.2 Pre and post processing

In order to study all of those interaction mechanisms, galaxy clusters are one of the largest and most massive known gravitationally bound structures in the Universe that give an ideal laboratory to probe the galaxy evolution driven by their extreme environmental, product of their continuum growing through the accretion of galaxies that fall from the filaments, groups and even other clusters. The accretion of galaxies into cluster seem to be the responsible mechanism of growing the riches of the current clusters and the formation of large-scale structures that intersect between filaments forming the cosmic web, as we can appreciate in simulations like the one in Figure 1.4 where the matter flows along these filaments converging in nodes of high luminosity where these galaxy cluster are formed. Galaxies thus evolve within an evolving environment, transitioning from lower to higher density environments such as voids, filaments, and groups before eventually falling into clusters. This implies that galaxies can be "*pre-processed*" (i.e. start to quench and transform) in some of these intermediate environments before they reach the cluster (Fujita, 2004). Simulations indeed show that ~40

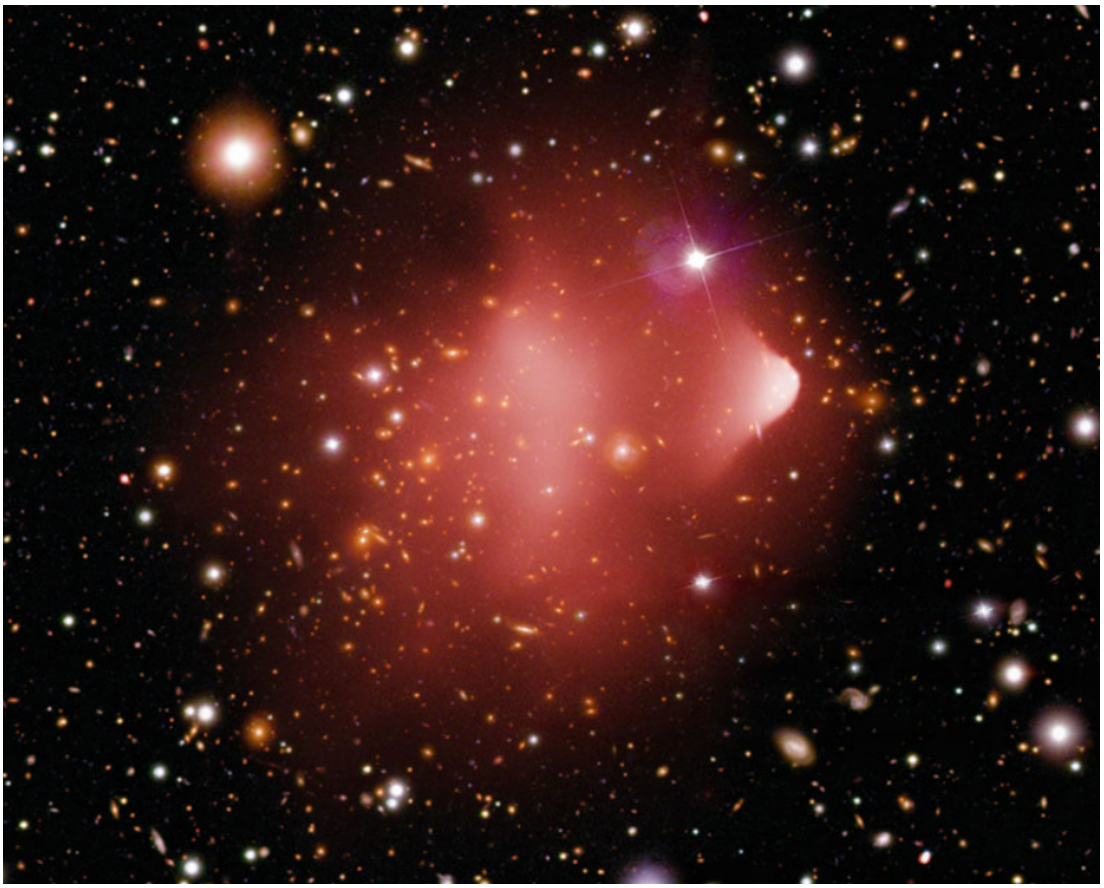

Figure 1.5: The cluster of galaxies 1E 0657-56 is a perfect example of a merging cluster. The X-ray emission of this cluster as observed by Chandra, shown in red, is superposed on an optical HST image. The most remarkable feature in the X-ray map is the compact region to the right (westwards) of the cluster center (from which the cluster derives its name the 'Bullet cluster'), and the sharp transition in the surface brightness further at its right edge. An analysis of the brightness profile and of the X-ray temperature distribution shows that this must be a shock front moving at about 2.5 times the speed of sound, or $v \sim 3500 km/s$, through the gas. To the right of this shock front, a group of galaxies is visible. Credit: X-ray: NASA/CXC/CfA/M. Markevitch et al.; Optical: NASA/STScI; Magellan/U.Arizona/D. (Clowe et al., 2004)

per cent of cluster galaxies today were previously in a group (McGee et al., 2009; Pallero et al., 2019, 2022), highlighting the need to take pre-processing into account. Supporting the pre-processing scenario, observational studies have reported a large fraction of galaxies undergoing transformations (e.g. starburst) or already passive galaxies in groups in and around clusters (Dressler, 2004; Cortese et al., 2006; Hou et al., 2014; Boselli et al., 2014; Jaffé et al., 2016). In addition, the fraction of star-forming galaxies in the field is significantly higher than that in cluster outskirts (at $\sim 3 \times R_{200}$; Haines et al., 2015; Bianconi et al., 2018), which indicates galaxies are processed in intermediate environments prior becoming cluster members. What has not been cleared yet is what physical mechanisms are responsible for such pre-processing.

In addition to the accretion of galaxies from filaments and groups, clusters can also grow via major mergers with other clusters. Approximately 10-20% of low-redshift clusters show evidence of having had a major merger in the past (Katayama et al., 2003; Sanderson et al., 2009; Hudson et al., 2010). Simulations predict an enhancement of gravitational and hydrodynamical interactions in cluster mergers which has been referred to as "*post-processing*" (Vijayaraghavan & Ricker, 2013).

Large mergers between clusters, like in Figure 1.5, have shown to be effective for events of post-processing, with violent and fast interactions of galaxies with the environment. However, there are not many observational studies on the post-processing of galaxies in cluster mergers and the ones that have attempted it often have contradicting conclusions (Fujita et al., 1999; Domainko et al., 2006; Kapferer et al., 2009; Hwang & Lee, 2009; Ma et al., 2010; Owers et al., 2012; Stroe et al., 2014; Rawle et al., 2014; Stroe et al., 2015; McPartland et al., 2016; Ebeling & Kalita, 2019; Kelkar et al., 2020). One interesting example supporting post-processing is the extremely high number of jellyfish galaxy candidates (70) in the A901/2 quadruple cluster system undergoing a merger (Roman-Oliveira et al., 2019; Ruggiero et al., 2019). However, a recent study attempting to quantify the fraction of jellyfish galaxies in a wide range of cluster dynamical stages found no clear evidence for an enhancement of RPS in cluster mergers (Lourenço et al. submitted), but note that their study is limited to an area $< R_{200}$.

In general, most observational studies of galaxy evolution in cluster regions are limited to the virial region or in some cases extend at most to 2-3$\times R_{200}$. The infall regions of clusters however are key for understanding galaxy evolution as they connect the cluster to the surrounding larger-scale structure. In fact, filaments and infalling groups are more easily detected in cluster outskirts (West & Bothun, 1990; Hou et al., 2012; Jaffé et al., 2013; Dressler et al., 2013). Moreover, hydrodynamical simulations of galaxies around massive clusters have demonstrated that environmental effects such as RPS could play a role in depleting both hot and cold gas in cluster galaxies out to $\sim 5 \times R_{200}$ (Bahé et al., 2013).

With the aim of better understanding the role of pre- and post-processing of galaxies and the relative role of the different environmental mechanisms at play, in this thesis we present a detailed study of galaxies in the massive and interacting cluster Abell 2670 (A2670) and its large-scale surroundings out to $5 \times R_{200}$. The interacting nature of the cluster offers the possibility to study post-processing while the large area studied additionally allows accounting for pre-processing. Our strategy is simple: we use optical imaging to identify morphological features in the cluster galaxies indicative of gravitational or hydrodynamical interactions and correlate them with their environment, which we characterize through a careful substructure analysis able to distinguish galaxy groups and other structures present in the field.

1.3 The interacting cluster Abell 2670

This thesis focuses on A2670, an interacting cluster at z = 0.0763, with a $\sigma_{200} = 919 \pm 46$, a total mass of $M_{200} = 8.5 \pm 1.2$ (10^{14}M$_\odot$) and a size of $R_{200} = 1.91 \pm 0.1$ Mpc (Sifón et al., 2015). Optical and X-ray analysis have concluded this cluster is undergoing a merger in the plane of the sky (Hobbs & Willmore, 1997; López-Gutiérrez et al., 2022), where the X-ray peak is coincident with the Brightest Cluster Galaxy (BCG), with coordinates R.A. (J2000) = $23^{\rm h}54^{\rm m}13^{\rm s}.7$, Dec. (J2000) = $-10^{\rm o}25'9.2''$.

All the previous works have been emphasized only in the central part of the cluster. In particular, a comet-like structure in X-rays was found around one of the brightest (cD) galaxies in the central region, with a cold front at the leading edge of the structure (Fujita et al., 2006) (Fig. 1.6). The mass of X-ray gas in the comet-like structure, which extends to about 100 kpc from the cD, suggests that the galaxy was in a small cluster, or group, and its ICM is being stripped away by ram pressure close to the cluster core. In Fig. 1.7, we show an optical map of the central region of the cluster with X-ray contours from Chandra overlayed on top, where the disturbances can be seen.

In terms of the galaxy populations in A2670, a large number of elliptical galaxies with faint features indicative of past interactions (post-mergers) were found by Sheen et al. (2012) near the cluster centre. The authors concluded that these probably merged in a previous group environment prior to entering the cluster. In addition, an intriguing and unique case of ram-pressure stripping in an elliptical galaxy with blue "tadpoles" associated with it was reported by Sheen et al. (2017). Furthermore, (López-Gutiérrez et al., 2022) presents HI observations of this cluster out to $\sim 2 \times R_{200}$ along NE-SW direction, finding three minor groups running along that direction, with strong pre-processing (HI-disturbed in this case) in the SW group.

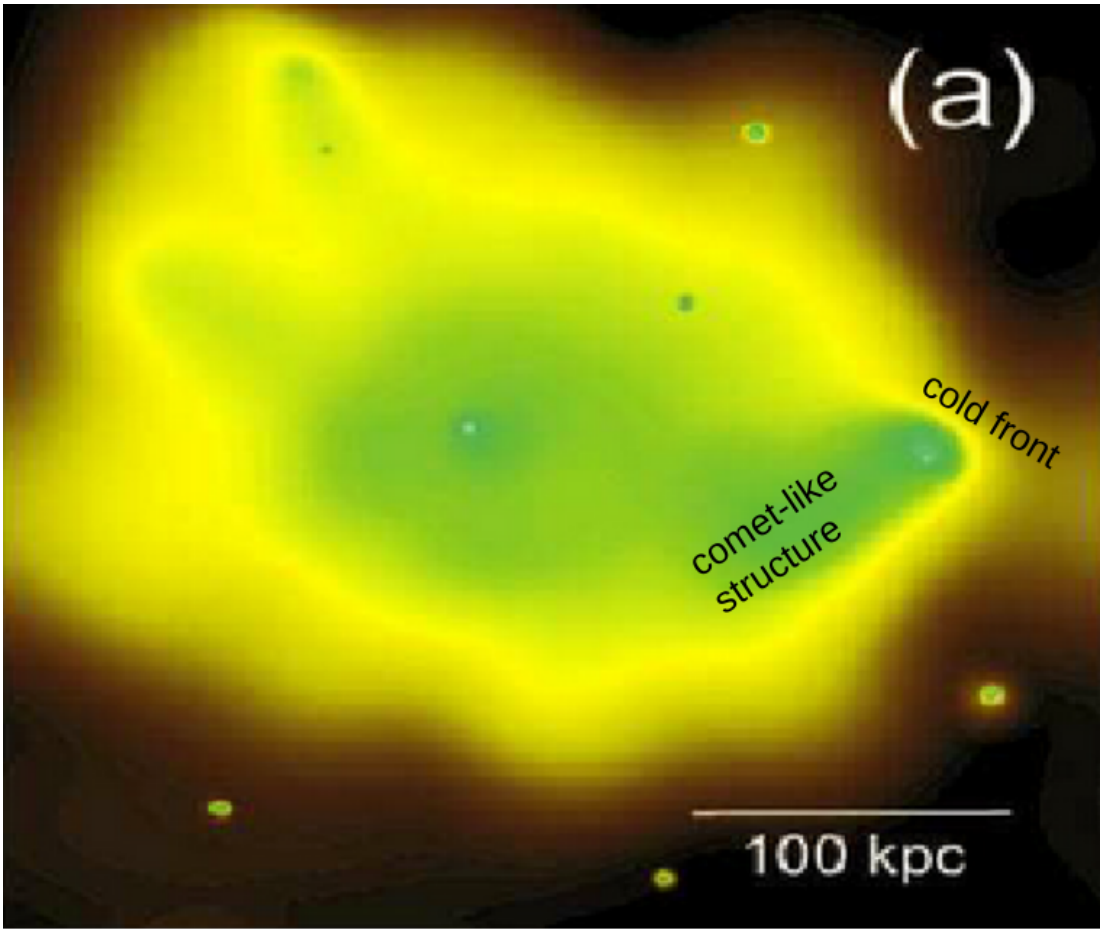

Figure 1.6: A comet-like structure in X-rays was found around one of the brightest galaxies with a cold front at the leading edge of the structure (Fujita et al., 2006)

1.4 This work

With the aim of better understanding the role of pre- and post-processing of galaxies and the relative role of the different environmental mechanisms at play, in order to understand which of these is the most dominant in the different pre- and post processing scenarios, in this thesis we present a detailed large-scale study surroundings out to $5 \times R_{200}$, considering that there not much studies of galaxies in large scale structures around clusters in comparison with studies of cluster core. The interacting nature of A2670 cluster offers the possibility to perform a pilot study of post-processing while the large area studied additionally allows accounting for pre-processing.

Our strategy is simple: we use optical imaging to identify morphological features in the cluster galaxies indicative of gravitational or hydrodynamical interactions and correlate them with their environment, which we characterize through a careful substructure analysis able to

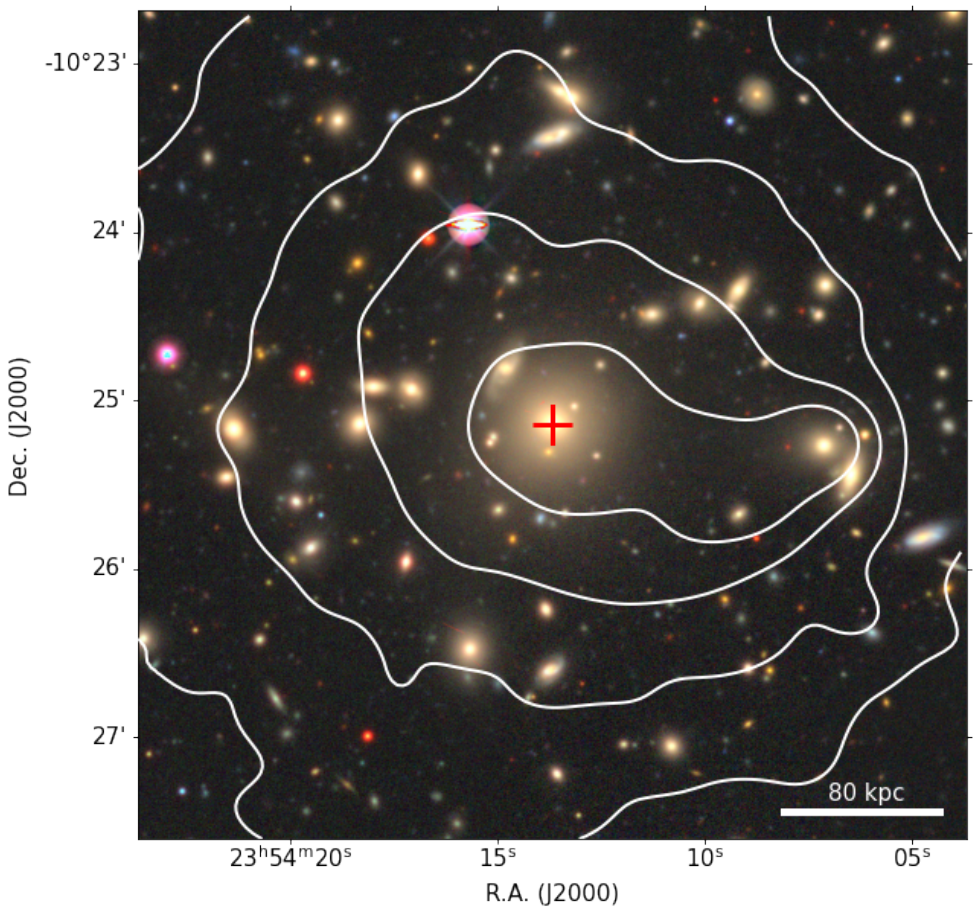

Figure 1.7: X-ray morphology contours from Chandra on top of a colour legacy survey image of the central region of the cluster. The BCG is marked with a red cross. The FOV is about $5' \times 5'$. A scale of 80 kpc can be visualized lower right.

distinguish galaxy groups and other structures present in the field.

The outline of this thesis is as follows: in chapter 2, we describe the photometric and spectroscopic optical datasets utilized to study the cluster and its galaxies, and we identify cluster members in the photometric and spectroscopic samples; in chapter 3 we perform different (2D and 3D) substructure analyses and compare the results between all the methods to robustly identify substructures in and around the cluster; in chapter 4 we perform a visual inspection of the cluster galaxies and identify interacting galaxies, split into main categories gravitational and hydrodynamical (RPS) interactions. We then study the incidence of interacting galaxies as a function of their local and global environment; in chapter 5 we show some works in progress, where we perform a measurement of the tail directions for jellyfish candidates that we found among the interacting candidates; in chapter 6 we discuss results and compare with the literature; in chapter 7 we summarize the main results and show conclusions; and finally, in chapter 8, we propose future works and extensions of this work.

This thesis assume a ΛCDM cosmology, with a Hubble constant $H_0 = 70$ km s^{-1} Mpc^{-1}, present matter density of $\Omega_m = 0.3$, and dark energy density $\Omega_\Lambda = 0.7$.

Chapter 2

Data

A novel and key aspect of our study is the wide-area explored around the cluster under study (A2670). To reach the far outskirts of the cluster ($5\times R_{200}$) we built a large photometric and spectroscopic catalogue in an area of $3.6^\circ \times 3.6^\circ$ centred on the BCG. The data is described in the following.

2.1 Optical Photometry

2.1.1 Legacy Survey

Our base sample for the wide-area explored consists of optical photometry from Legacy Survey (LS; Dey et al., 2019) public data release (DR9), obtained through the Astro Data Lab Query [1] interface. The main tractor photometry catalogue (combined north and south region), provides both model object type and the AB system apparent magnitudes converted from the Vega system[2], for 3 bands: g, r and z, with their respective de-reddened magnitudes corrected by galactic extinction E(B-V). Duplicates as well as objects with model type = PSF (stars) were excluded. Applying these filters, the base sample is conformed by 628,902 objects which cover up to $5\times R_{200}$, shown in grey in Figure 2.1 (left).

[1] https://datalab.noirlab.edu/query.php

[2] https://wise2.ipac.caltech.edu/docs/release/allsky/expsup/sec4_4h.html

For all the galaxies from this catalogue, we computed absolute magnitudes in r and g-band as follows

$$M_{band} = m_{band} - K_{corr}(m_{band}, z, m_g - m_r) - \mathrm{DM}(z) \tag{2.1}$$

where m_{band} is the apparent magnitude corrected by extinction (in r and g), DM is the distance modulus on function of redshift (z) and K_{corr} is the K-correction term for each galaxy as a function of apparent magnitude, z and color. This correction was estimated with a python code adopted from (Chilingarian et al., 2010; Chilingarian & Zolotukhin, 2012)[3]. For the z we assumed the mean cluster redshift for all galaxies.

2.1.2 Deep DECam imaging

We also used deep optical imaging in u, g, and r bands taken with the Dark Energy Camera (DECam) at the Blanco telescope in Cerro Tololo Inter-American Observatory from 19th August 2014 to 22nd August 2014 (Proposal ID: 2014B-0608, PI: Y. Jaffé), with 6300s, 4200s, and 9000s exposure time for the combined mosaic in u, g, and r-band, respectively in an area of $\sim 3\, deg^2$, covering $\sim 3\, R_{200}$ of the cluster.

After source extraction in the deep DECam images, we found 6,203 galaxies in common between the LS catalogue and the deep DECam catalogue. The galaxy sources from this catalogue were detected primarily in short-exposure and additionally from stacked Abell cluster A2670 mosaics in u, g, and r band.

The magnitudes of standard stars and galaxies were measured using Source Extractor (SExtractor) and compared those with Southern Standard Stars or SDSS catalogue, so that it could fit the zeropoints (ZPs) which are corrected for airmass term at each night. Using the ZPs, the galaxy magnitudes where measured from the SExtractor. The objects of this catalogue are plotted as green crosses in Figure 2.1 (left). This data is about a magnitude deeper than LS in g, and r and the surface brightness limits of the r band is over 28 mag/arcsec^2. The details of the data reduction, catalogue generation and surface brightness limit can be found in Kim et al. (in prep.).

2.2 Optical Spectroscopy

Public spectroscopic data from Sloan Digital Sky Survey (SDSS) DR9 (Ahn et al., 2012) were also collected for galaxies in the large area explored in this work, but these are only available

[3] http://kcor.sai.msu.ru/

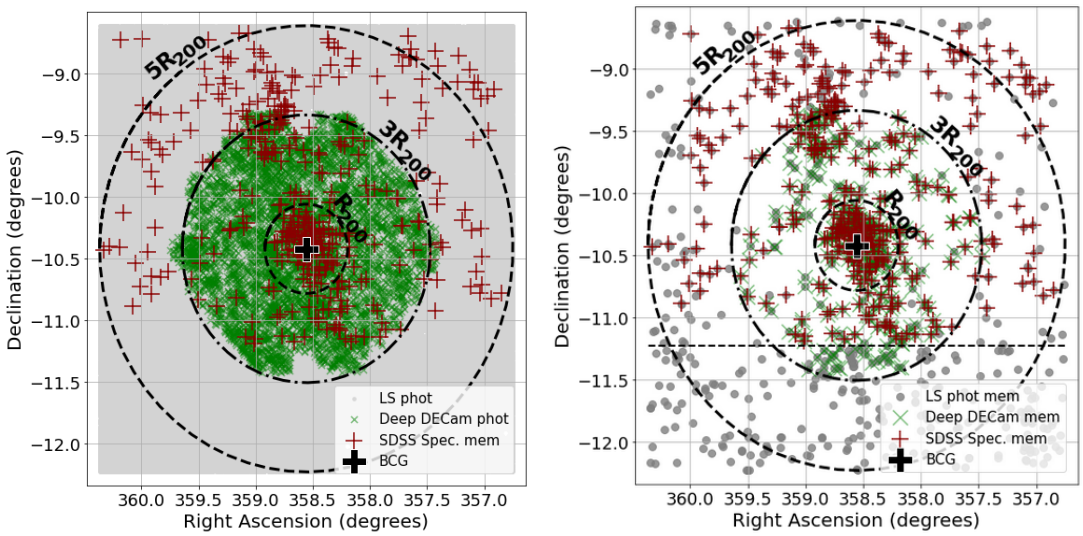

Figure 2.1: LEFT: Distribution of the 628,902 objects from LS DR9 (grey) and the 6,203 sources in common from our Deep DECam imaging (green) in the sky. The confirmed 405 members from available SDSS spectroscopic (red crosses) are overplotted. The dashed circles correspond to radii of 1, 3 and 5 $\times$ R_{200}, centred on the BCG (black cross). The black dashed horizontal line indicates the southernmost limit of SDSS. **RIGHT:** The final sample of galaxies used for the substructure analysis and the visual inspection. This sample consists of galaxies within our magnitude and colour cut (see Section 2.3.2), excluding galaxies with spectroscopy that are confirmed non-members (see Section 2.2). This yields a total of 843 photometric cluster members (grey), a total of 364 galaxies belonging to Deep DECam imaging (green) and 376 of which are confirmed spectroscopic cluster members (red)

for a declination $\gtrsim -11.^{\circ}2$ (dashed horizontal line in Figure 2.1). When matching the SDSS spectroscopic data with our parent sample, we found 1685 objects with redshift, down to the SDSS spectroscopic magnitude limit of $m_r \lesssim 17.5$, which roughly corresponds to $M_r \lesssim -20$. The spectroscopic redshift was used to define cluster membership as discussed in the following section.

2.3 Cluster Members

2.3.1 Spectroscopic cluster members

We use the available SDSS spectra to define cluster membership and to identify substructures. Figure 2.2 (top) shows the velocity distribution (zc) for all the galaxies with spectroscopy in our sample. Three overdensities are observed in the blackened region. If we zoom in, taking a velocity range covering this region (Fig 2.2, bottom), we can find a clear peak for the main cluster (red histogram). We can also identify two subgroups at low and high redshift, likely two

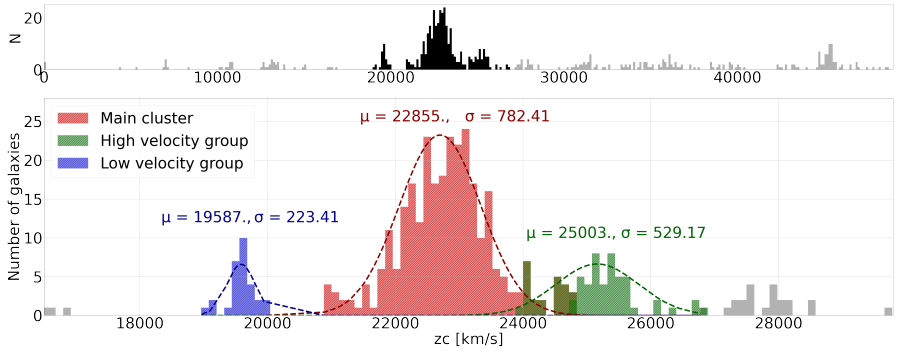

Figure 2.2: Velocity distribution of galaxies in A2670 using SDSS spectroscopy. Three main overdensities can be easily identified. Three Gaussian were fitted and memberships were assigned for galaxies within 3-sigma from the centre of each substructure. The main cluster corresponds to the red histogram centred at $zc = 22,855$ km s^{-1} (z = 0.076), and two additional groups in the foreground and background are identified in blue and green, respectively. In this work, we consider spectroscopic cluster members all galaxies in these three structures, which translates into a redshift cut of $0.063 < z < 0.09$ (their distribution in the sky is shown by the red crosses in the left panel of Figure 2.1).

accreting foreground/background substructures (blue and green histograms, respectively).

The departure from a single Gaussian distribution is already a sign that the cluster is not relaxed. To define cluster membership we fit three Gaussians, one to each of the overdensities, and consider galaxies within $\pm 3\sigma$ (the standard deviation) of the mean velocity to be part of that structure. The resulting mean velocities (μ) and dispersion σ for each structure are marked in Figure 2.2. Galaxies with velocities in the range $23,983.39 < zc < 24,806.67$ km s^{-1} (dark overlapping histogram in the figure) could belong to either/both the high-velocity group or the main cluster.

Given our scientific goal and the complex nature of this cluster, we define a generous final cluster membership that includes the main cluster as well as its foreground/background groups, covering a velocity range starting from the lower limit for the low-velocity group up to the higher limit for the high-velocity group ($18,916.6 - 27,036.66$ km s^{-1}). Using this definition, we obtain 405 spectroscopic cluster members and 1280 non-members from the 1685 galaxies with spectra in our sample. Spectroscopic cluster members galaxies are plotted in Figure 2.1 (left) as red plus markers (spectroscopic non-members are not plotted). We computed, for reference, the velocity dispersion of the core cluster members (red histogram) within R_{200}, obtaining $\sigma_{200} = 873.843$ km s^{-1}.

2.3.2 Photometric cluster members

We combine photometric and spectroscopic information to assemble an unbiased magnitude-limited sample of galaxies that are likely part of this assembling cluster. To define the photometric memberships, we opt to use the photometric information from the parent sample from LS as it has the largest extent, contrary to the photometric information from SDSS which is limited in declination.

We adopt a cut in $M_r < -20$ following Sheen et al. (2012). This cut allows for reasonable visual classification of the galaxies and at the same time, it coincides with the magnitude limit reached by SDSS spectroscopy ($m_r \lesssim 17.5$). We further consider colour cuts to maximize the probability of a given galaxy being a cluster member. We first identified the colour range of the confirmed spectroscopic members, which yielded $0.3 < M_g - M_r < 1$ (the dashed box in Fig. 2.3 upper). Then, using the confirmed spectroscopic members from the SDSS catalogue (subsection 2.3.1), we defined the *red sequence* and *blue cloud* galaxies within this box by fitting a double Gaussian to the colour distributions in 4 bins of M_r (delimited by the vertical lines in the middle panel of Figure 2.3. Our fitting procedure used the sklearn.mixture.GaussianMixture package from the python module Scikit-learn, a representation of a Gaussian mixture model probability distribution (Pedregosa et al., 2011; Buitinck et al., 2013). For the brightest bin, given the lack of blue galaxies, we only fitted a single Gaussian. In the bottom panel of Figure 2.3 we show as an example the double Gaussian fit performed to the fainter magnitude bin (M_r from -21 to -20 mag). The vertical orange line separates blue and red galaxies while the red one identifies the peak colour of the red galaxy population in that magnitude bin. Once this was done for all magnitude bins, we took the peak value of the redder Gaussian to fit a red sequence, using the mean of M_r of all of the spectroscopic member galaxies in each bin (see large filled circles in the middle panel of the figure). The resulting fit is shown as a dark black line in the middle panel of the figure

Finally, we considered photometric cluster members those galaxies above our magnitude limit. In order to avoid significant contamination from outliers in our selection (i.e. spectroscopic non-members, plotted as orange circles in the middle panel Fig. 2.3) without sacrificing possible cluster members, we further make a colour cut of -11 and $+2\sigma$ from the red sequence fit (dotted lines in the middle panel of Figure 2.3). Within this colour-magnitude region, the contamination from outliers is $< 35\%$.

The final sample of galaxies used for the substructure analysis and the visual inspection (Chapter 3 and 4, respectively) consists of the photometric plus spectroscopic members, and excludes galaxies that have a redshift placing them outside the cluster (see Section 2.3.1). This

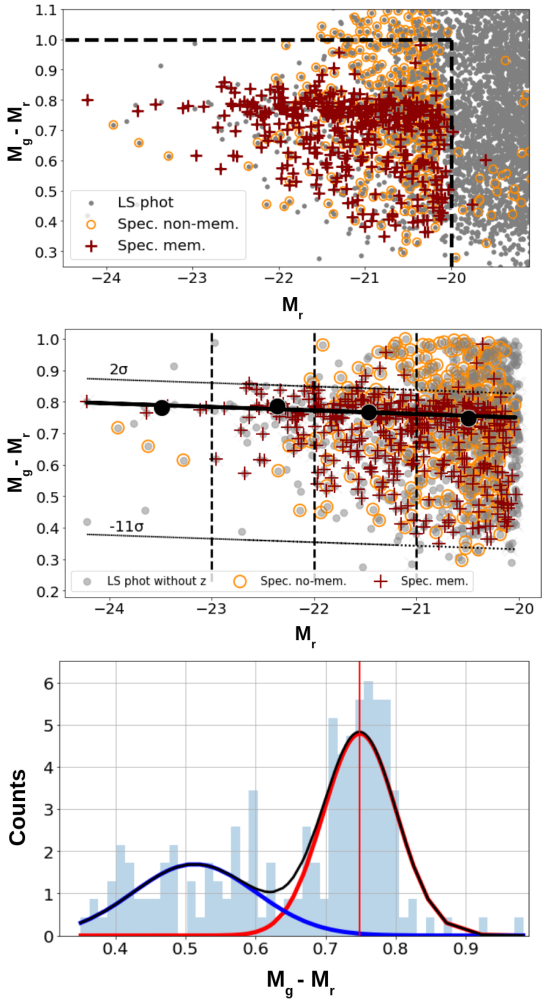

Figure 2.3: TOP: Color Magnitude Diagram for the complete LS photometric sample (grey) where we highlight the spectroscopic sample of both no-member (orange) and members (red) (Section 2.3.1). To maximize the probability of a given galaxy being a cluster member, we started with a reasonable cut in $M_r < -20$ (horizontal black dash line) following Sheen et al. (2012) and also because it coincides with the spectroscopic limit from SDSS ($m_r \lesssim 17.5$) and we considered the colour range of the confirmed spectroscopic members, which yielded $M_g - M_r < 1$ (vertical black dash line). **MIDDLE:** The four bins across the r band magnitude. For each bin and using only the confirmed spectroscopic members, a double Gaussian to the colour distribution was fitted. The peak value of the redder gaussian of each bin and the measured absolute magnitude corresponding to this peak are plotted as large filled circles and then the line was fitted which corresponds to the red sequence (dark black line). **BOTTOM:** An example of the double gaussian fit performed on the fainter magnitude bin (M_r from -21 to -20 mag). The vertical red line identifies the peak colour of the red galaxy population in that magnitude bin.

yields a total of 843 photometric cluster members, 376 of which are confirmed spectroscopic cluster members (Fig. 2.1, right panel). A total of 364 galaxies (green crosses in Fig. 2.1, right) from the photometric cluster members belong to Deep DECam imaging (Subsec. 2.1.2).

Galaxy stamps

For all the galaxies that belong to the final sample we made 60" × 60" image cutouts from Legacy Survey Sky Browser[4]. The cuts are r, g and z-band composite and were obtained as JPEGs files using the cutout service from LS for DR9. The size of the images were specified using a size of 256 pixels and a pixscale of 60/256 ("/pixels). For the galaxies with deep DECam data available we created fits cutouts in u, g and r-band with a size of 60" × 60" . The size of the fits cutouts images were specified using a size of 222.22 pixels and a pixscale of 60/222.22 ("/pixels). A set of stamps r'-band and $u'g'r'$-color images are available as well for some galaxies with deep DECam data (see Kim et al. in preparation for more details).

[4] https://www.legacysurvey.org/viewer

Chapter 3

Cluster substructure analysis

In Section 2.3.1, we found preliminary evidence through the galaxy velocity distribution that supports the merger scenario presented in the literature (see Section 1.3). In this section, we characterize the environment in and around A2670 out to its outskirts through the identification of substructures using two different methods.

3.1 Dressler-Shectman's test

The Dressler-Shectman (DS, Dressler & Shectman, 1988) test is a statistical test widely used in astronomy to establish whether a cluster is disturbed and to highlight galaxy substructures. In the case of a galaxy cluster, the DS analysis will highlight smaller galaxy groups clustered in the sky by measuring their deviations in velocity from the velocity distribution of the galaxies in the main cluster.

In short, the test consists of the following steps: We identify the N_{nn} nearest neighbours of each galaxy. Then, for each i-group of $N_{nn}+1$ galaxies, we compare the *local* mean velocity $\overline{v}^i_{local}$ and dispersion σ^i_{local} with the *global* mean velocity $\overline{v}_{cl}$ and dispersion σ_{cl} of the cluster. This is done by computing the deviation δ_i parameter, defined as:

$$\delta_i^2 = \left(\frac{N_{nn}+1}{\sigma_{cl}^2}\right)\left[(\overline{v}^i_{local}-\overline{v}_{cl})^2+(\sigma^i_{local}-\sigma_{cl})^2\right] \tag{3.1}$$

The larger the value of δ_i, the larger deviation of the local parameters with respect to the global ones.

We applied the DS test to all confirmed spectroscopic members from the photometric cluster members sample. In order to highlight the infalling structures, the cluster parameters $\overline{v}_{cl}$ and σ_{cl} were determined considering only members from the main cluster (red histogram, see Section 2.3.1) and that are within R_{200}, using $N_{nn} = 10$ following similar studies (e.g. Jaffé et al., 2013).

To confirm and quantify the disturbed nature of the cluster, we performed the two standard statistical DS tests:

1. **Critical value:** A cumulative deviation Δ is computed as the sum of δ_i:

$$\Delta = \sum_i \delta_i \tag{3.2}$$

   Values of $\Delta/N_{mem} > 1$ indicate a strong evidence of substructures, where N_{mem} is the number of cluster members.

2. **P-value**: To further test the statistical robustness of the Δ-value test, it is possible to shuffle randomly the observed radial velocities of each galaxy cluster member and reassigning them to a new galaxy of the sample (i.e. Monte Carlo shuffling), in order to compute 'shuffled' Δ-values. Comparing these $\Delta_{shuffle}$ values with our Δ_{obs} computed from Eq. (3.2), we can obtain a P-value defined as

$$P = \sum(\Delta_{shuffle} > \Delta_{obs}/N_{shuffle}) \tag{3.3}$$

   Where $N_{shuffle}$ is the number of Monte Carlo shuffles performed, typically around 5000. Values of P < 0.01 provide a robust constraint on the presence of substructures in the clusters.

   We obtain $\Delta/N_{mem} = 2.83$ and P < 0.001 after applying the DS test in A2670. We confidently conclude that the cluster hosts significant substructures. One of the disadvantages of the DS test is not being able to identify which galaxies are members of the substructures. To this aim, we applied a second test described in the following.

3.2 Mclust test

Mclust (Scrucca et al., 2016) is an R package for model-based clustering and density estimation using finite Gaussian Mixture Models (GMM). The code applies the Expectation-Maximization

(EM) algorithm to estimate the parameters of GMM for clustering. For a multidimensional analysis, *mclust* provides 14 models with varying geometry depending on its distribution, volume, shape and orientation (See Appendix A.1). For each model, the code can find one, two or more numbers of components. *Mclust*, by default, identifies the model that best fits the data using the Bayesian Information Criterion (BIC, Kass & Raftery, 1995). The code also allows the user to visualise the clustering results and assess the model fit. *Mclust* has been widely used in astronomy for substructure analyses (e.g. Einasto et al., 2012b,a; Monteiro-Oliveira et al., 2020, 2022; Lourenço et al., 2020)

3.2.1 Mclust 2D

We first apply *mclust* in 2D to the spatial distribution of all photometric cluster members (defined in Sec 2.3.2). When running *mclust* in 2D, the model that converged to the highest BIC found a total of 8 components of varying volume and shape (VVI in Appendix A.2).

In Figure 3.1, the eight components are highlighted with eight different symbols and labelled with numbers increasing inversely with the galaxy density: Component 1 (Comp. 1) corresponds to the densest substructure and Component 8 (Comp. 8) the lower density one. For reference, the five brightest galaxies are also plotted as larger filled circles, with the sizes reflecting their relative magnitudes. These galaxies coincide with some of the substructures found and have similar magnitudes (difference of 0.56-0.86 mags) which according to Raouf et al. (2019) is indicative of cluster interaction. In Figure 3.2 (top panel), we further plot the fraction of galaxies in each component relative to all the photometric cluster members. The total number of photometric cluster members per components are listed in table A.1 (top).

The densest structure (Comp. 1, filled circles in Fig. 3.1) is a group of 146 galaxies ($> 17\%$ of all the photometric members) located at the centre of A2670. This structure coincides spatially with the X-ray emission (see Figure 1.7) and the BCG (solid open circle at the centre of Fig 3.1), clearly indicating this component corresponds to the main cluster (A2670). The second densest component is located southwestward of the main cluster at $> 5R_{200}$ (Comp. 2, x symbols in Fig. 3.1), where we see a compact clump with 46 galaxies distributed around the 5th brightest galaxy in the field. It is unclear if this group extends further as it is at the edge of the inspected field. A third high-density component with 144 galaxies was detected northeastward of the main cluster (Comp. 3, stars in Fig. 3.1). This group has the 3rd and 4th brightest galaxies in the field and is comparable in number of galaxies to the main cluster, but it is less dense, and extends from $\sim$2 to $\sim 5R_{200}$. Based on their proximity and also their velocities (see bottom panel of Figure 3.1) it is likely that Comp. 3 and Comp. 1 are in the process of merging

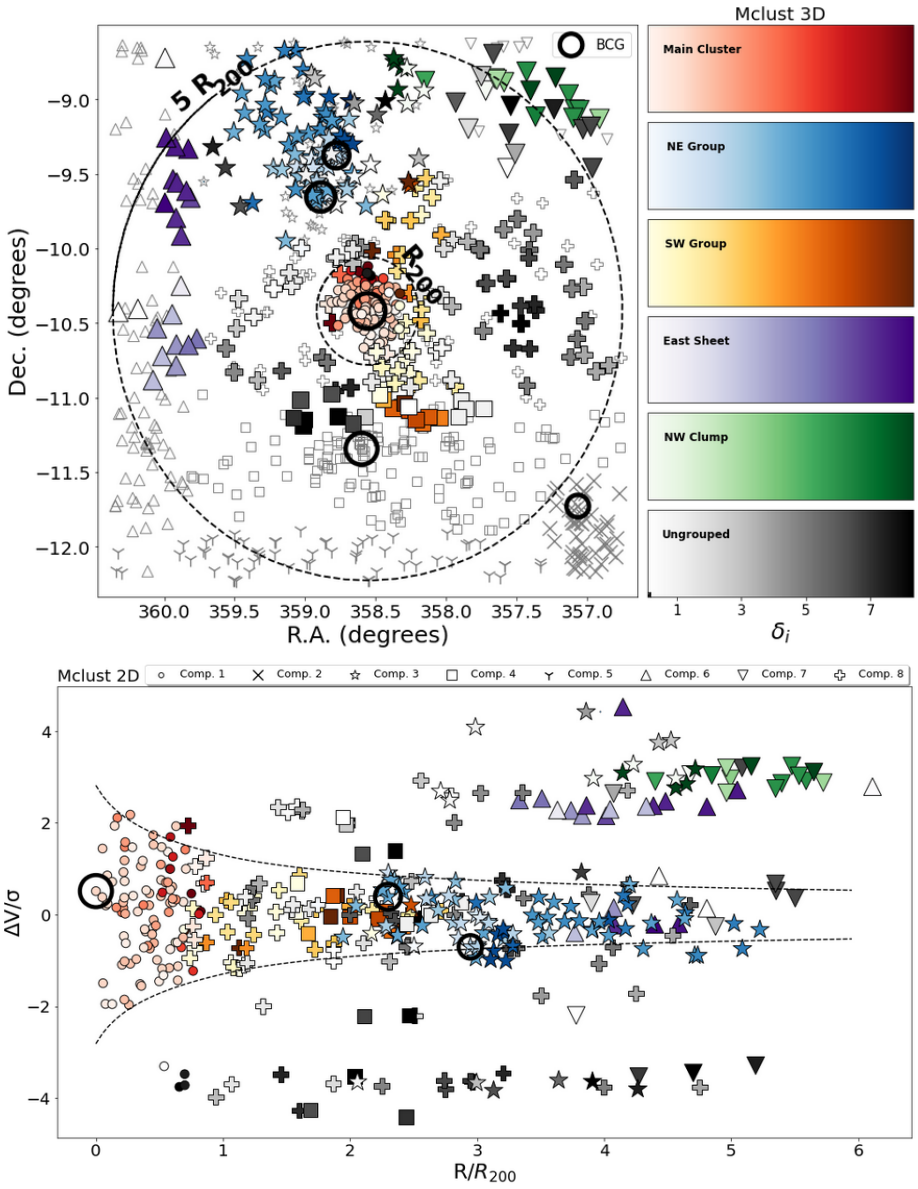

Figure 3.1: Distribution of the photometric cluster members in the sky (TOP) and the spectroscopic cluster members in position vs. velocity phase-space (BOTTOM). The substructures identified by *mclust* 2D and 3D are highlighted with different symbols and colours respectively, while the darkness of the colour increases with increasing δ_i (from the DS analysis), as labelled. Note that because not all photometric members have a spectroscopic redshift, some galaxies that belong to structures found by *mclust* 2D are not in the 3D sample (i.e. the smaller grey open symbols, which are absent in the bottom plot). The inner and outer circles in the top panel correspond to 1 and $5R_{200}$, respectively. The 5 brightest galaxies are also plotted as solid black open circles, with the sizes reflecting their relative magnitudes (in the phase space only those with redshifts are plotted). The dashed curves in the bottom panel correspond to the escape velocity in a NFW halo (Navarro et al., 1996) with the concentration parameter equal six, similar to Jaffé et al. (2015).

with each other. In fact, the BCG (Comp. 1) has a similar magnitude to the brightest galaxy of Comp. 3 (with a magnitude gap of ~ 0.6), which according to Raouf et al. (2019) is indicative of cluster interaction. The fourth densest structure (Comp 4, squares in Figure 3.1) is the most numerous one, containing over 19% of the galaxies. This loose structure is located southward of the main cluster, has the second brightest galaxy in the field, and extends from ~ 1.5 to $\sim 5R_{200}$. Further south another very loose and extended (along R.A.) component is detected at the edge of the field (Comp. 5, propellers in Fig. 3.1) with 61 galaxies (7% of the sample). Towards the east, there is also an extended (along DEC.) structure of 96 galaxies (Comp. 6, triangles in Fig. 3.1) and at the north-west corner a low-density but well-separated group of 36 galaxies (Comp. 7, inverted triangles in Fig. 3.1). Both of these structures have high relative velocities ($\sim 3\sigma$) with respect to the main cluster, as shown in the bottom panel of Figure 3.1. Finally, the analysis found 152 galaxies that do not seem to be grouped (Comp. 8, crosses in Fig. 3.1). This component is indeed the least reliable "group" because the second-best model of our analysis (i.e. that with the second-highest BIC, which was only marginally smaller) excluded this structure.

3.2.2 Mclust 3D

We add spectroscopic information on line of sight velocity to perform a three-dimensional (3D) analysis. Our 3D analysis was performed using only the confirmed spectroscopic members from the photometric cluster members sample, which limits the sample in numbers and also in the area covered (See Figure 2.1 and section 2.3.1). *Mclust* 3D finds that the model with the highest BIC was the same for *mclust* 2D, but this time with a total of 6 components (VVI in Appendix A.2). In the bottom panel of Figure 3.2 we plot the fraction of galaxies for each component relative to all the spectroscopic cluster members. The total number of photometric cluster members per components are listed in table A.1 (bottom).

In Figure 3.1, the six components are highlighted with six different colours and labelled according to their position on the plane of the sky: The Main Cluster (red in Fig. 3.1) is the densest and dominant structure at the centre, with a total of 102 galaxies (> 25% of the spectroscopic cluster members) clearly corresponds to Comp. 1 found by *mclust* 2D. A second less populated group of 76 galaxies at the same mean velocity of the cluster and located $> 2R_{200}$ northeastward was labelled NE Group (blue in Fig. 3.1), and largely corresponds to Comp. 3. A third group with 48 galaxies at the same velocity of the main cluster, and located mostly towards southwest, but also partially extending to the northwest was labelled as SW Group (orange in Fig. 3.1). This group includes galaxies from Comp. 4 and Comp. 8 from the 2D analysis.

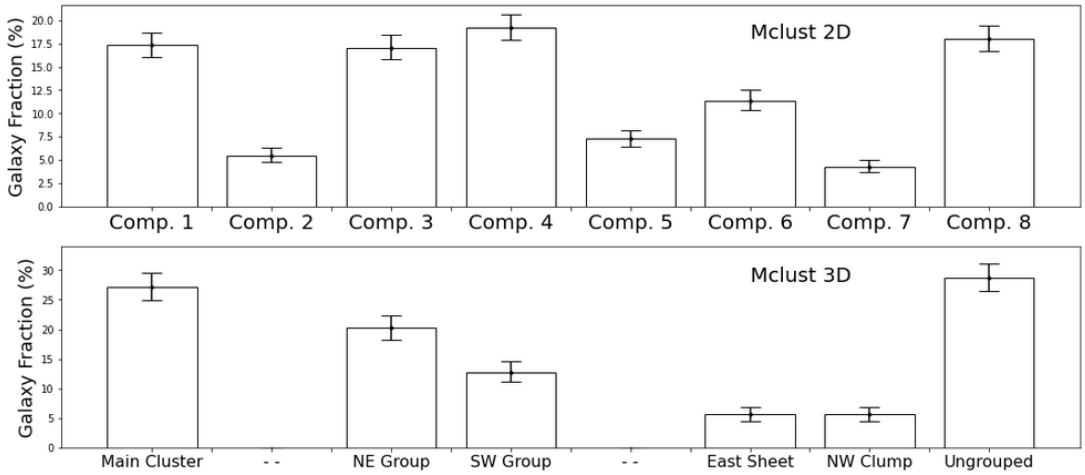

Figure 3.2: Galaxy fraction for all the components, respect to the photometric cluster members for *mclust* 2D (top) and respect to the spectroscopic cluster members for *mclust* 3D (bottom). The error bars correspond to a binomial proportion confidence interval, using a Wilson interval.

A pair of poorly populated but clearly separated substructures at high relative velocities were found towards the east and towards the northwest, and were called East Sheet (purple in Fig. 3.1) and NW Clump (green in Fig. 3.1) respectively. These largely correspond to Comp. 6 and 7. Finally, we have a sixth "Ungrouped" component (grey in Fig. 3.1), that spans a broad area and velocity range and hence it's not well defined. More than 25% of the spectroscopic cluster members belong to this component, with a total of 108 galaxies.

The comparison between the best and second best models in 3D yields a BIC difference less than 5 (|BIC diff|: 4.703, see A.2), indicating that the number of components is not fully reliable (Kass & Wasserman, 1995). Furthermore, the composition of the SW Group shows a strong uncertainty in comparison with the other components. Actually, the second-best model detects a seventh component composed of some galaxies that belong to SW Group, mainly those that are extended northward. In addition, only some of the southern galaxies in this group seem to be part of a similar group found by *mclust* 2D in the same direction (Comp. 4).

3.3 Comparison of the different substructure analysis

In general, there is a good agreement between the structures found by the 3D and 2D analysis as they both robustly find the main cluster (Comp. 1), a large group towards the NE (Comp. 3) and

two lower-density high-velocity substructures: East Sheet (Comp. 6) and NW Clump (Comp. 7). However, the southern part is not subject to comparison between the 2D and 3D analysis, since this region is not covered by the spectra and it is difficult to predict if the SW Group could extend beyond the limited declination (see Section 2.2) forming a similar southward component like at *mclust* 2D (Comp. 4).

One caveat of *mclust* is that a mixture of Gaussians does not necessarily describe the data distribution. Not all the galaxies in the sample belong to the group that the GMM assigned them to. For example, the foreground group in the Figure 2.2 (blue histogram), 2D and 3D analysis don't give a clear index about substructures or components located to low velocities. In fact, in the phase-space (Fig. 3.1, bottom) we see a clear sheet of galaxies located in $\Delta V/\sigma <$ -3. This is composed by galaxies that are members of different components of 2D and all these galaxies were detected as ungrouped galaxies for 3D. Only some galaxies with high δ_i values that could be located in the west on the plane of the sky, could be part of this structure.

Nevertheless, using the *mclust* with the DS test allows us to validate the substructures of the different methods. Indeed there are higher values of δ_i in the substructures found by *mclust*, as seen by the darker colours in Figure 3.1 in all of these structures except for the main cluster which was taken as reference in the DS analysis.

Chapter 4

Visual inspection of the cluster galaxies

The large amount of substructures found in Chapter 3 confirms that A2670 is indeed a complex merging/interacting system. In order to understand how the galaxies in this system are affected by the local and global environment, seven classifiers visually inspected all the photometric cluster members (see Section 2.3.2) to search for signs of ongoing or past interactions (e.g. mergers and ram-pressure stripping), independently of their morphology. To perform the visual inspection we use the stamps described in section 2.3.2.

In the following, we explain the tools and methods used to classify the galaxies (Sec. 4.1) and present the population of interacting galaxies found in the cluster and substructures (Sec 4.2).

4.1 Identification of interacting galaxies

We developed a custom-made tool in python to inspect and classify each galaxy [1]. The code displays several images of a given galaxy: a colour RGB composite image from LS, alongside the deep DECam g and r-band images (when available) and ugr-color composite stamps (Kim et al. in prep.). Each classifier visually inspects the stamps to assign a classification. The priority of visual inspection performed here over automated techniques for morphology detection is it

[1] https://github.com/FrancoPiraino/Interacting_Galaxy_Classification.git

can serve as a reference for ongoing or future larger studies aiming at identifying interacting galaxies in large optical datasets visually, (e.g. for ongoing citizen science projects "*Fishing for Jellyfish Galaxies*"[2]).

Seven authors (FP,YJ,VS,JC,AL,KK,DP) independently classified all or a subset of the total galaxy sample, assigning for each of them, one of the following categories:

- **Merger (M):** Ongoing merger between two or more galaxies resulting in a very disturbed system, multiple cores, or features such as tidal tails or stellar bridges between galaxies.
- **Post-merger (PM)**: Typically bright elliptical galaxies with faint features around the galaxy such as shells that indicate a past gravitational interaction/merger (see Sheen et al., 2012, 2017).
- **Ram-pressure stripping or "jellyfish" candidate (JF):** Galaxies with features indicative of gas stripping such as one-sided asymmetries, tails, star formation in one side and/or unwinding spiral arms, (see Poggianti et al., 2016; Bellhouse et al., 2021; Vulcani et al., 2022).
- **Gravitational or hydrodynamical (JM):** Cases of interacting galaxies where it is not clear whether the disturbance is gravitational (i.e. M or PM), hydrodynamical (JF), or both at the same time.
- **Star (S):** Very bright point-like sources that could be stars.
- **Broken (B):** The classification was not possible due to artefacts such as saturation from nearby stars.
- **Nothing (N):** Normal galaxy of any type (spiral, lenticular, elliptical or irregular) with no clear sign of gravitational or hydrodynamical interactions.

Once all galaxies were classified by at least n = 3 inspectors, we follow the flowchart in Figure 4.1 to allocate a final category for each galaxy and associated uncertainty for the type of interaction (Gravitational, RPS, or none).

We start by counting the total number of votes per each galaxy (n). We then count how many of the n votes went into each of the seven categories (N_{category}). Some of the categories are related (e.g. M and PM), so before assigning a final category for the galaxy, we group the votes of related categories into three broader classes. This allows us to compute an uncertainty

[2] https://www.zooniverse.org/projects/cbellhouse/fishing-for-jellyfish-galaxies

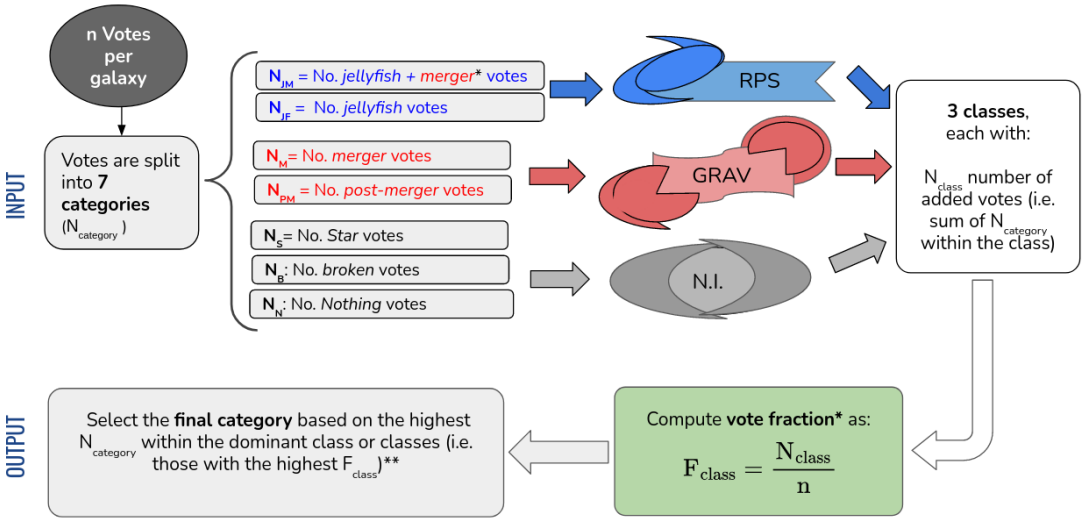

Figure 4.1: Flowchart with the visual classification scheme. The *input* consists of the classifications of the different inspectors in different categories, while the *output* corresponds to a unique final category (JF, JM, M, PM, S, B or N), accompanied by the likelihood of being in each of the 3 main classes (i.e. the vote fractions $F_{\rm RPS}$, $F_{\rm GRAV}$ and $F_{\rm N.I.}$) as explained in the text.

that reflects the vote fraction for the general class, rather than the specific category. The three classes are:

- **Ram-pressure stripping class (RPS):** which includes the categories JF and JM. To estimate the likelihood that the galaxy is experiencing RPS, the fraction of the JF and JM votes over the total number of votes is computed as:

$$F_{\rm RPS} = \frac{N_{\rm JF} + 0.5 \times N_{\rm JM}}{n} \tag{4.1}$$

  where $N_{\rm JF}$ is the number of JF votes, and $N_{\rm JM}$ is the number of JM votes.

- **Gravitational interactions class (GRAV): Includes M and PM** Likewise, we compute the likelihood that a galaxy is undergoing a gravitational interaction as the fraction of JM, M, and PM votes, following:

$$F_{\rm GRAV} = \frac{N_{\rm M} + N_{\rm PM} + 0.5 \times N_{\rm JM}}{n} \tag{4.2}$$

  where $N_{\rm M}$ is the number of M votes, and $N_{\rm PM}$ is the number of PM votes.

- **Non-Interacting class (N.I.):** We finally compute the combined probability that the galaxy is not interacting by considering the N, S, and B votes:

$$F_{\mathrm{N.I.}} = \frac{N_{\mathrm{S}} + N_{\mathrm{B}} + N_{\mathrm{N}}}{n} \tag{4.3}$$

  where N_{S} is the number of S votes, N_{B} is the number of B votes, and N_{N} is the number of N votes.

Note that for JM category, the votes were split between the RPS and GRAV class (see Eq. 4.1 and 4.2), since for those cases both types of interactions could be at play, or it is not clear which of them dominate. In these cases, half of the weight was assigned to each vote fraction in order to preserve the total number of votes per galaxy.

The vote fractions in each class (F_{class}) are indicative of the dominant process affecting (or not) the galaxy and are used as a measure of the uncertainty in the final classification.

To define the final category of a galaxy, we select the dominant class with the highest vote fraction. If there is one dominant F_{class}, the assigned final category will be that with the highest N_{category} within that class. For example, if the vote fraction of the RPS class (F_{RPS}) dominates, the category with more votes among JF and JM will be the final category for this galaxy (see examples in Fig. 4.2, top middle and right panels). For 5% of photometric cluster members, there was more than one dominant class. In these cases, the final category assigned is that with the highest N_{category} within the dominant classes.

When assigning the final category, $N_{\mathrm{categories}}$ are occasionally tied within the dominant class(es). In general, we gave priority to the categories listed higher in the flowchart of Figure 4.1. For instance, in case of a tie among N_{JF} and N_{JM}, we choose the latter as the final category to be conservative (see example in Fig. 4.2, top right). If F_{GRAV} dominates, the category with more votes among JM, M, and PM is assigned (Fig. 4.2, bottom left and centre). In the case of a tie between N_{JM}, N_{M} and/or J_{PM}, we assigned the final category JM to ensure we did not throw away possible RPS candidates. If only M and PM share the same amount of maximum votes, we opt for M as the final category. If RPS and GRAV have the same (dominant) vote fraction, the category with more votes among JF, JM, M, and PM will be adopted as the final category (Fig. 4.2, top left). If the vote fraction of N.I. class dominates, the category with more votes among S, B, and N is considered the final one (Fig. 4.2, bottom right). In the case of a tie, S was the assigned category. In case B and N have the same amount of maximum votes, B was prioritized. In summary, the output consists of a final category (JF, JM, M, PM, S, B, or N) for each galaxy, accompanied by the likelihood of that galaxy belonging to each of the three classes (i.e. the vote fractions F_{RPS}, F_{GRAV}, and $F_{\mathrm{N.I.}}$) that indicate the likelihood of a galaxy

being disturbed by RPS, gravitational interactions or not being disturbed at all. To visualize the classification scheme, we give some examples of different classifications in Figure 4.2. In the top-left example (Galaxy 43), $n = 5$ inspectors classified the galaxy, with two votes for JF, one for JM, one for M, and one for PM. The computation of the RPS vote fraction, $F_{\rm RPS}$, considers only the votes for JF and JM (see eq. 4.1), and yields 0.5. Likewise, $F_{\rm GRAV}$ (Eq. 4.2) considers only the votes for JM, M, and PM, and yields 0.5. Naturally, $F_{\rm N.I.} = 0$ (N.I.; Eq. 4.3) as there were no votes for S, B, or N. Since $F_{\rm RPS} = F_{\rm GRAV}$ for this galaxy, the final classification is that with the most votes within these two classes, which in this case is JF. Therefore the galaxy with ID:43 is a JF candidate with 50% likelihood to be interacting hydrodynamically, 50% likelihood to be interacting gravitationally, and 0.0% likelihood of not undergoing an interaction.

All the interacting galaxies found in this work are listed in the table shown in Appendix B, where we see their final category and vote fraction for each class ($F_{\rm RPS}$, $F_{\rm GRAV}$ and $F_{\rm N.I.}$). The corresponding LS images for all of them are shown in this section as well.

4.2 The population of interacting galaxies

In Figure 4.3 (left), the distribution of vote fraction for the entire cluster galaxy sample is plotted for each class. It is clear that the majority of the sample is not interacting, but an impressive number of galaxies are. Specifically, 236 galaxies are considered to be undergoing gravitational or hydrodynamical interactions based on their final categories (= JF, JM, M or PM). This implies that more than 27% of all the photometric cluster members have visible signs of disturbances caused by environmental effects and most (but not all) have high classification confidence. Being more conservative and only taking into account galaxies with high vote fractions within the interacting classes (i.e. $F_{\rm RPS}$ or $F_{\rm GRAV} > 0.5$), we find a lower but still impressive number of interacting galaxies (172), corresponding to $\sim 20\%$ of the photometric cluster members.

The dominant class with more than half of the interacting galaxy sample is RPS (over 60% including JF and JM), as can be seen in the right-hand panel of Figure 4.3. However, not all of them have a high vote fraction. This can be seen in Figure 4.4, where it is shown that only over 40% of interacting galaxies classified as JF have $F_{\rm RPS} > 0.5$ (bottom left of the figure). Also, if we consider the JM cases, the situation naturally worsens, with only $\sim 1\%$ of them having $F_{\rm RPS} > 0.5$ (Fig. 4.4, bottom right). In other hand, more than 37% of the interacting galaxies sample is GRAV (including M and PM), as can be seen in the right-hand panel of Figure 4.3. However, only over 24% of interacting galaxies classified as M have $F_{\rm GRAV} > 0.5$ (Fig. 4.4, top left) and more than 7% PM galaxies have $F_{\rm GRAV} > 0.5$ (Fig. 4.4, top right). Finally, is more common to find that all the classifiers are agree when a galaxy doesn't have signs of interaction,

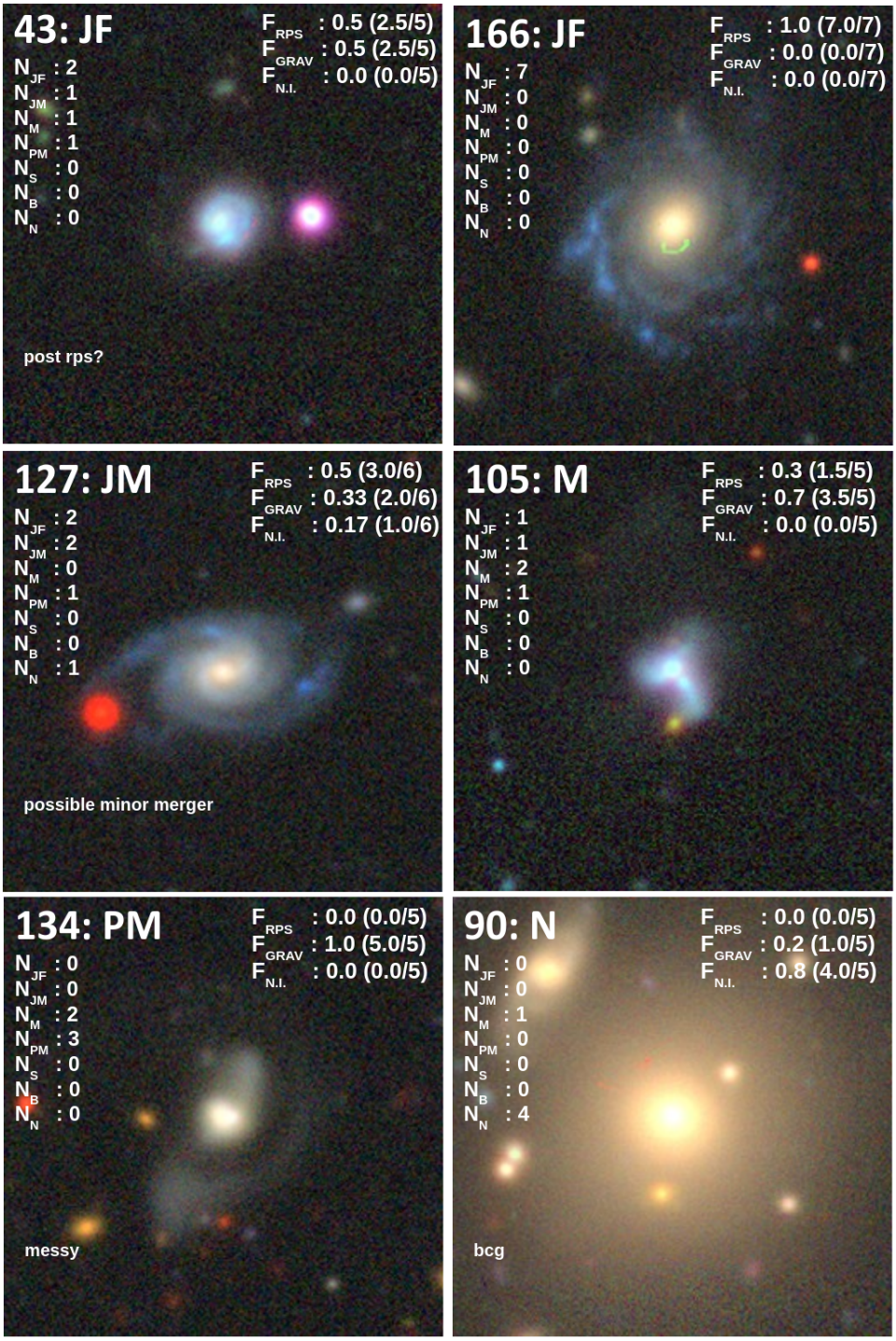

Figure 4.2: Legacy Survey images for a few examples of the different interacting classifications. In the upper left of each image we can see the ID of the galaxy and the final category assigned to each galaxy, as well as the number of votes for each category (N_{category}) below that. In the upper right, the vote fraction for each class is overplotted (F_{class}). In the bottom left, for some galaxies, we see comments from the inspectors. The example in the bottom right we see an example for a non-interacting classification. The corresponding LS images for all the interacting galaxies found in this work are shown in Appendix B

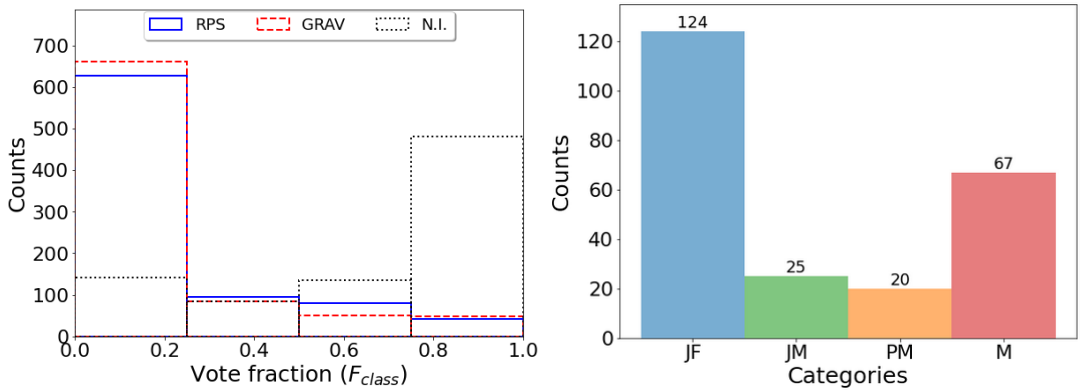

Figure 4.3: LEFT: Distribution of vote fractions for the entire cluster sample evaluated, split into each class ($F_{\rm class}$; see legend and eq. 4.1,4.2,4.3). **RIGHT:** Distribution of the final categories assigned to the interacting galaxies identified in our sample. In blue, we have the number of galaxies that were classified as JF. In green, we have the number of galaxies that were classified as JM. In orange, we have the number of galaxies that were classified as PM. In red, we have the number of galaxies that were classified as M. The number is displayed above each bar.

which should correspond to more than 70% of the cluster galaxy sample that have a $F_{\rm N.I.} > 0.5$ (Fig. 4.3), black dot histogram from left panel).

Keeping these uncertainties in mind, we can conclude that $\sim 20-27\%$ of the cluster galaxies belonging to the photometric cluster members are interacting, of those $\sim 42-63\%$ are being affected by ram-pressure stripping (RPS) and $\sim 31-37\%$ by gravitational interactions (GRAV).

The spatial and phase-space distribution of all interacting galaxies identified is shown in Figure 4.5. The final categories (JF, JM, PM, and M) are marked with different symbols and colours. The assigned vote fractions are indicated by the colour gradient, where the more confident classifications are shown with darker colors, using $F_{\rm RPS}$ for JF and JM galaxies, and $F_{\rm GRAV}$ for PM and M galaxies. We use a grey colour bar to represent the gradient of the four colours. At first glance, the interacting galaxies seem to follow the dominant substructures identified in Figure 3.1 very well, with many of them clustering in the centre, where the main cluster is, and the distributed mostly in the NE-SW direction, where the largest structures (and brightest galaxies) are. A remarkable finding is the presence of clear cases of ram-pressure stripped galaxies (JF with a high vote fraction, darker blue stars in the figure) very far from the cluster core, at $> 4 \times R_{200}$ (e.g. in the East Sheet of galaxies). Examples of JF galaxies in the outskirts include galaxies with ID 135, 222 and 712; shown in Figure B.1

To investigate the correlation between galaxy morphology and cluster substructures, in Figure 4.6 we plot the fraction of interacting galaxies (black line) as a function of cluster

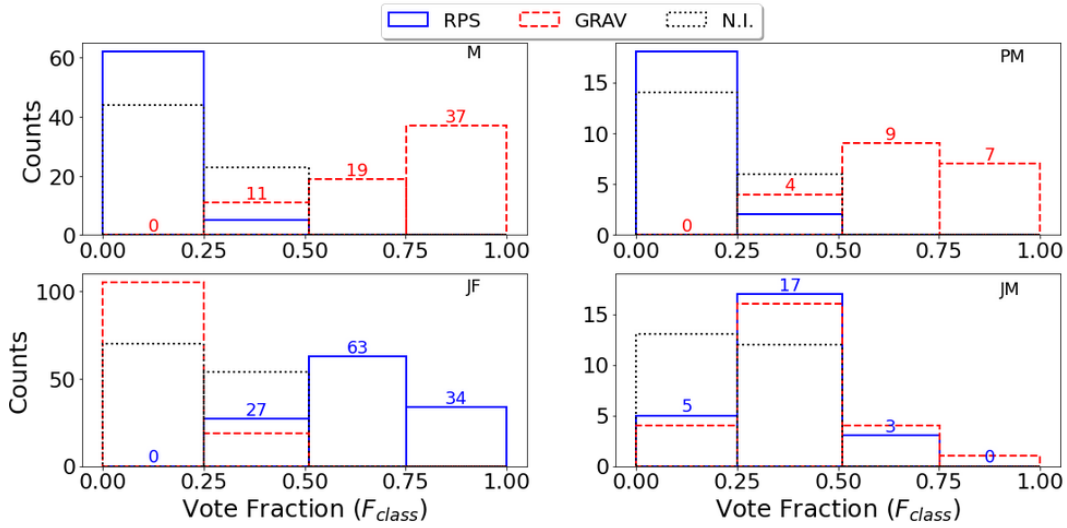

Figure 4.4: Distribution of vote fractions for each class ($F_{\rm class}$) and for the four different final categories within the interacting galaxy sample. In the top left, we see the distribution of the three vote fractions for all these galaxies that were classified as M, where more than 23% of them have $F_{\rm GRAV} > 0.5$. In the top right, we see the distribution of the three vote fractions for all these galaxies that were classified as PM, where more than 6% of them have $F_{\rm GRAV} > 0.5$. In the bottom left, we see the distribution of the three vote fractions for all these galaxies that were classified as JF, where more than 40% of them have $F_{\rm RPS} > 0.5$. In the bottom right, we see the distribution of the three vote fractions for all these galaxies that were classified as JM, where only more than 1% of them have $F_{\rm RPS} > 0.5$. We conclude that $\sim 31-37$% of interacting galaxies are being gravitational (GRAV) and $\sim 42-63$% are being ram-pressure stripping (RPS).

substructures, ordered by decreasing density. The top panel corresponds to structures identified by *mclust* 2D and the bottom panel to *mclust* 3D. In the 3D case, where substructures are more robustly identified, we find that the main cluster has the highest number of interacting galaxies, and the substructures that follow in density have increasingly lower fractions of interacting galaxies. The case of 2D is not too dissimilar if we exclude substructures that are very loose, poorly defined, or at the edge of the field where the spectroscopic information is not available (namely Comp. 2, 4, and 5). This alone is already a strong indication of pre-processing. Interestingly, in both cases the fraction of interacting galaxies outside of substructures (in Comp. 8 or in the "Ungrouped" component) is comparable or even higher than that in the main cluster, suggesting that interaction between the galaxies and their environment can happen between and around cluster substructures. One interpretation of the high fraction of interacting galaxies around substructures is that the accretion of the groups into the cluster is what is causing the disturbances (i.e. post-processing).

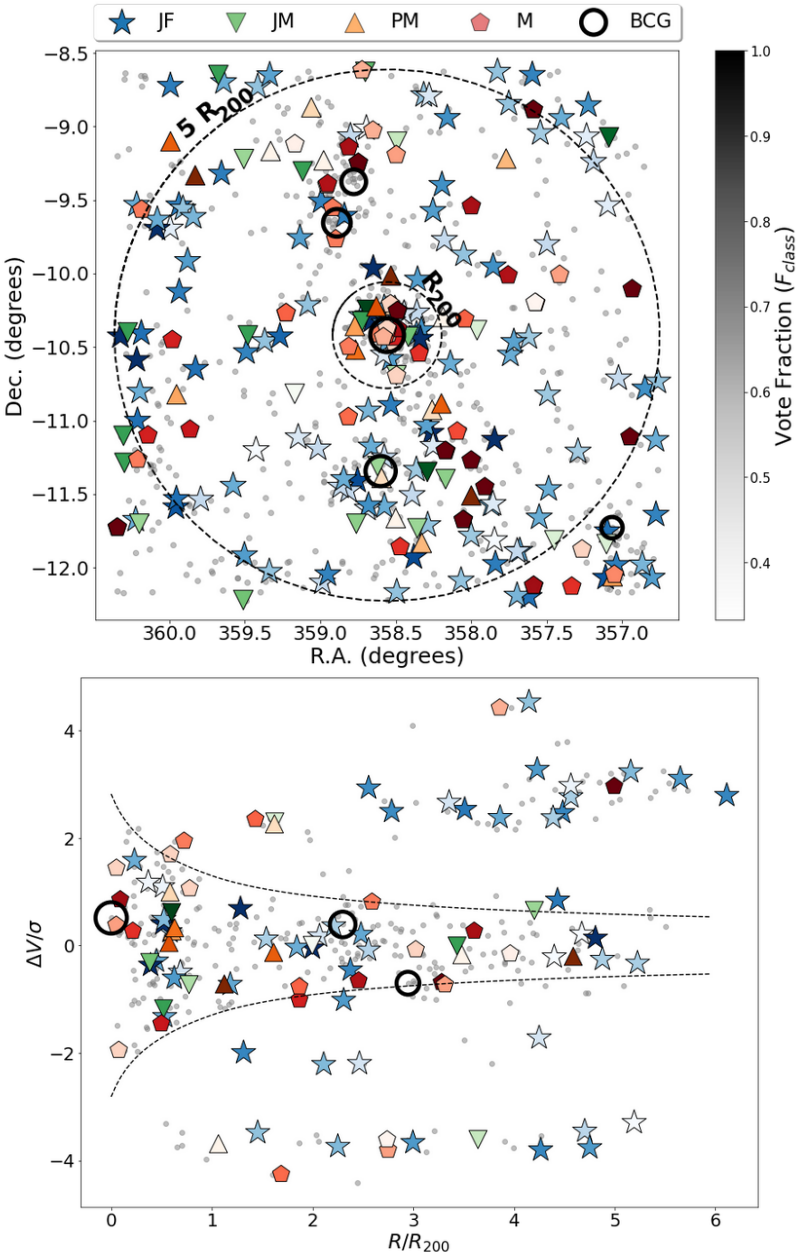

Figure 4.5: Distribution of all interacting galaxies identified in this work in the field of A2670. The final classifications (JF, JM, PM, and M) are marked with different symbols and colours. The corresponding vote fractions are indicated by the colour gradient, where the more confident classifications are shown with darker colours, using $F_{\rm RPS}$ for JF and JM galaxies and $F_{\rm GRAV}$ for PM and M galaxies. We use a grey colour bar to represent the gradient of the four colours. The small and large dashed circles indicate R_{200} and $5 \times R_{200}$, respectively. The 5 brightest galaxies are also plotted as larger filled circles, with the sizes reflecting their relative magnitudes (in the phase space we only visualize those with available velocity). At the bottom, we have the distribution of all interacting galaxies corresponding to spectroscopic members in the phase space diagram. In both panels, the grey points correspond to no interacting galaxies whose final classification was S, B, or N.

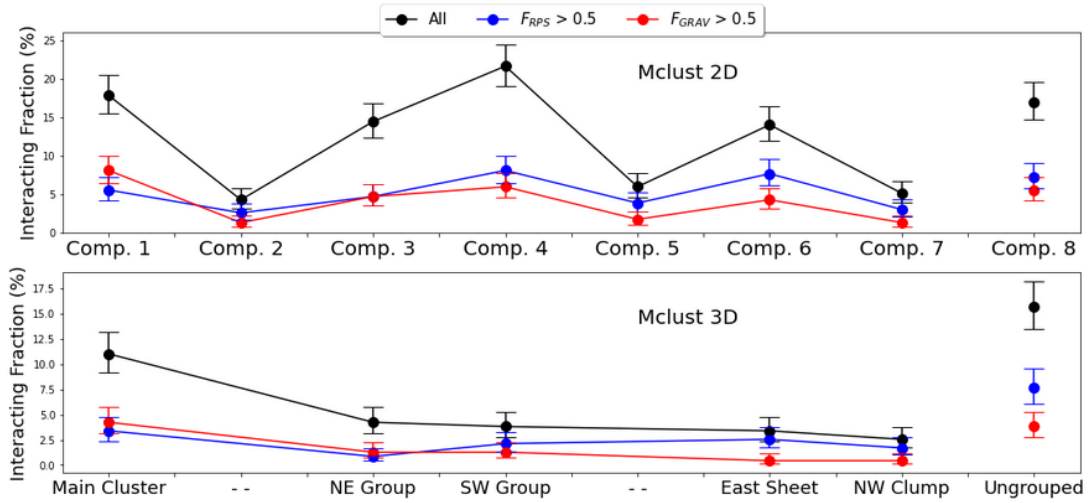

Figure 4.6: The interacting galaxy fraction is visualized for each component both 2D (top) and 3D (bottom) *mclust* analysis. The black dot line shows how many galaxies from the interacting galaxy sample (236) there are in each component. In blue, we can visualize how many galaxies from the interacting galaxy sample with a $F_{\rm RPS} > 0.5$ there are in each component. In red, we can visualize how many galaxies from the interacting galaxy sample with a $F_{\rm GRAV} > 0.5$ there are in each component. The error bars correspond to a binomial proportion confidence interval, using a Wilson interval.

We split the interacting galaxies into hydrodynamical and gravitational interactions by considering $F_{\rm RPS} > 0.5$ and $F_{\rm GRAV} > 0.5$, respectively (blue and red lines in Figure 4.6). We find that gravitational interactions (80 % mergers and 20% post mergers) are comparable with the RPS interactions in the cluster core within errors. Interestingly, in lower density structures towards the cluster outskirts (at $5 \times R_{200}$), the fraction of galaxies experiencing RPS ~ 4 times larger than that of gravitationally interacting galaxies (over 1σ significance). This implies that RPS could be the main responsible for galaxy transformations even in loose groups entering a cluster (pre-processing). We listed the interacting galaxies and galaxies with vote fractions for RPS and GRAV classes > 0.5 per substructure found by Mclust 2D (top) and 3D (bottom) (see table A.1).

To clearly see the extent of the environmental effects in the large-scale cluster environment we show in Figure 4.7 the fraction of interacting galaxies as a function of clustercentric distance, split by cause of interaction (RPS vs. GRAV). Interestingly, the fraction of RPS and GRAV galaxies are comparable at clustercentric distances lower than $\sim 2-4 \times R_{200}$. In the outskirts however (at $> 4 \times R_{200}$), the fraction of RPS galaxies increases significantly while the GRAV fraction remains low. This goes against the notion that RPS is stronger close to the cluster core (in regular clusters), where the ICM is denser and galaxies are travelling at great speeds.

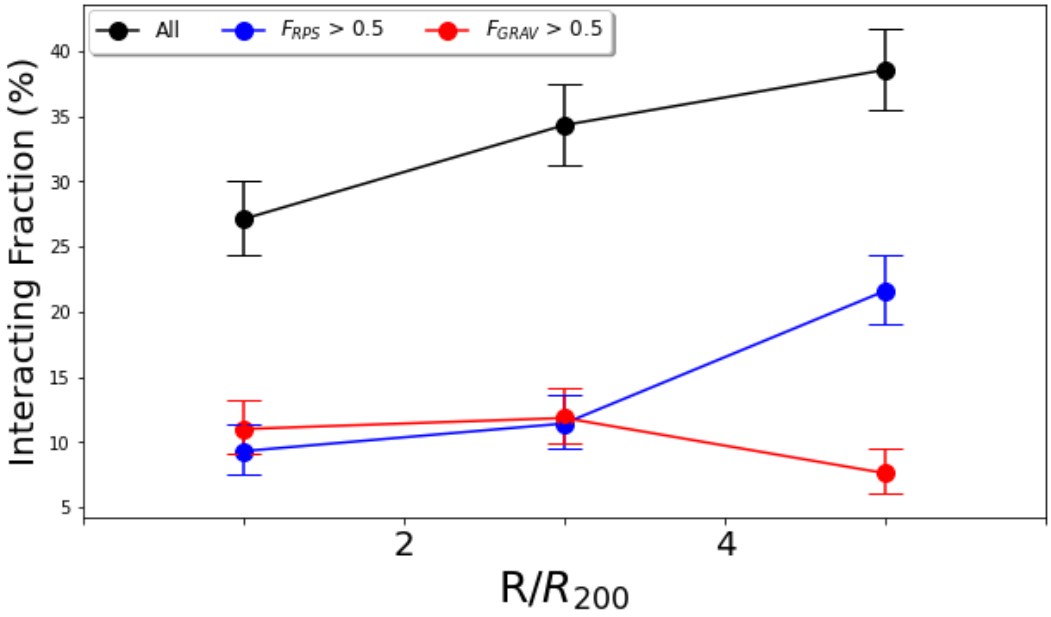

Figure 4.7: The interacting galaxy fraction in the function of the clustercentric distance of the system, with radial intervals of width $2\times R_{200}$. The black dot line shows how many galaxies from the interacting galaxy sample (236) there are in each interval of radius. In blue, we can visualize how many galaxies from the interacting galaxy sample with a $F_{\rm RPS} > 0.5$ there are in each interval. In red, we can visualize how many galaxies from the interacting galaxy sample with a $F_{\rm GRAV} > 0.5$ there are in each interval. The error bars correspond to a binomial proportion confidence interval, using a Wilson interval.

Also, galaxy-galaxy interactions are more easily triggered in lower-mass groups where relative velocities are not as high as in clusters, which makes our findings puzzling. Our findings reflect the complex interplay between the environmental effects in dynamically young clusters. On one hand pre-processing in galaxy groups can start to transform galaxies in the cluster outskirts, and on the other hand the merging cluster environment can trigger hydrodynamical and gravitational interactions, accelerating galaxy evolution (post-processing). Our results also highlight the importance of studying the outskirts of clusters galaxy transformations and quenching can start to occur.

Chapter 5

Work in progress

5.1 Tail directions for jellyfish galaxy candidates

The visual inspection gives us a several amount of interacting galaxies, more than 27% of the complete final sample. Among them, we found that $\sim 42 - 63\%$ of those being ram-pressure stripping (RPS) candidates with a total of 149 if we keep in mind JF + JM. In an attempt to further investigate how the cluster's dynamical state is affecting the galaxies and possibly enhancing RPS, we studied the distribution of tail directions for the RPS candidates with clear tails, so we decided to measure the tail direction for each jellyfish galaxy candidate. These tails are a good indicator of the stripping direction which should be opposite the direction of motion. It's also important to understand the dominion of the substructures over them and to check the dynamical behavior in this complex environment of substructures.

The tool to measure the tail direction of each jellyfish galaxy candidate consisted in running a second python 3.0 code[1] to display colour Legacy Survey images cuts and alongside the deep DECam in r-band images (when available). Six inspectors ran the code to perform the measurements, add a J class (1, 2, 3, 4, 5 like (Poggianti et al., 2016)) and a confidence for the tail (High Confidence: 2, Low Confidence: 1, No Confidence: 0). Since we are in front of a very large sample of jellyfish candidates, each inspector measured as many tails as possible.

The main aim of the inspector was to draw the tail angle with respect to the projected horizontal of BCG. With this parameter plus the BCG angle, which correspond to the angle

[1] https://github.com/FrancoPiraino/Tails_Measurements_Codes.git

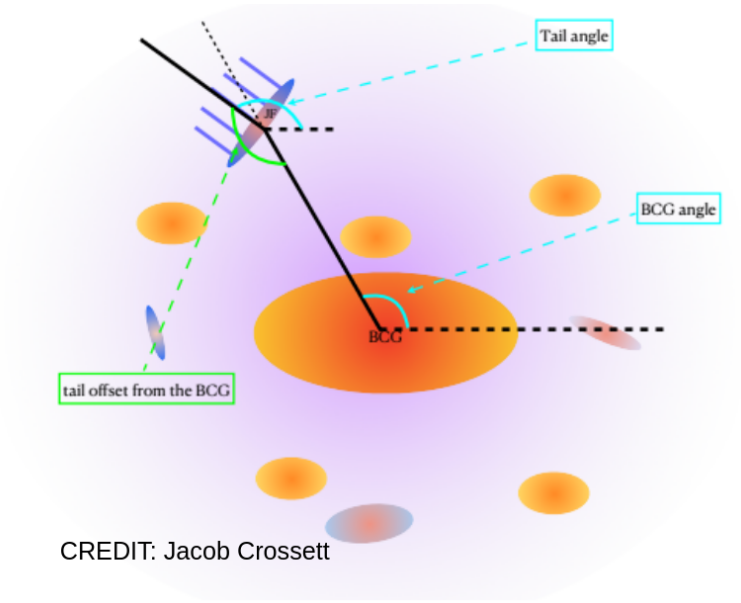

Figure 5.1: Diagram showing the different angles measured to define the jellyfish tail direction. The tail angle respect to the projected horizontal of BCG plus the BCG angle, which correspond to the angle between the same horizontal and the direction to the galaxy give us the angle between the stripping feature direction and the direction toward the cluster centre, the tail offset from the BCG. Image Credit: Jacob Crossett.

between the same horizontal an the direction to the galaxy, we will be able to compute the angle between the stripping feature direction and the direction toward the cluster centre, the tail offset from the BCG (Figure 5.1). As (Roberts & Parker, 2020), the tail offset angle of each JF candidate may be a good parameter to check what galaxies have a tail pointing toward to the cluster centre or away from it and that could indicate us if we have a cluster where the almost stripped galaxies are falling to or going back from the centre.

Then, after each inspector has measured the tail angle for each galaxy, an average tail angle among all the inspectors is computed. Whose average is obtained removing some tails angles that maybe have the largest average angle difference with respect to the other measured tail angles by other inspectors. The flowchart from Figure 5.2 shows the steps to obtain that average tail angle with its confidence. In short, we have tail angles drawn by N people for each jellyfish candidate. If at least half of N people see a tail confidence greater than 0, we compute an angle difference (θ_{ij}) between each of the angles, else the galaxy will be considered to not have a tail. Then, we check if there is an angle difference $\theta_{ij} > 45$. If so, we remove the angle (i or j) with the largest average angle difference with respect to the other angles. Each time that one of those angles is removed, we check if the remaining angles are more than the half of people

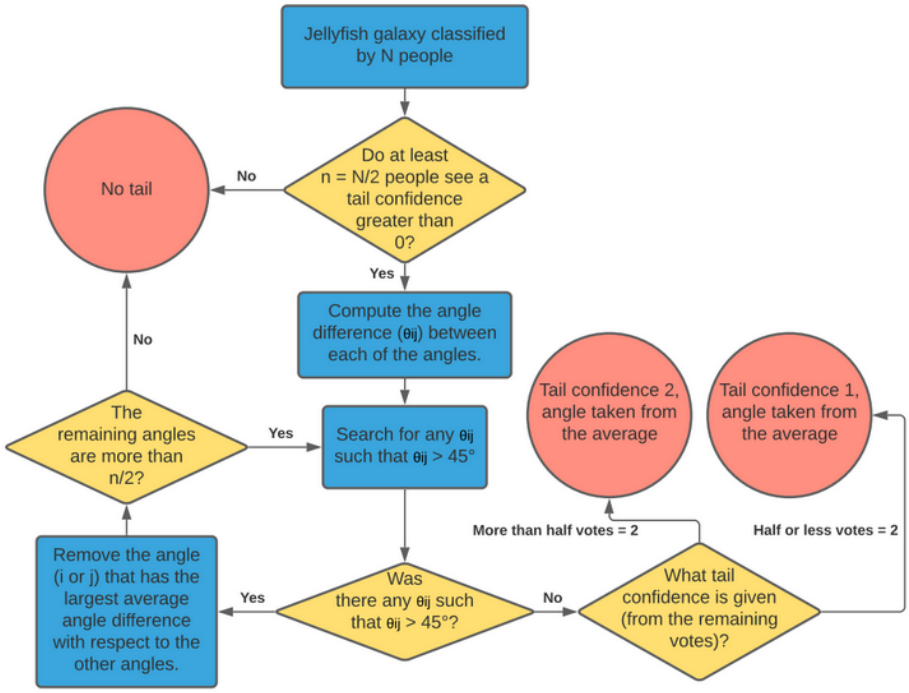

Figure 5.2: Flowchart to obtain the average tail angle with its associated confidence. Credit: Salinas et al. in preparation. Based on the work by (Kolcu et al., 2022)

that see a tail confidence greater than 0. Else, the galaxy will be considered to not have a tail. After eliminating the cases where $\theta_{ij} > 45^o$, we compute an average tail between the remaining angles and an associated confidence as follow: if more than half of the remaining tail angles have a high confidence (2) the final average tail has a high confidence = 2, but if half or less remaining tail angles have a high confidence, the final average tail has a low confidence = 1.

In Figure 5.3 we show a few examples to follow the flowchart. For example, for the first galaxy (top left), we have 4 tail angles (yellow, red, green, blue) drawn with a confidence of > 0 (1, 2, 2, 1). In this case, with an offset of 334.0 degrees, the blue arrow is the only one that has a max average offset $\theta_{ij} > 45^o$ respect to the other tail angles. So, we don't consider the blue arrow (top right) and we compute an average with the remaining tail angles (yellow, red, green) with confidences (1, 2, 2) respectively. Since more than half remaining tail angles have a high confidence (2) the final average tail has a high confidence = 2 (white).

For all the galaxies whose average tail might be measured with its own confidence, the tail offset angle was computed. In the Figure 5.4, an histogram of the average tail angle between the stripping feature direction and the direction toward the cluster can be visualized. Galaxies

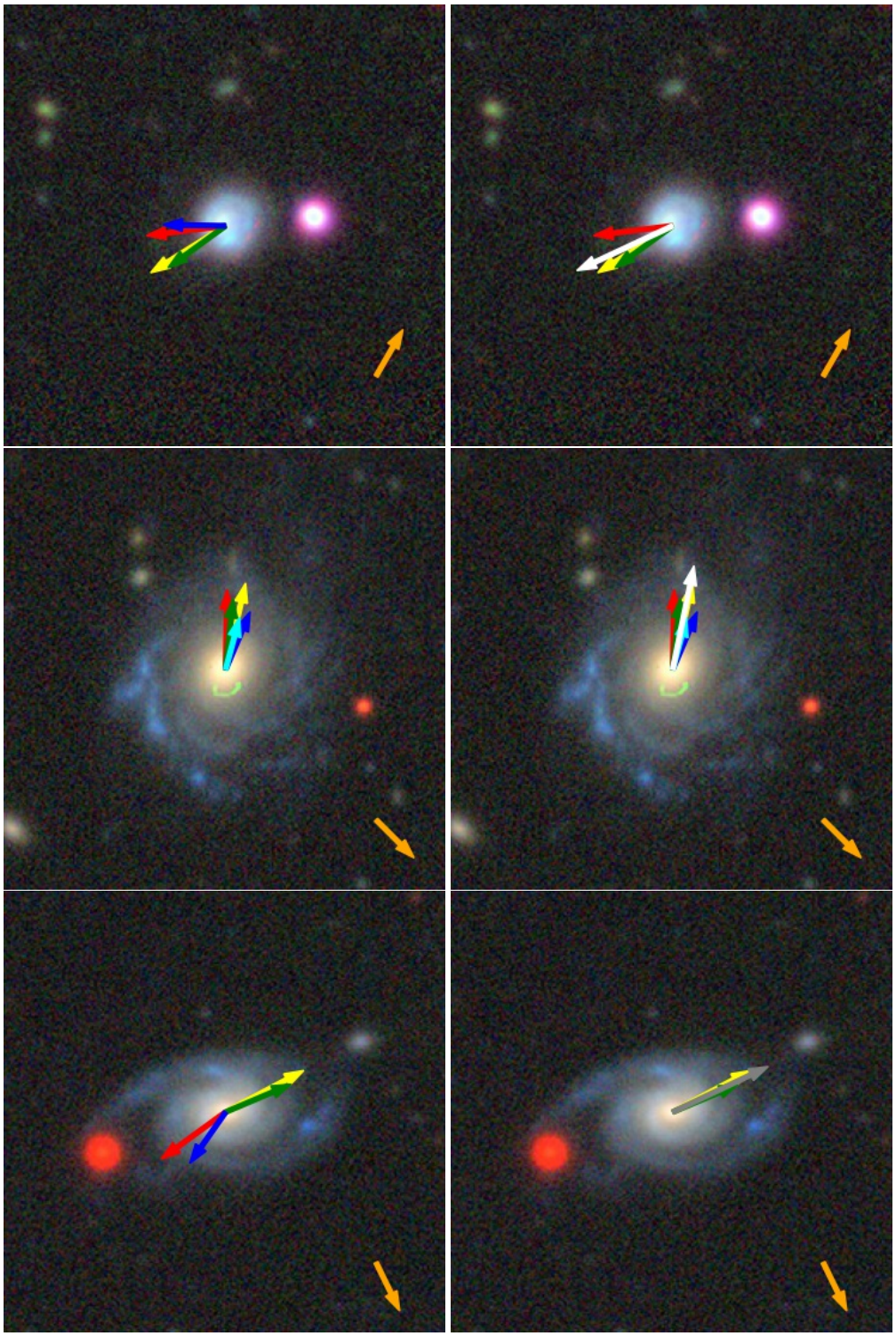

Figure 5.3: Tail angles plotted on cutout images from LS. **LEFT:** Before the flowchart with all the tail angles. **RIGHT:** After the flowchart, with some tail angles removed and the final average tail angle with its confidence. High confidence (white), Low confidence (grey). Orange arrow direction to the cluster centre.

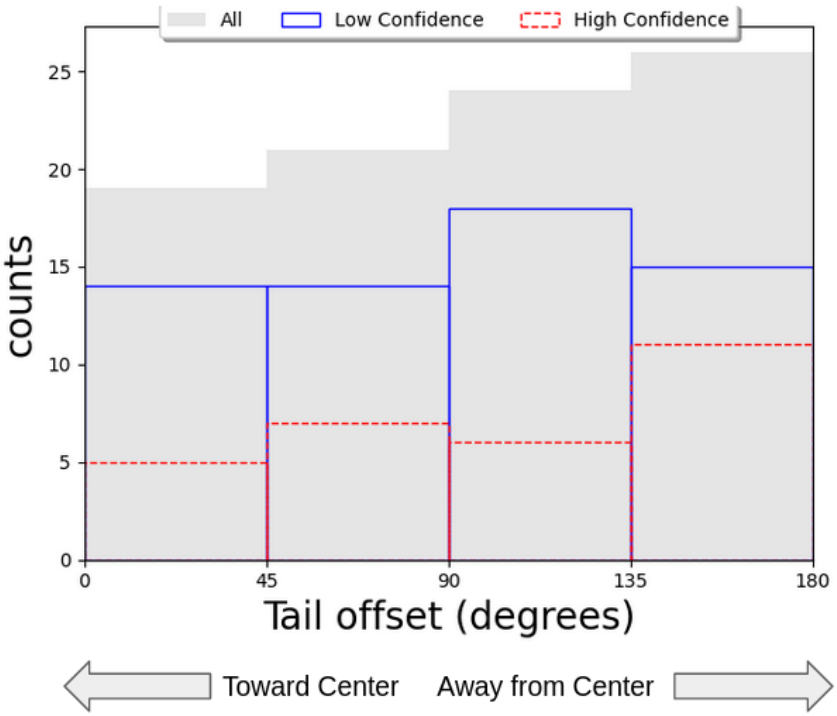

Figure 5.4: Histogram of the average tail angle between the stripping feature direction and the direction toward the cluster can be visualized. Galaxies that show angles between 135 - 180 degrees, its tails are pointing away from the cluster centre. Galaxies that show angles between 0 - 45 degrees, its tails are pointing toward the cluster centre. In blue we have average tail offset with low confidence and in red we have average tail offset with high confidence.

that show angles between 135 - 180 degrees, its tails are pointing away from the cluster centre. Galaxies that show angles between 0 - 45 degrees, its tails are pointing toward the cluster centre. In blue we have average tail offset with low confidence and in red we have average tail offset with high confidence.

Chapter 6

Discussion

In Chapter 4 we found a total of 236 interacting galaxies in A2670 and its surroundings. The majority of those (42-63%) are likely being disturbed by ram-pressure stripping (i.e. are "jellyfish" galaxies), while the rest are likely disturbed gravitationally. Our study reports the highest number of jellyfish candidates to date in a single system ($\sim 100-149$, considering a range of uncertainties). Prior to this study, the record was held by (Roman-Oliveira et al., 2019; Ruggiero et al., 2019) who claim to have found 70 jellyfish candidates in a similar system: A901/2, composed of two galaxy clusters and two smaller groups in route of collision with each other simultaneously. These two works combined could suggest that dynamically young clusters can indeed enhance ram-pressure stripping (see also Owers et al., 2012). These single-system studies contradict a recent study (Lourenço et al., submitted) aiming at quantifying the effect of cluster dynamical state in the formation of jellyfish galaxies using a large homogeneous sample from (Poggianti et al., 2016). The study finds no correlation between the fraction of jellyfish galaxies and cluster dynamical stage but their results could be affected by the limited area covered by the observations ($0.7 \times R_{200}$). Our findings thus motivate larger-sample studies such as that of Lourenço et al. (submitted) but extending well beyond the virial radius of the clusters. In fact, hydrodynamical simulations suggest gas stripping can start to take place at $\sim 5 \times R_{200}$ (Bahé et al., 2013) and that the peak of RPS is located around the virial radius Pallero et al. (2022).

To understand how unique A2670 is, we compare our results with statistical studies of the incidence of optically-selected RPS candidates in clusters. The most recent one is (**?**)Vul-

cani2022, who found that these galaxies represent $\sim 15-20\%$ of the infalling population of blue spiral galaxies (within roughly the virial region) in a large sample of mostly relaxed clusters from the WINGS/OmegaWINGS surveys. In order to compare in a meaningful way our results with this study we consider only the blue galaxies in A2670 (those below 1σ from the red sequence line in Fig. C.1) and assume they are mostly spirals. We find that between $\sim 22-32\%$ of the blue members of A2670 (up to $5 \times R_{200}$) are being affected by RPS, which is indeed higher than what is found by (Vulcani et al., 2022). The fraction of blue RPS candidates in A2670 decreases only very mildly (21-30%) when we restrict the sample to $1 \times R_{200}$ (closer to the area explored by Vulcani et al., 2022).

The most interesting is the distribution of the interacting galaxies in A2670. While many of them are found near the inner part of the cluster, many of them are distributed in the outer parts, in and around the substructures, especially along the cluster merger axis (NE-SW). In fact, the components that form this axis are in the same velocity located into the escape velocity (Figure 3.1, bottom), where part of the cluster is virialized, giving us a possibility to derive the mass for these structures, using the available radial velocity of their members. The compute of their mass could support the idea that the galaxies and RPS candidates are following these structures, as well as the brightest galaxies distributed across the NE-SW axis (see Figure 3.1).

We interpret the interacting galaxies in groups as a consequence of pre-processing and those in between the structures as post-processing. Specifically, almost 40% of the interacting galaxies (mostly RPS candidates) are located well beyond the virial region close to $\sim 5 \times R_{200}$, supporting the notion that gas removal can start very far from the virial region of the cluster, especially near filaments (Bahé et al., 2013). It is intriguing however that the RPS galaxies are increasingly more common at increasing clustercentric distance, which contradicts the notion that RPS is stronger near the cluster core. On the other hand, gravitationally interacting galaxies are more common close to the cluster core, which is not expected in a regular cluster due to the higher relative motions of galaxies in clusters. In merging systems however asymmetric galaxies have been found to be more common near the core (e.g. Kleiner et al., 2014), and indeed the distribution of merging and post-merger galaxies in A2670 is concentrated along the merger axis. We interpret these results as an effect of post-processing at play, where the dynamically active environment and in particular the merger of the different structures enhances galaxy-galaxy interactions as well as RPS in unexpected regions.

To better separate the effects of pre- and post-processing in a follow-up study we will analyze the direction of the tails in the RPS candidates which reflect their direction of motion.

Chapter 7

Summary and Conclusions

Galaxy clusters are among the largest known structures, and they continue to grow through the accretion of galaxies from filaments, groups and even other clusters. It is thus expected that the evolution of galaxies depends on interactions mechanism with their evolving environments, which can accelerate the formation and evolution of galaxies (Boselli & Gavazzi, 2006). Recent studies seem to show that ram-pressure stripping (Gunn & Gott, 1972) is a very important mechanism in clusters (Vulcani et al., 2022; Jaffé et al., 2015), however the most dominant mechanism in pre- and post-processing scenarios of galaxies before falling into large clusters are not clear yet (Dressler, 2004; Cortese et al., 2006; Hou et al., 2014; Boselli et al., 2014; Jaffé et al., 2016; Haines et al., 2015; Fujita et al., 1999; Domainko et al., 2006; Kapferer et al., 2009; Hwang & Lee, 2009; Ma et al., 2010; Owers et al., 2012; Stroe et al., 2014; Rawle et al., 2014; Stroe et al., 2015; McPartland et al., 2016; Ebeling & Kalita, 2019; Kelkar et al., 2020).

In order to understand the complex role of the evolving environment in galaxy transformations (in particular the role of *pre* and *post-processing*), we studied the properties of galaxies in a large area centred on the interacting system A2670, a nearby massive cluster of galaxies. We looked for signs of transformations in galaxies not only in the inner part of the cluster where many galaxy evolution studies focus, but also in the infall regions of the cluster up to $\sim 5\times R_{200}$ where galaxies are falling in from the cosmic web.

We first built a complete and homogeneous spectro-photometric catalogue using public data from LS DR9 and the SDSS when available for a $3.6^\circ \times 3.6^\circ$ region centred on A2670. We select photometric and spectroscopic members by considering galaxy colours and redshifts

respectively within a magnitude limit of $M_B < -20$.

We then studied the distribution and clustering of galaxies in this large region containing the cluster and its infall regions using different 2D and 3D techniques, including a Dressler Schectman's test and a gaussian mixture model technique (*mclust*) in 2D and 3D. We could robustly confirm that the cluster is interacting and has a significant amount of substructure, not only in the core (as found by Hobbs & Willmore, 1997; Fujita et al., 2006; Sheen et al., 2012) but out to the outskirts. The substructure analysis clearly identified the main cluster at the centre of the field, accompanied by a large group towards the NE, a group towards the SE, 2 lower-density high-velocity substructures far from the cluster centre, and other less-defined structures. Our results are consistent with similar but smaller-area studies of this cluster (e.g. López-Gutiérrez et al., 2022), that have found at least three groups running along the NE-SW axis with a high probability to be merging with the main cluster. Further confirmation comes from the 5 brightest galaxies in the system, which are aligned with the merging axis.

After characterizing the environment in this cluster, we visually inspected the member galaxies in search of signatures of ongoing or past gravitational (mergers and post-mergers) and hydrodynamical interactions (RPS). We used optical images from LS as well as our own deeper DECam data. We developed our own interactive tool to allow different users to classify the galaxies, and a method to combine the votes into a final category with associated uncertainty. Our tools and methods can serve as a reference for ongoing or future larger studies aiming at identifying interacting galaxies in large optical datasets visually (e.g. the ongoing citizen science project "*Fishing for Jellyfish Galaxies*"[1].

A total of 236 interacting galaxies were found in A2670 and its surroundings. Of those, 149 are jellyfish candidates, while the rest are likely disturbed gravitationally. Our study reports the highest number of jellyfish galaxies to date in a single system, supporting previous claims that cluster mergers could enhance ram-pressure, and trigger galaxy interactions.

When studying the distribution of the interacting galaxies in A2670 we find that while many of them agglomerate near the inner part of the cluster, most of them are located in the outer parts, in and around the substructures, with a high concentration in the merging axis of the A2670 system. In particular, almost 40% of the interacting galaxies (mostly RPS candidates) are located well beyond the virial region at $> 4 \times R_{200}$ (in all directions), highlighting the important role of pre-processing must have to transform galaxies prior to entering the cluster. This finding also supports the (theoretical) notion that gas removal in particular can start very far from the virial region of the cluster. On the other hand, gravitationally interacting galaxies are more common close to the cluster core and along the merging axis, which could be a consequence of

[1] https://www.zooniverse.org/projects/cbellhouse/fishing-for-jellyfish-galaxies

the cluster merger (post-processing).

Our study showcases the importance of pre- and post-processing of galaxies in actively growing clusters and presents a motivation for larger homogeneous studies of galaxies within their large scale-environment.

Finally, to investigate whether the galaxies with signatures of RPS are experiencing gas removal due to radial accretion towards the cluster or due to pre-processing in groups being accreted into the cluster, the direction of the jellyfish galaxy tails was measured with respect to the center of the cluster for all the jellyfish candidates. We find that, while most galaxies have tails pointing away from the center (see histogram in Figure 5.4), the distribution is much flatter than for regular clusters (Roberts & Parker, 2020), which confirms the complex orbits of the galaxies in this system.

Chapter 8

Future work and perspectives

- The work presented in this thesis has several components, namely detailed substructure analysis and identification and characterization of interacting galaxies. The last part of the thesis was focused on measuring the tail direction of the jellyfish galaxy candidates to analyze this measurement of tails. We are yet to analyze the tail directions with respect to the substructures and not only to the center of the cluster, to investigate whether if the direction of tails is determined by the substructures or by the main cluster.

- We also hope to use the tools developed in this thesis to extend the study of A2670 to another much larger sample of clusters with different states of interaction, and including data from other wavelengths such as radio observations (López-Gutiérrez et al., 2022) that allow us to evaluate the HI gas content of the galaxies.

- Finally, this work is a pilot study which hopes to serve as a pathway for future larger studies. In particular, the upcoming 4MOST instrument which will carry out several spectroscopic legacy surveys such as CHANCES, from which environment and galaxy properties will be well characterized. In addition, large optical datasets are allowing the identification of ever greater numbers of interacting galaxies through citizen science (e.g. "Fishing for jellyfish galaxies" in Zooniver.org)[1] and larger deeper surveys will soon reveal even larger samples (e.g S-PLUS, LSDR10, LSST in the future).

[1] https://www.zooniverse.org/projects/cbellhouse/fishing-for-jellyfish-galaxies

Appendix A

Mclust test

In this appendix you can find information about models that *mclust* provides us for our analysis. The results of the selection of the best model through BIC criterion. In addition, we show a table for the fractions of galaxies per component found by *mclust* analysis.

A.1 Models

According (Scrucca et al., 2016), for a multidimensional analysis (both 2D and 3D), *mclust* provides 14 models with varying geometry depending on its distribution, volume, shape and orientation (see Figure A.1 and A.2).

A.2 Choosing the best model for 2D and 3D mclust analysis

In Figure A.3, we can visualize the BIC in function of number of components for each of the 14 Gaussian models for our 2D and 3D analysis.

Model	Σ_k	Distribution	Volume	Shape	Orientation
EII	$\lambda \boldsymbol{I}$	Spherical	Equal	Equal	—
VII	$\lambda_k \boldsymbol{I}$	Spherical	Variable	Equal	—
EEI	$\lambda \boldsymbol{A}$	Diagonal	Equal	Equal	Coordinate axes
VEI	$\lambda_k \boldsymbol{A}$	Diagonal	Variable	Equal	Coordinate axes
EVI	$\lambda \boldsymbol{A}_k$	Diagonal	Equal	Variable	Coordinate axes
VVI	$\lambda_k \boldsymbol{A}_k$	Diagonal	Variable	Variable	Coordinate axes
EEE	$\lambda \boldsymbol{D}\boldsymbol{A}\boldsymbol{D}^\top$	Ellipsoidal	Equal	Equal	Equal
EVE	$\lambda \boldsymbol{D}\boldsymbol{A}_k\boldsymbol{D}^\top$	Ellipsoidal	Equal	Variable	Equal
VEE	$\lambda_k \boldsymbol{D}\boldsymbol{A}\boldsymbol{D}^\top$	Ellipsoidal	Variable	Equal	Equal
VVE	$\lambda_k \boldsymbol{D}\boldsymbol{A}_k\boldsymbol{D}^\top$	Ellipsoidal	Variable	Variable	Equal
EEV	$\lambda \boldsymbol{D}_k\boldsymbol{A}\boldsymbol{D}_k^\top$	Ellipsoidal	Equal	Equal	Variable
VEV	$\lambda_k \boldsymbol{D}_k\boldsymbol{A}\boldsymbol{D}_k^\top$	Ellipsoidal	Variable	Equal	Variable
EVV	$\lambda \boldsymbol{D}_k\boldsymbol{A}_k\boldsymbol{D}_k^\top$	Ellipsoidal	Equal	Variable	Variable
VVV	$\lambda_k \boldsymbol{D}_k\boldsymbol{A}_k\boldsymbol{D}_k^\top$	Ellipsoidal	Variable	Variable	Variable

Figure A.1: Parametrization of the within-group covariance matrix Σ_k for multidimensional data available in the mclust package, and the corresponding geometric characteristic

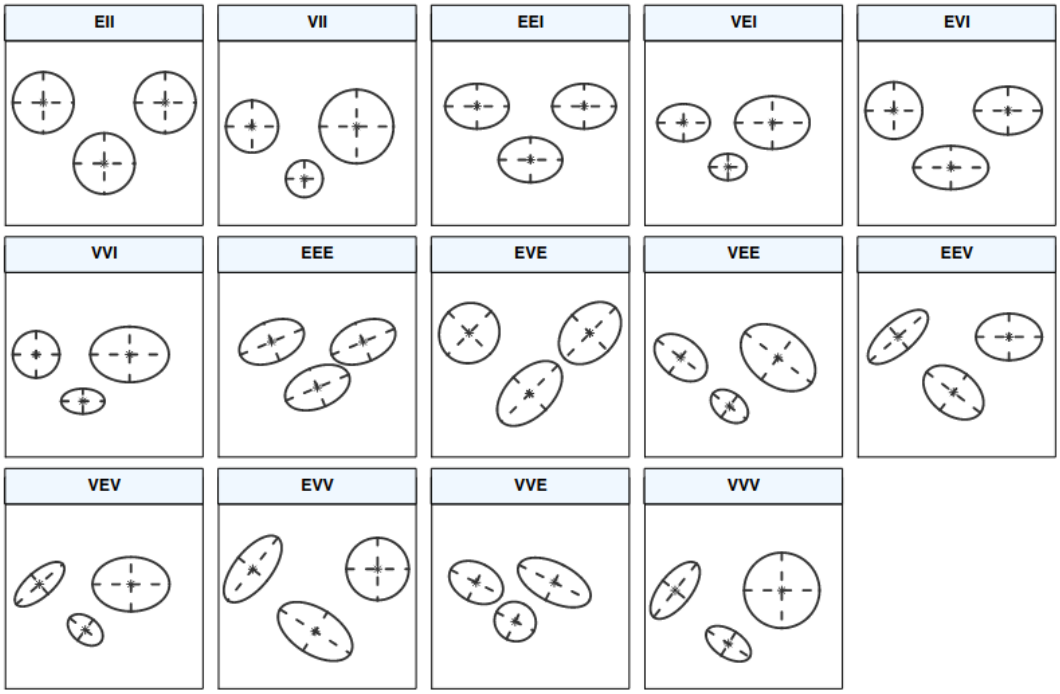

Figure A.2: Ellipses of isodensity for each of the 14 Gaussian models obtained by eigen-decomposition in case of three groups in two dimensions.

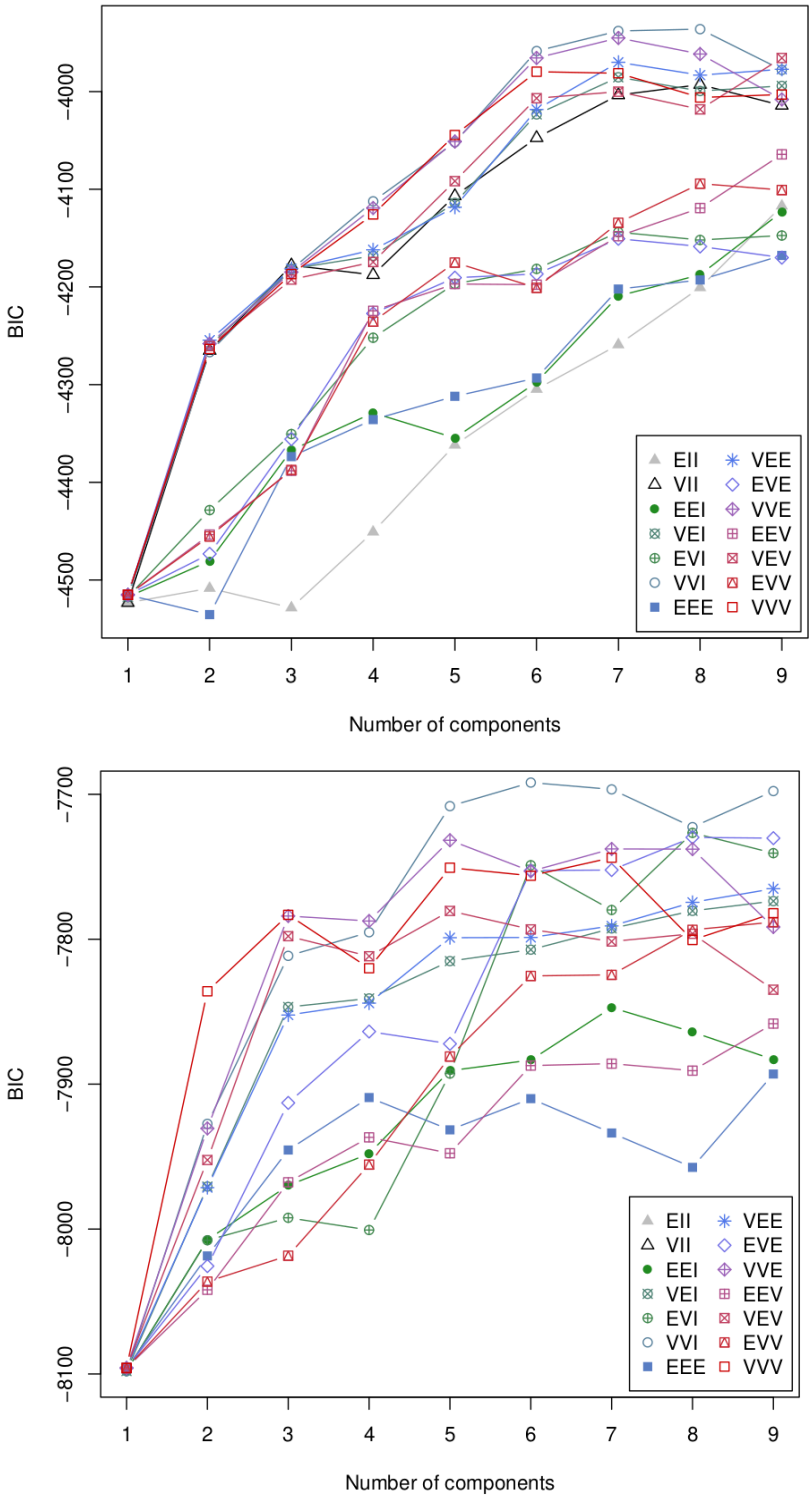

Figure A.3: In Figure A.3, we can visualize the BIC in terms of the number of components for each of the 14 Gaussian models. In the top, we see the results for 2D analysis, where the model that converged to a maximum |BIC| corresponds to the VVI model with 8 components. In the bottom, we see the results for 3D analysis, where the model that converged to a maximum |BIC| corresponds to the VVI model with 6 components.

Mclust 2D	Comp. 1	Comp. 2	Comp. 3	Comp. 4	Comp. 5	Comp. 6	Comp. 7	Comp. 8
All	146	46	144	162	61	96	36	152
Interacting	42	10	34	51	33	14	12	40
$F_{\mathrm{RPS}} > 0.5$	13	6	11	19	18	9	7	17
$F_{\mathrm{GRAV}} > 0.5$	19	3	11	14	10	4	3	13
Mclust 3D	Main Cluster	—	NE Group	SW Group	—-	East Sheet	NW Clump	Ungr.
All	102	—	76	48	—	21	21	108
Interacting	26	—	10	9	—	8	6	37
$F_{\mathrm{RPS}} > 0.5$	8	—	2	5	—	6	4	18
$F_{\mathrm{GRAV}} > 0.5$	10	—	3	3	—	1	1	9

Table A.1: Total number of galaxies per component, for both 2D (top) and 3D (bottom) analysis. In the first row, we see the distribution of all photometric cluster members per component. In the second row, we see the total number of interacting galaxies per component. In the third row, we see the total number of interacting galaxies with a vote fraction F_{RPS} more than 0.5. In the fourth row, we see the total number of interacting galaxies with a vote fraction F_{GRAV} more than 0.5.

A.3 Fraction of galaxies per components in *mclust* analysis

In table A.1 we can see the total number of galaxies, interacting galaxies, and galaxies with vote fractions for RPS and GRAV classes > 0.5, for each of the substructures found by Mclust 2D (top) and 3D (bottom).

Appendix B

Interacting galaxies

In table B.1 we list the final classifications for the 236 interacting galaxies found in this work, and in Figure B.1 we show the corresponding Legacy Survey images for each of them.

Table B.1: The first column of the table indicates the ID of the galaxies in our catalogue. The second and third column contain the coordinates of the galaxies in degrees, R.A. and Dec., respectively. The fourth column contains the final category assigned to the galaxy using the different votes of each classifier. The fifth, sixth and seventh column contain the vote fraction for each class, F_{RPS}, F_{GRAV} and $F_{\mathrm{N.I.}}$, respectively.

ID	R.A.	Dec.	Final Category	F_{RPS}	F_{GRAV}	$F_{\mathrm{N.I.}}$
7	358.49480	-10.69413	M	0.100	0.500	0.400
9	358.53481	-10.57998	JF	0.714	0.143	0.143
13	358.49525	-10.69191	JM	0.300	0.700	0.000
28	358.72571	-10.28808	JF	0.600	0.000	0.400
30	358.69096	-10.24600	JM	0.700	0.300	0.000
33	359.08307	-10.21275	JF	0.600	0.000	0.400
34	358.26567	-11.08203	JF	1.000	0.000	0.000
35	357.02268	-10.71181	JF	0.500	0.000	0.500
40	358.04252	-10.30951	M	0.000	0.714	0.286
43	359.01519	-11.18858	JF	0.500	0.500	0.000

Table B.1 continued from previous page

52	358.50602	-10.21325	PM	0.000	0.600	0.400
67	358.53431	-10.20781	M	0.000	0.500	0.500
76	358.54199	-10.40703	M	0.000	0.500	0.500
82	357.54160	-9.04424	JF	0.571	0.000	0.429
83	359.82906	-9.33143	PM	0.000	1.000	0.000
84	358.66306	-11.17487	JF	0.667	0.333	0.000
87	358.68413	-10.28220	JF	1.000	0.000	0.000
104	358.15778	-8.94071	JF	0.750	0.250	0.000
105	358.81385	-10.97464	M	0.300	0.700	0.000
110	358.55513	-10.38638	M	0.071	0.929	0.000
119	359.22704	-10.26874	M	0.000	0.833	0.167
124	357.57138	-10.19963	M	0.000	0.600	0.400
125	358.77058	-10.35581	PM	0.143	0.714	0.143
127	359.11609	-9.30547	JM	0.500	0.333	0.167
129	358.99402	-9.50826	JF	0.786	0.214	0.000
131	359.22668	-10.26791	M	0.000	0.714	0.286
133	358.48580	-10.25292	M	0.143	0.857	0.000
134	358.53200	-10.01322	PM	0.000	1.000	0.000
135	359.82718	-10.64715	JF	0.833	0.167	0.000
136	357.40130	-8.94153	JF	0.667	0.000	0.333
137	358.72339	-10.32546	JM	0.500	0.167	0.333
140	358.17773	-9.77037	JF	0.500	0.000	0.500
145	358.35993	-10.26360	JF	0.500	0.000	0.500
157	358.53183	-10.89376	JF	0.800	0.000	0.200
160	358.19361	-9.39617	JF	0.750	0.083	0.167
164	358.91854	-9.55243	M	0.000	0.667	0.333
166	358.65902	-10.31880	JF	1.000	0.000	0.000
168	359.16952	-10.81769	JM	0.100	0.500	0.400
170	358.25328	-9.57316	JF	0.714	0.143	0.143
171	358.62848	-10.22337	PM	0.000	0.857	0.143
174	358.25881	-10.92653	PM	0.417	0.583	0.000
177	358.57615	-10.23046	JF	0.667	0.000	0.333
179	358.97778	-9.22967	PM	0.300	0.500	0.200
186	358.18622	-10.29496	PM	0.000	0.500	0.500

Table B.1 continued from previous page

190	357.49733	-9.79894	JF	0.500	0.000	0.500
194	358.95637	-9.39853	M	0.000	0.500	0.500
195	358.41611	-10.42991	JM	0.400	0.600	0.000
196	358.57647	-10.33747	JF	0.700	0.100	0.200
198	358.52930	-10.42132	M	0.000	0.500	0.500
204	358.35536	-10.04006	JF	0.714	0.000	0.286
211	358.76653	-10.51664	PM	0.000	0.800	0.200
217	357.57541	-10.19743	M	0.200	0.400	0.400
218	358.29533	-11.03420	JF	0.700	0.300	0.000
222	359.93771	-9.53557	JF	0.800	0.200	0.000
224	359.87962	-9.91379	JF	0.714	0.000	0.286
227	358.48842	-10.38032	M	0.000	0.800	0.200
234	358.49079	-9.10317	JM	0.250	0.417	0.333
236	357.23466	-9.06688	JF	0.400	0.200	0.400
239	358.81129	-10.49654	M	0.000	0.667	0.333
243	358.19735	-10.88310	PM	0.000	0.833	0.167
252	358.68154	-10.93081	JF	0.643	0.214	0.143
260	358.44444	-10.27081	JF	0.429	0.143	0.429
263	358.65125	-9.02668	M	0.286	0.571	0.143
266	359.36878	-10.45888	JF	0.600	0.200	0.200
267	356.84795	-10.78096	JF	0.750	0.250	0.000
268	358.84038	-9.60657	JF	0.800	0.000	0.200
273	358.36167	-10.41159	JF	0.700	0.100	0.200
277	358.32949	-10.38424	JF	0.750	0.083	0.167
283	358.74814	-9.24707	M	0.000	1.000	0.000
284	358.64907	-9.96356	JF	1.000	0.000	0.000
285	358.58131	-10.55010	JF	0.417	0.250	0.333
286	357.41333	-10.00713	M	0.000	0.600	0.400
287	359.48998	-10.53390	JF	0.786	0.071	0.143
290	359.91075	-9.55799	JF	0.600	0.000	0.400
291	357.96055	-10.38551	JM	0.200	0.400	0.400
293	358.81121	-9.13957	M	0.083	0.917	0.000
296	358.57536	-10.41544	M	0.000	0.600	0.400
297	359.16884	-9.11901	M	0.250	0.417	0.333

Table B.1 continued from previous page

304	359.99483	-9.69295	JF	0.400	0.200	0.400
305	357.75500	-10.01107	M	0.100	0.900	0.000
306	359.65528	-9.31968	JF	0.800	0.000	0.200
310	358.31430	-8.78573	JF	0.600	0.000	0.400
320	357.58919	-8.88501	M	0.000	1.000	0.000
325	357.74023	-10.55045	JF	0.667	0.333	0.000
330	357.09422	-9.53560	JF	0.400	0.400	0.200
340	359.50640	-9.22128	JM	0.333	0.333	0.333
342	357.22353	-8.85431	JF	0.750	0.083	0.167
348	357.85426	-9.95125	JF	0.750	0.250	0.000
355	357.61752	-10.43200	JF	0.583	0.417	0.000
356	359.41487	-8.72869	JF	0.600	0.000	0.400
358	358.27844	-8.79123	JF	0.429	0.286	0.286
362	359.99389	-8.72214	JF	0.800	0.200	0.000
364	357.75039	-8.84456	JF	0.600	0.000	0.400
371	356.80080	-12.06758	JF	0.714	0.143	0.143
373	356.86549	-11.97720	JF	0.643	0.357	0.000
383	357.06170	-12.05838	PM	0.143	0.714	0.143
384	357.05070	-12.04698	M	0.357	0.643	0.000
386	357.03676	-11.98044	JF	0.800	0.000	0.200
388	357.10855	-12.06815	JF	0.900	0.100	0.000
393	356.77461	-11.63899	JF	0.786	0.071	0.143
403	357.10259	-11.83976	JM	0.200	0.600	0.200
406	357.26481	-11.87509	M	0.000	0.500	0.500
407	357.09747	-11.75161	JF	0.833	0.167	0.000
417	357.33292	-12.12778	M	0.200	0.800	0.000
418	357.61599	-12.19887	JF	0.833	0.000	0.167
419	357.58502	-12.12266	M	0.143	0.857	0.000
420	357.58596	-12.12182	M	0.071	0.929	0.000
421	357.69533	-12.18937	JF	0.643	0.071	0.286
425	357.83868	-11.97430	JF	0.800	0.200	0.000
427	358.06661	-12.08680	JF	0.600	0.000	0.400
429	357.44842	-11.81442	JM	0.200	0.800	0.000
431	357.67743	-11.88525	JF	0.700	0.100	0.200

Table B.1 continued from previous page

432	357.69505	-11.88823	JF	0.500	0.333	0.167
434	357.54904	-11.65835	JF	0.667	0.167	0.167
436	357.84524	-11.81301	JF	0.333	0.333	0.333
441	357.99959	-11.78091	JF	0.583	0.083	0.333
442	357.86771	-11.57126	JF	0.667	0.000	0.333
443	357.85516	-11.56616	JF	0.417	0.250	0.333
446	358.05106	-11.67363	M	0.000	1.000	0.000
447	358.05252	-11.67492	M	0.000	1.000	0.000
449	357.99896	-11.50903	PM	0.000	1.000	0.000
452	356.77531	-11.13127	JF	0.667	0.000	0.333
459	356.94682	-11.11188	M	0.000	1.000	0.000
460	357.29145	-11.20970	JF	0.571	0.000	0.429
461	356.76275	-10.73378	JF	0.600	0.200	0.200
463	357.48648	-11.46494	JF	0.667	0.333	0.000
470	357.90925	-11.45150	M	0.000	1.000	0.000
475	358.16944	-11.39817	JM	0.357	0.357	0.286
478	357.99938	-11.26975	M	0.000	1.000	0.000
479	357.84451	-11.12915	JF	1.000	0.000	0.000
480	358.16680	-11.20586	M	0.000	0.833	0.167
481	358.17155	-11.20496	M	0.000	1.000	0.000
482	358.09223	-11.07317	M	0.083	0.750	0.167
485	357.49332	-10.82193	JF	0.583	0.417	0.000
492	358.49303	-12.16549	JF	0.600	0.000	0.400
497	358.38001	-11.92804	JF	0.929	0.071	0.000
500	358.32702	-11.83154	PM	0.000	0.667	0.333
502	358.28778	-11.70974	JF	0.600	0.000	0.400
504	358.35676	-11.73267	JM	0.333	0.333	0.333
505	358.47072	-11.85894	M	0.200	0.800	0.000
507	358.39167	-11.50539	JF	0.500	0.000	0.500
510	358.49953	-11.66317	PM	0.000	0.500	0.500
512	358.29031	-11.34935	JM	0.667	0.333	0.000
516	358.36276	-11.33369	JF	0.583	0.083	0.333
523	358.25229	-11.17124	JF	0.417	0.250	0.333
531	357.71679	-10.46376	JF	0.700	0.300	0.000

Table B.1 continued from previous page

532	358.13805	-10.61129	JF	0.667	0.000	0.333
535	358.34444	-10.54271	M	0.200	0.800	0.000
538	358.33703	-10.44327	JF	1.000	0.000	0.000
543	358.51219	-10.46514	M	0.167	0.500	0.333
545	358.50879	-10.43303	M	0.167	0.833	0.000
547	358.51908	-10.43059	JF	0.900	0.100	0.000
549	358.55655	-10.46340	JF	0.667	0.167	0.167
550	356.93242	-10.10521	M	0.000	1.000	0.000
557	358.04979	-9.86956	JF	0.600	0.400	0.000
560	357.18881	-9.23955	JF	0.500	0.167	0.333
561	357.08640	-9.07355	JM	0.643	0.214	0.143
564	357.99824	-9.54075	M	0.083	0.917	0.000
565	357.58651	-8.88589	M	0.000	1.000	0.000
566	357.76805	-9.21759	PM	0.000	0.667	0.333
568	358.54689	-10.40815	M	0.000	0.500	0.500
569	358.48798	-10.37459	M	0.083	0.917	0.000
571	358.52008	-10.32499	JF	0.571	0.000	0.429
572	358.55698	-10.39026	M	0.000	1.000	0.000
573	358.55625	-10.38574	M	0.100	0.900	0.000
575	358.48920	-10.25349	M	0.000	1.000	0.000
583	358.49678	-9.19279	M	0.000	0.600	0.400
588	357.59436	-8.64785	JF	0.786	0.071	0.143
589	357.82511	-8.62681	JF	0.600	0.000	0.400
592	358.57147	-10.41568	M	0.000	0.800	0.200
593	358.56183	-10.41358	M	0.250	0.750	0.000
595	358.60823	-10.41115	M	0.000	0.667	0.333
597	358.55711	-10.37252	M	0.000	0.500	0.500
612	358.89801	-9.76580	M	0.333	0.667	0.000
617	359.13513	-9.75631	JF	0.714	0.143	0.143
618	359.93535	-10.12369	JF	0.800	0.000	0.200
626	358.95113	-9.38944	M	0.100	0.900	0.000
629	358.74878	-9.24803	M	0.000	0.833	0.167
630	358.74820	-9.24562	M	0.000	1.000	0.000
636	358.69484	-9.01189	JF	0.333	0.333	0.333

Table B.1 continued from previous page

637	358.80014	-9.06530	JF	0.500	0.000	0.500
641	359.84268	-9.61400	JF	0.643	0.357	0.000
642	359.32888	-9.16648	PM	0.000	0.500	0.500
645	359.99299	-9.10078	PM	0.167	0.833	0.000
646	359.05929	-8.86970	PM	0.200	0.600	0.200
647	358.70143	-8.62838	JM	0.429	0.429	0.143
648	358.72309	-8.61664	M	0.429	0.571	0.000
651	359.33505	-8.65009	JF	0.700	0.100	0.200
652	359.64157	-8.69734	JF	0.667	0.000	0.333
653	359.67563	-8.64929	JM	0.500	0.333	0.167
662	358.98633	-12.10047	JF	0.500	0.167	0.333
663	358.95031	-12.04422	JF	0.786	0.214	0.000
664	358.57496	-11.58301	JF	0.667	0.000	0.333
666	358.76102	-11.70125	JM	0.357	0.357	0.286
668	358.68797	-11.59825	JF	0.429	0.143	0.429
669	358.68007	-11.57605	JF	0.750	0.250	0.000
677	359.51031	-12.22012	JM	0.400	0.600	0.000
684	359.33770	-12.02748	JF	0.600	0.000	0.400
690	359.50302	-11.91512	JF	0.714	0.143	0.143
708	359.79357	-11.53664	JF	0.500	0.214	0.286
712	359.95754	-11.58909	JF	0.900	0.100	0.000
713	359.95392	-11.53194	JF	0.833	0.167	0.000
715	358.59328	-11.38965	PM	0.250	0.583	0.167
722	358.62056	-11.30949	JM	0.333	0.333	0.333
724	358.57568	-11.25034	JF	0.500	0.333	0.167
728	358.75295	-11.40814	JF	0.929	0.071	0.000
729	358.81247	-11.47520	JF	0.500	0.214	0.286
732	358.86595	-11.44845	JF	0.500	0.500	0.000
733	358.84499	-11.39690	JF	0.667	0.000	0.333
753	359.14656	-11.11274	JF	0.429	0.143	0.429
754	359.42591	-11.19957	JF	0.333	0.333	0.333
755	359.57791	-11.44225	JF	0.667	0.000	0.333
758	359.86357	-11.06018	M	0.000	0.857	0.143
764	359.95285	-10.82104	PM	0.100	0.700	0.200

Table B.1 continued from previous page

767	358.58176	-10.43162	M	0.000	0.571	0.429
772	359.26739	-10.42607	JF	0.857	0.000	0.143
774	359.47995	-10.42052	JM	0.500	0.167	0.333
776	359.98098	-10.45068	M	0.167	0.833	0.000
784	360.19973	-11.70127	JM	0.333	0.333	0.333
785	360.34671	-11.72702	M	0.000	1.000	0.000
786	360.34486	-11.72640	M	0.000	1.000	0.000
788	360.22373	-11.67400	JF	0.667	0.000	0.333
801	360.29870	-11.28749	JM	0.500	0.500	0.000
804	360.20985	-11.26370	M	0.000	0.667	0.333
805	360.14277	-11.09888	M	0.167	0.833	0.000
808	360.30438	-11.10356	JM	0.500	0.500	0.000
810	360.21190	-10.99979	JF	0.833	0.167	0.000
813	360.19632	-10.80247	JF	0.667	0.000	0.333
814	360.21701	-10.58690	JF	1.000	0.000	0.000
822	360.27655	-10.40025	JM	0.500	0.167	0.333
824	360.08211	-9.69515	JF	1.000	0.000	0.000
826	360.08038	-9.63207	JF	0.667	0.000	0.333
827	360.18443	-9.56484	M	0.000	0.667	0.333
829	360.21754	-9.53093	JF	0.667	0.000	0.333
842	360.18664	-10.40580	JF	0.833	0.167	0.000
843	360.32517	-10.42615	JF	1.000	0.000	0.000

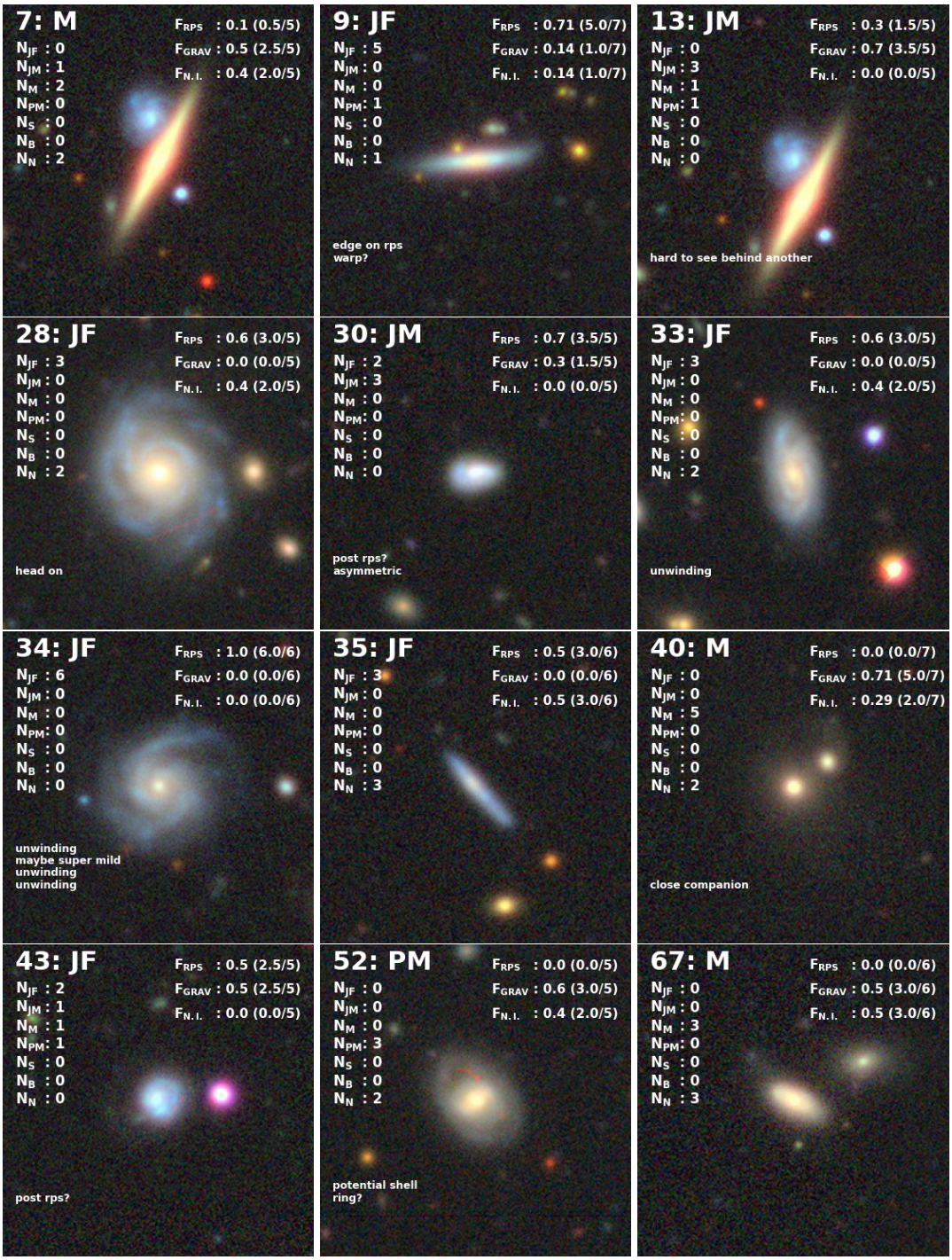

Figure B.1: Mosaic of LS images for all the interacting galaxies found. The labels are as in Figure 4.2.

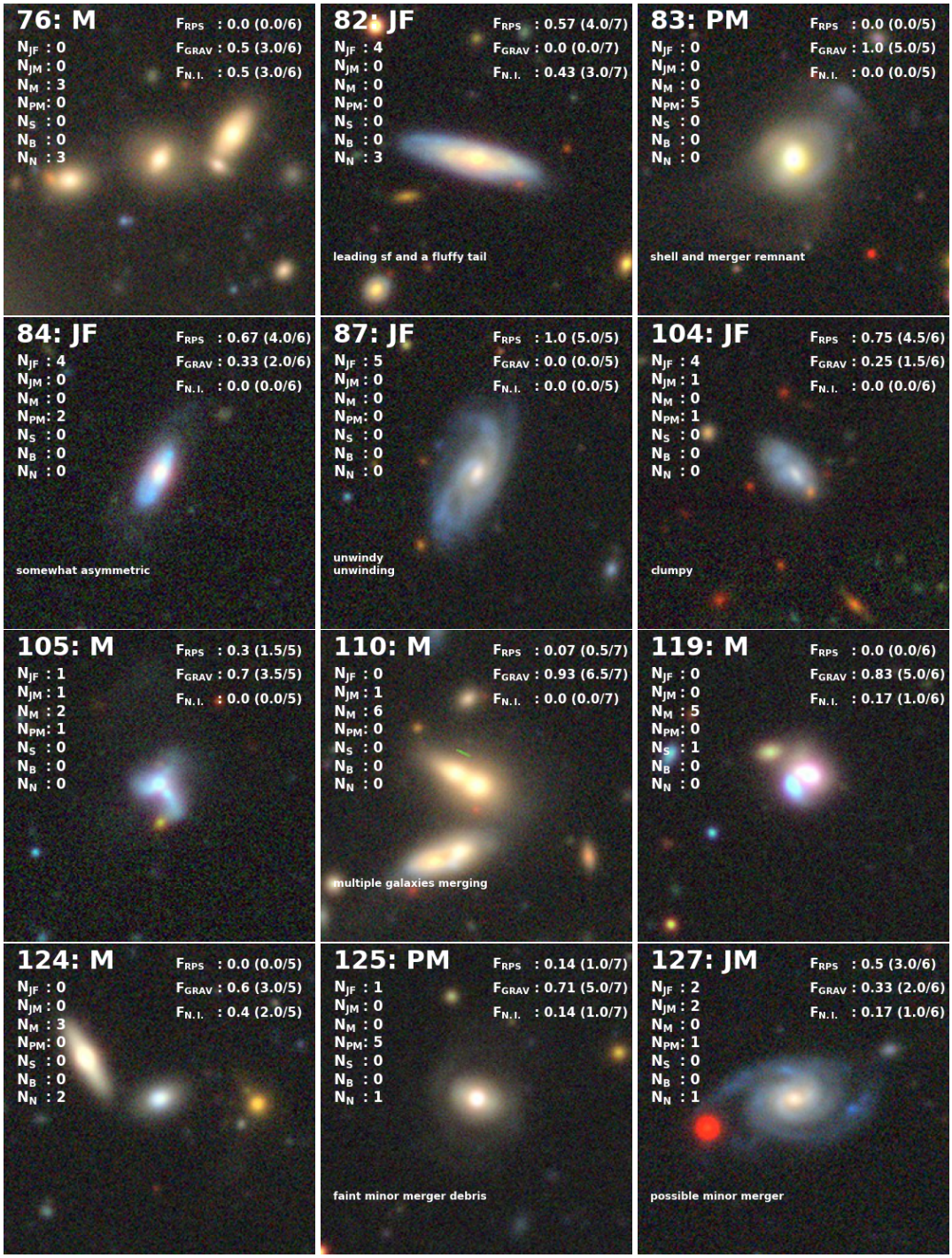

Figure B.1: Continued

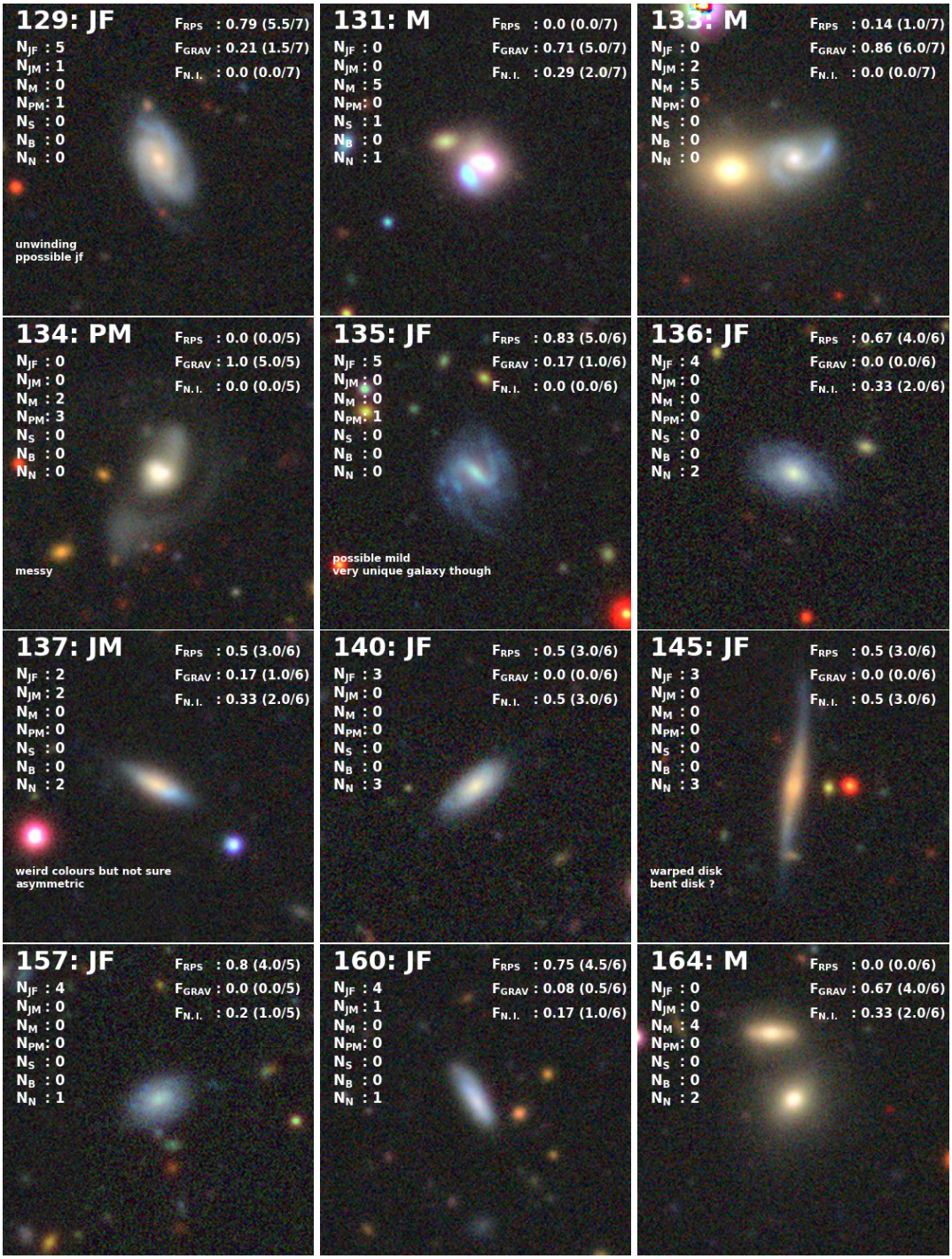

Figure B.1: Continued

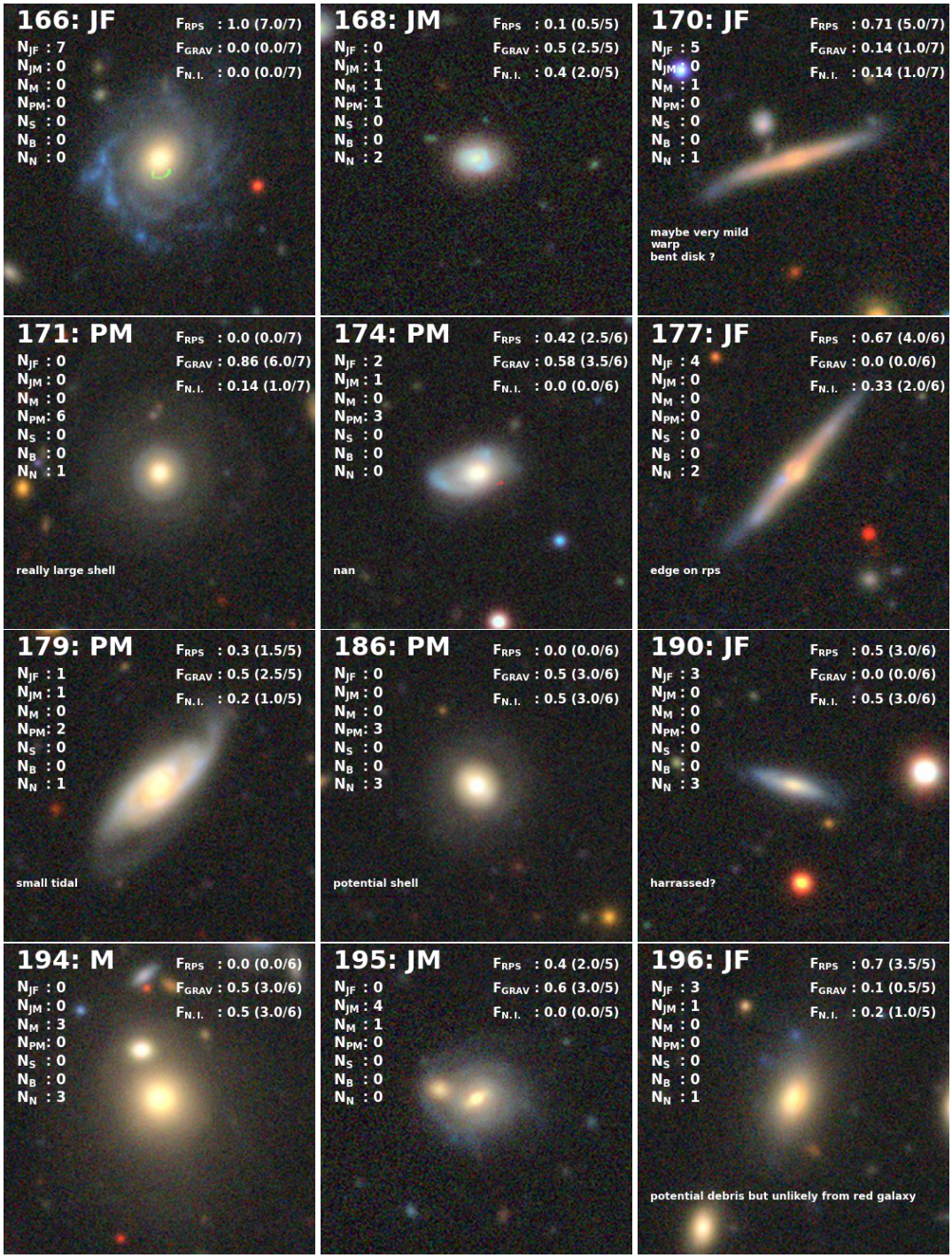

Figure B.1: Continued

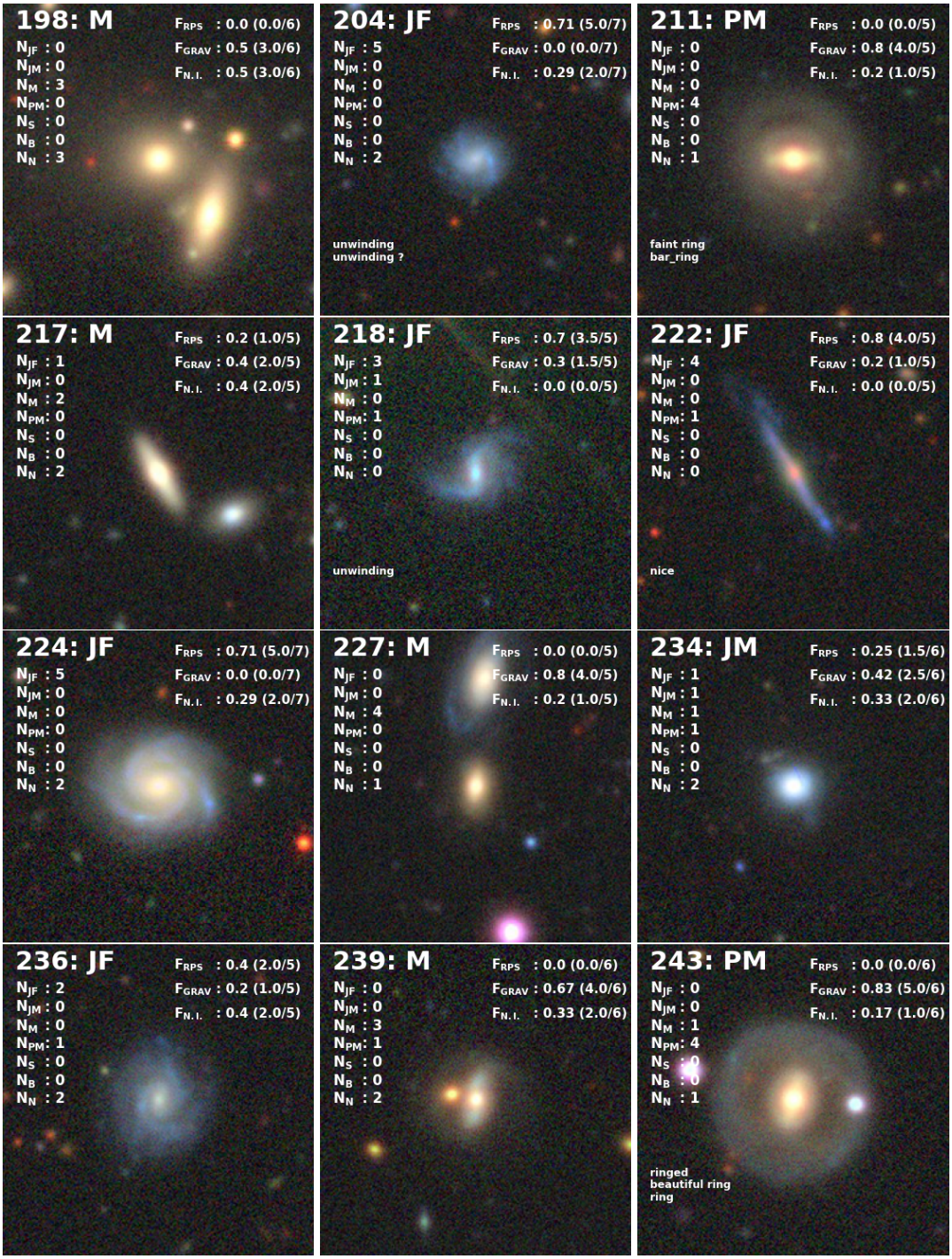

Figure B.1: Continued

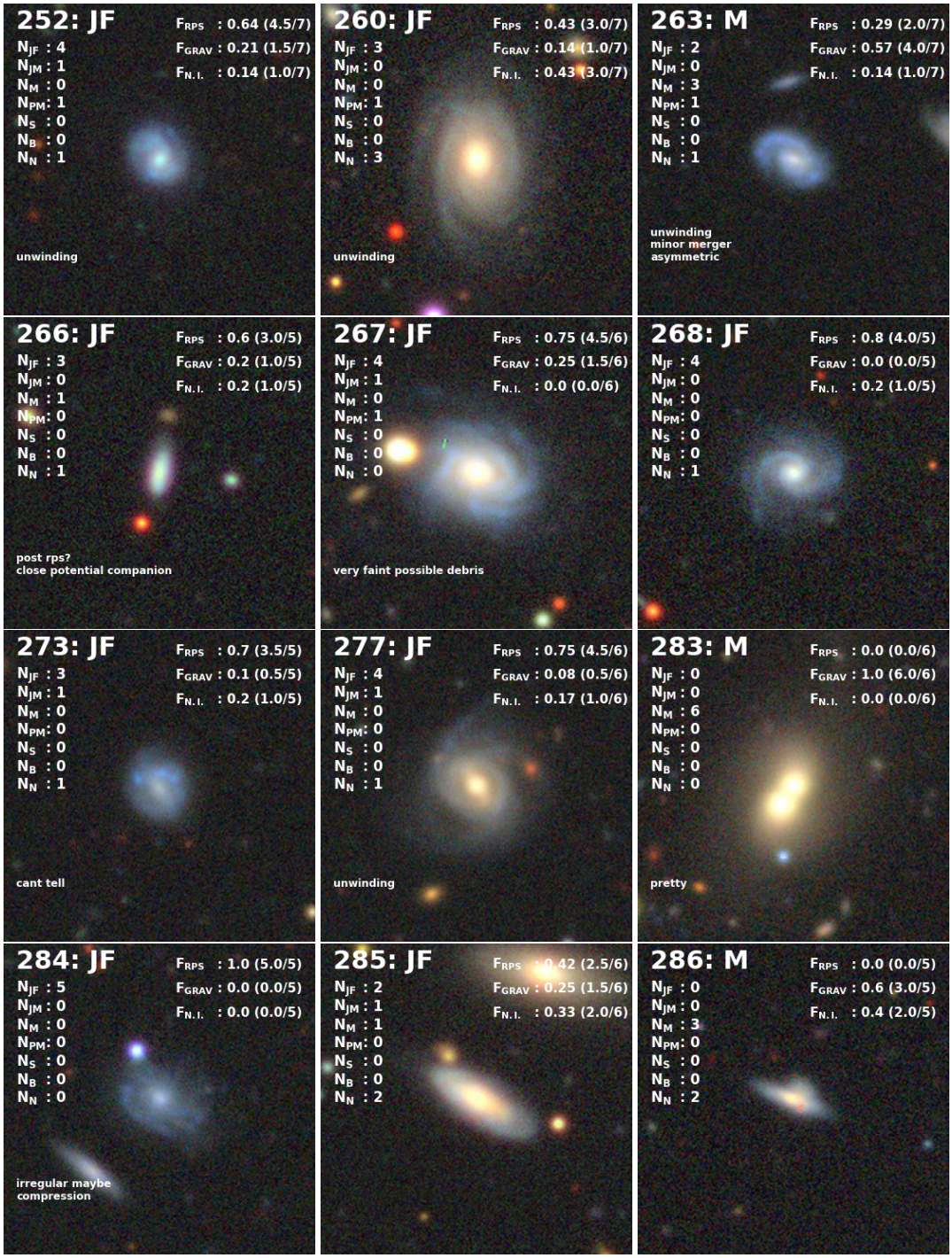

Figure B.1: Continued

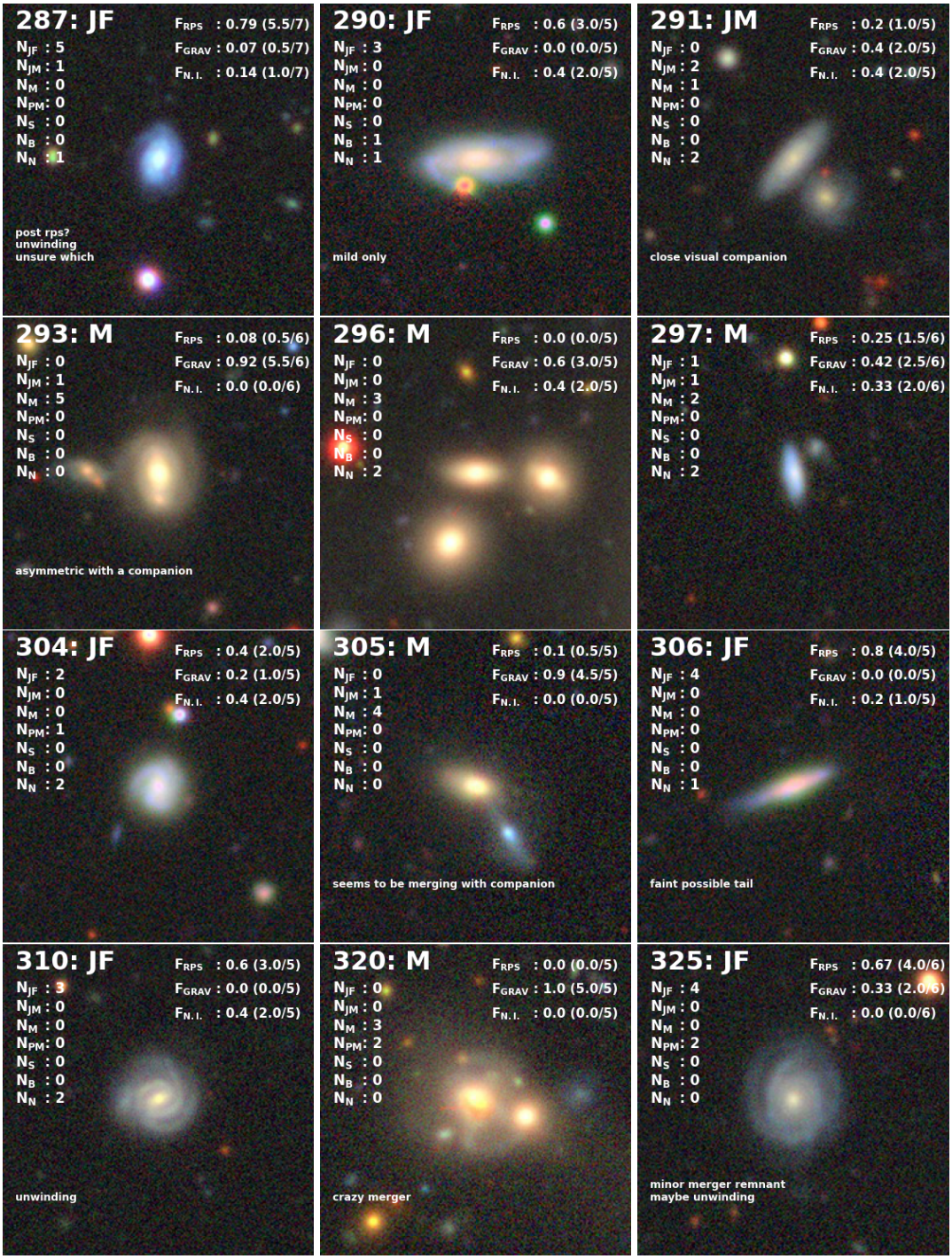

Figure B.1: Continued

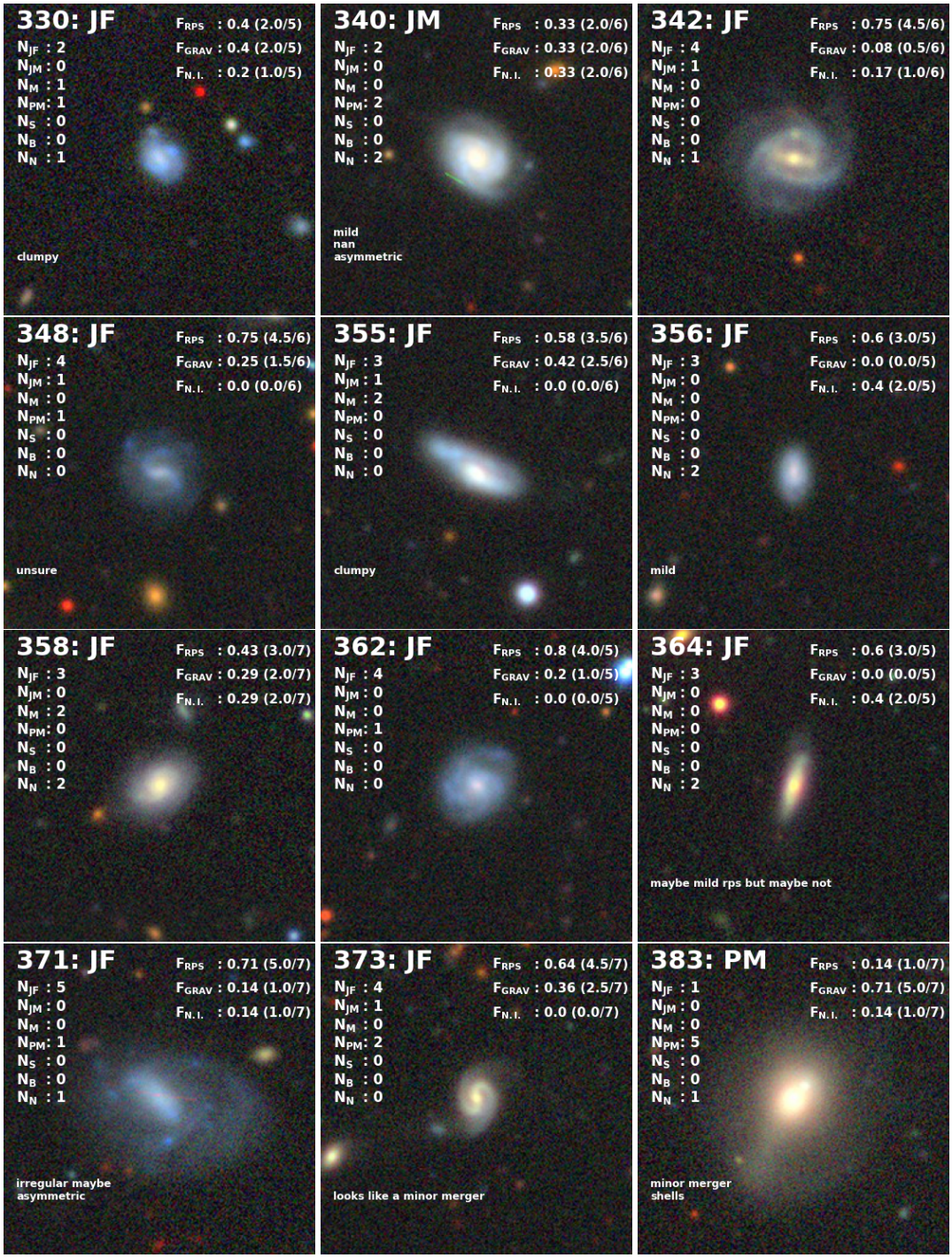

Figure B.1: Continued

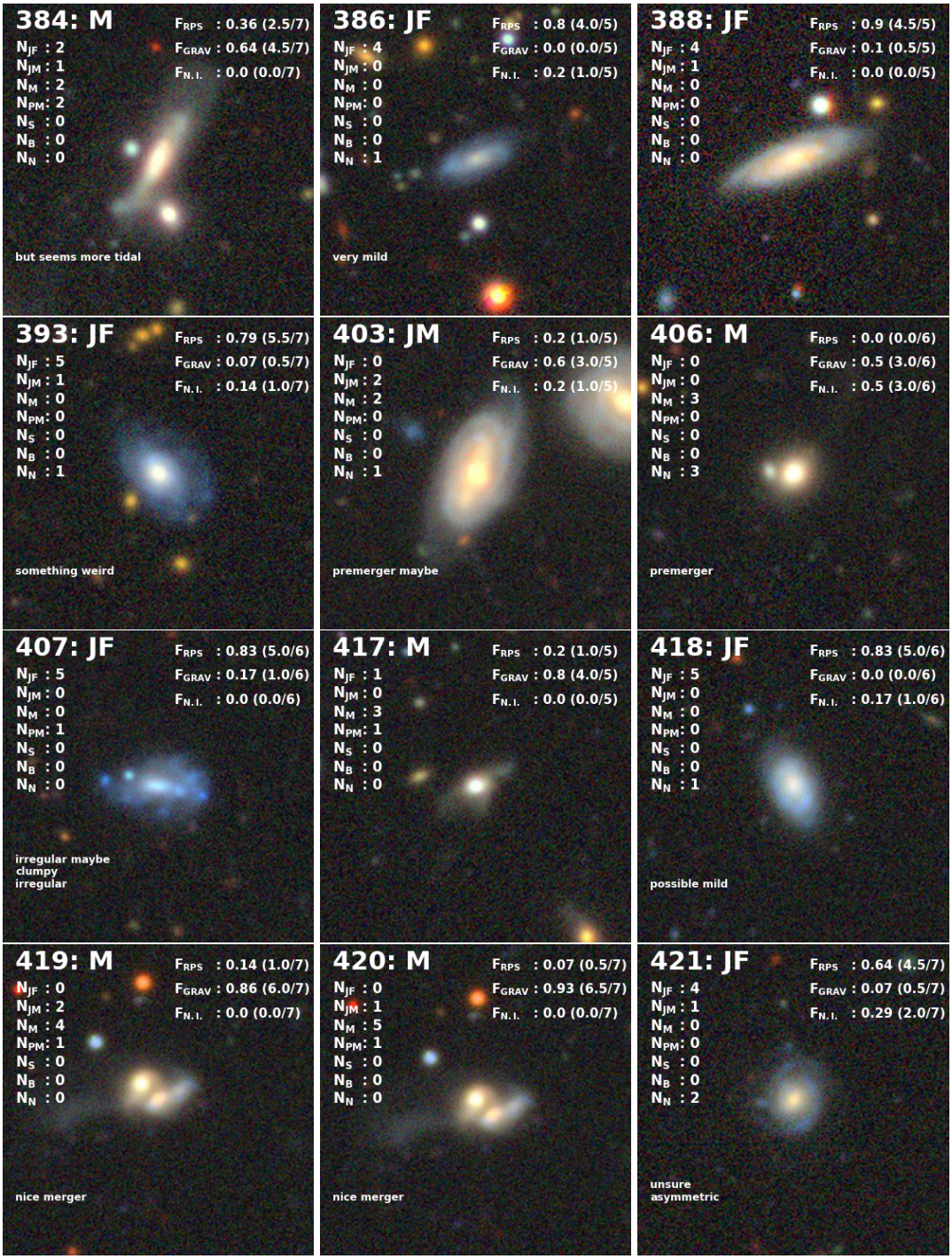

Figure B.1: Continued

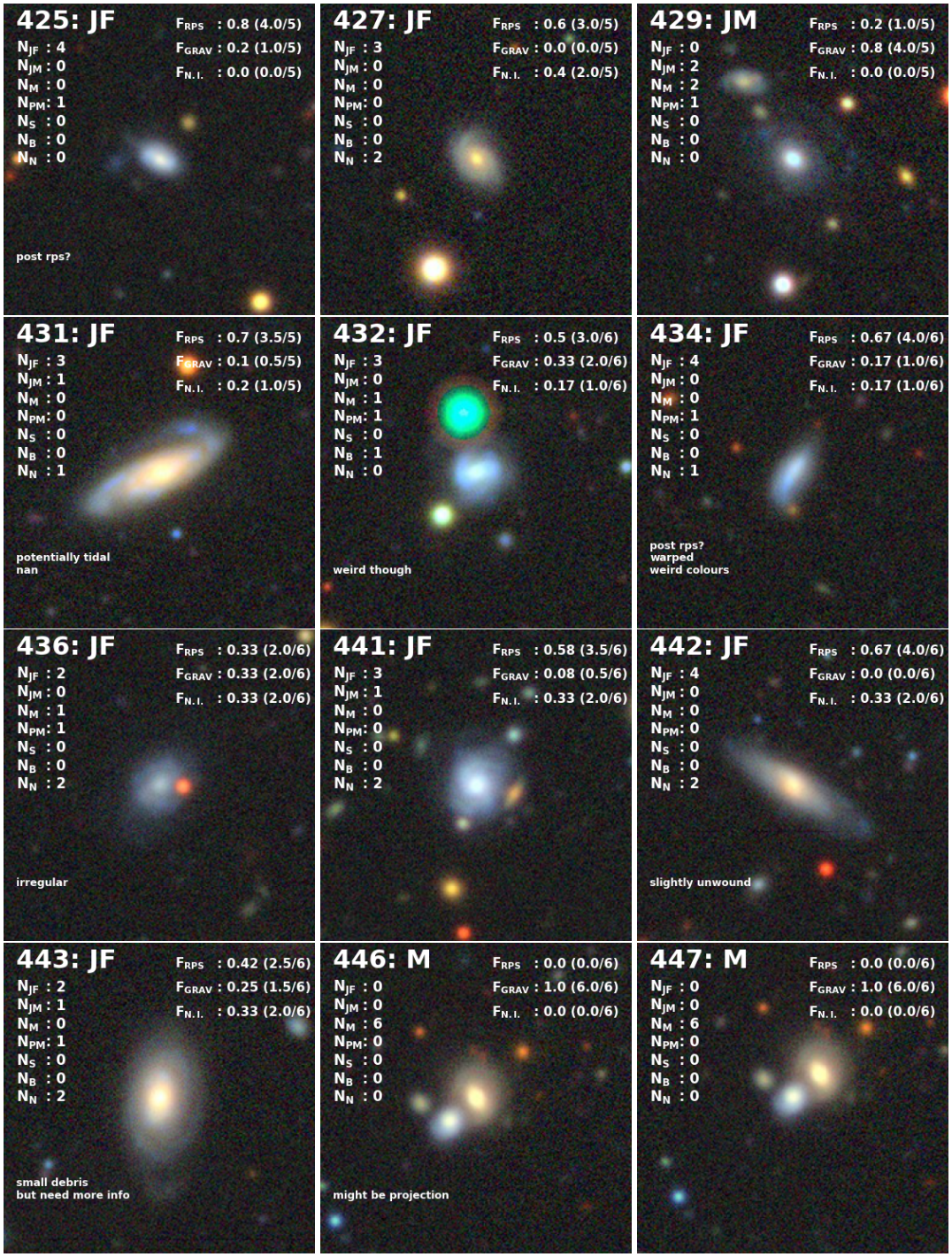

Figure B.1: Continued

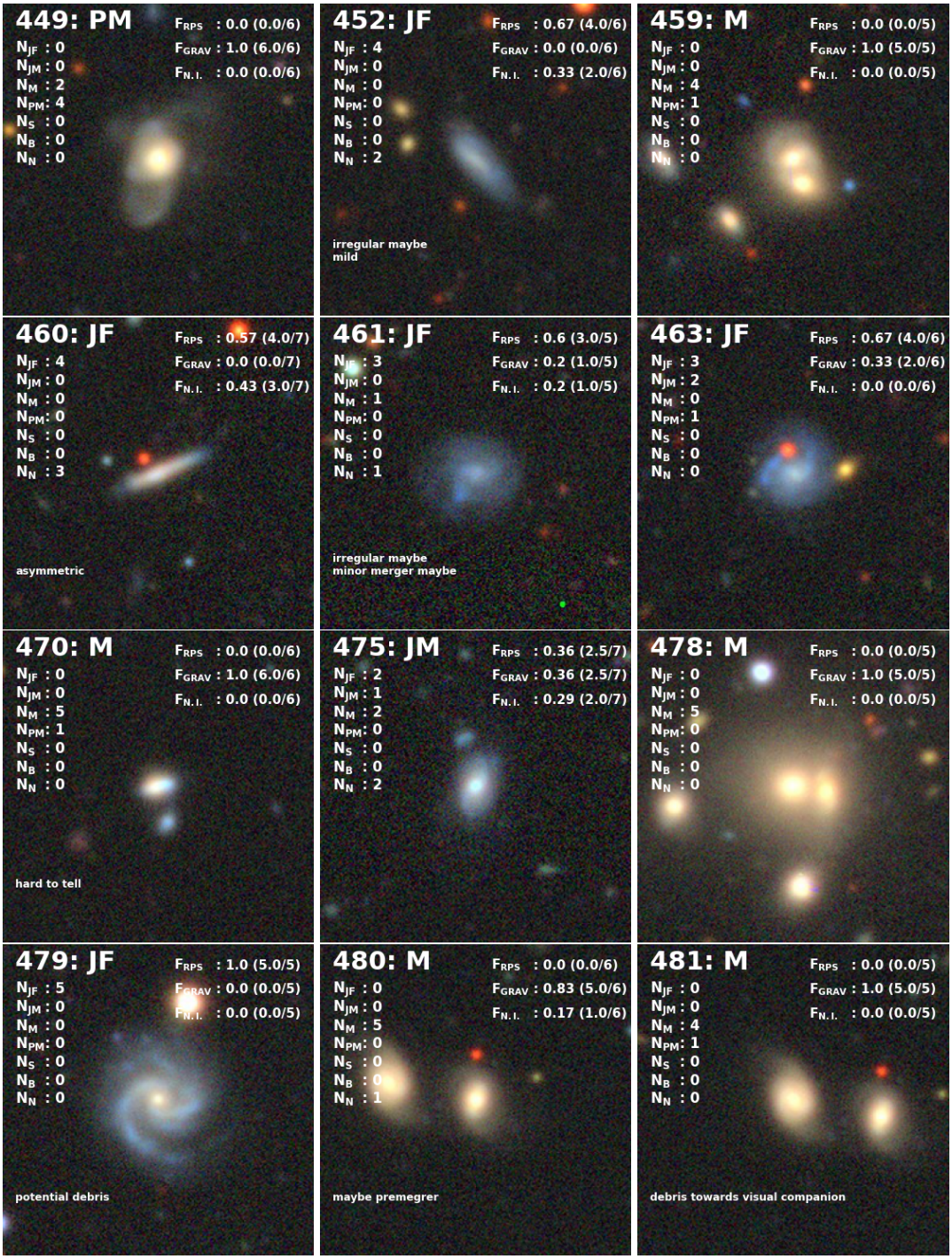

Figure B.1: Continued

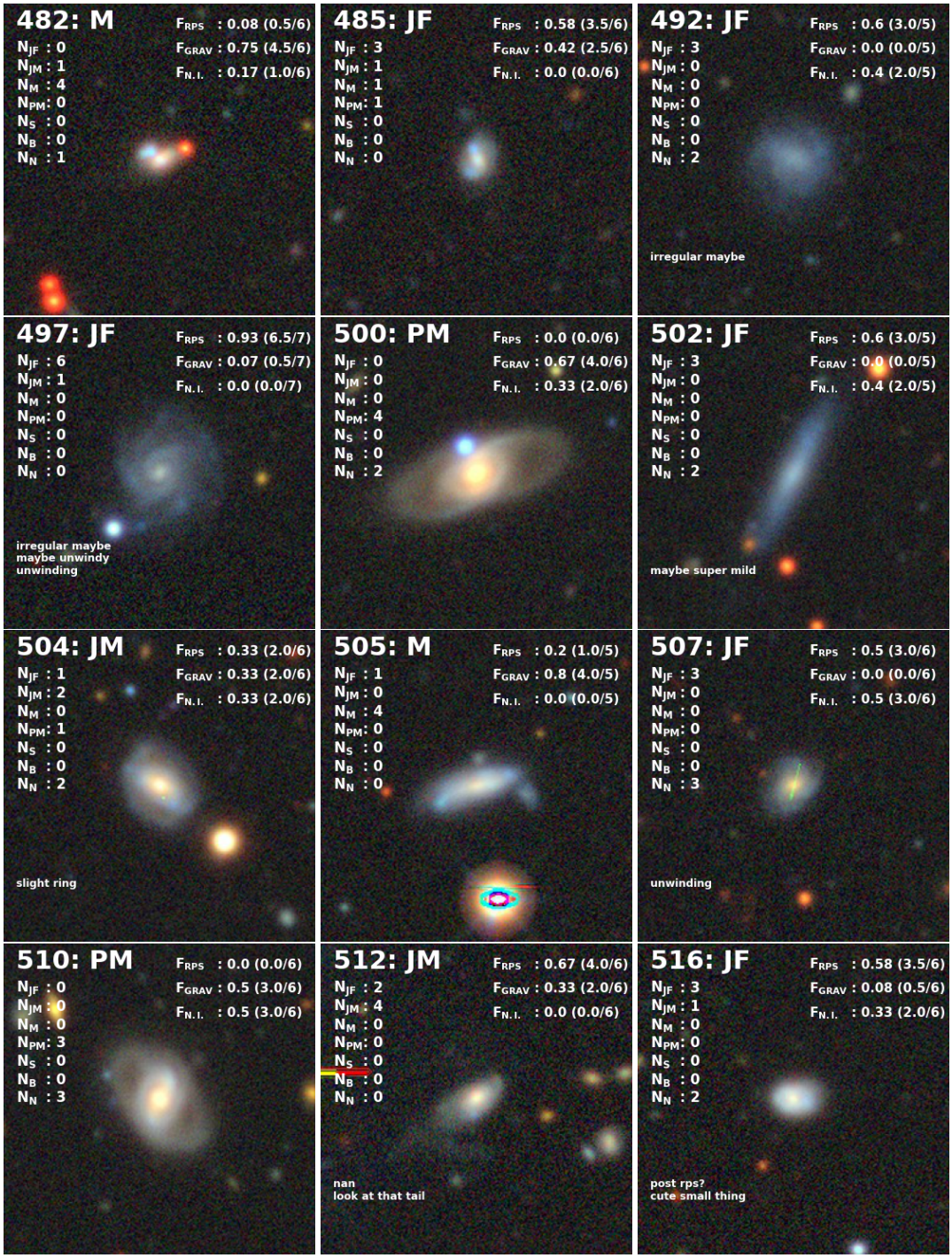

Figure B.1: Continued

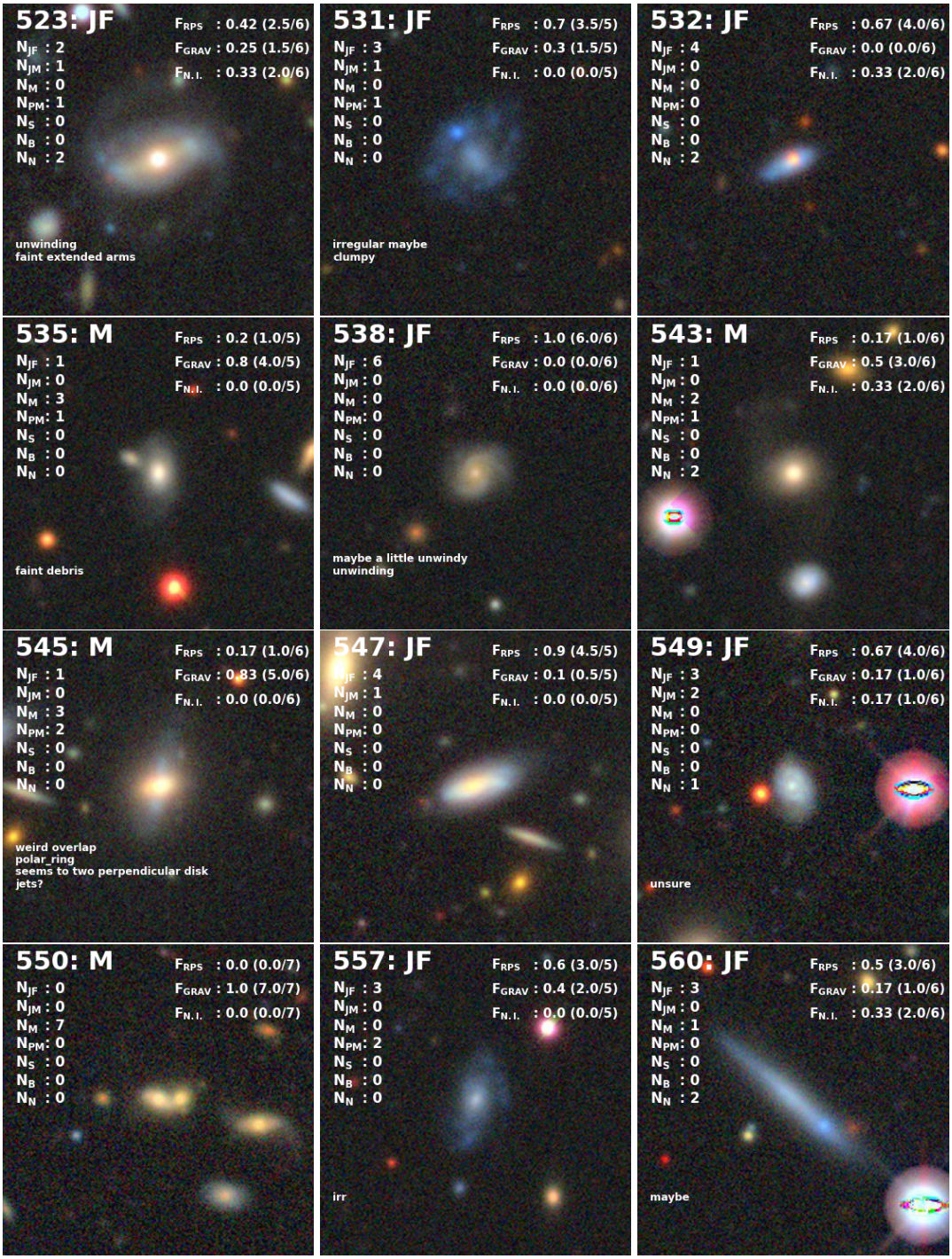

Figure B.1: Continued

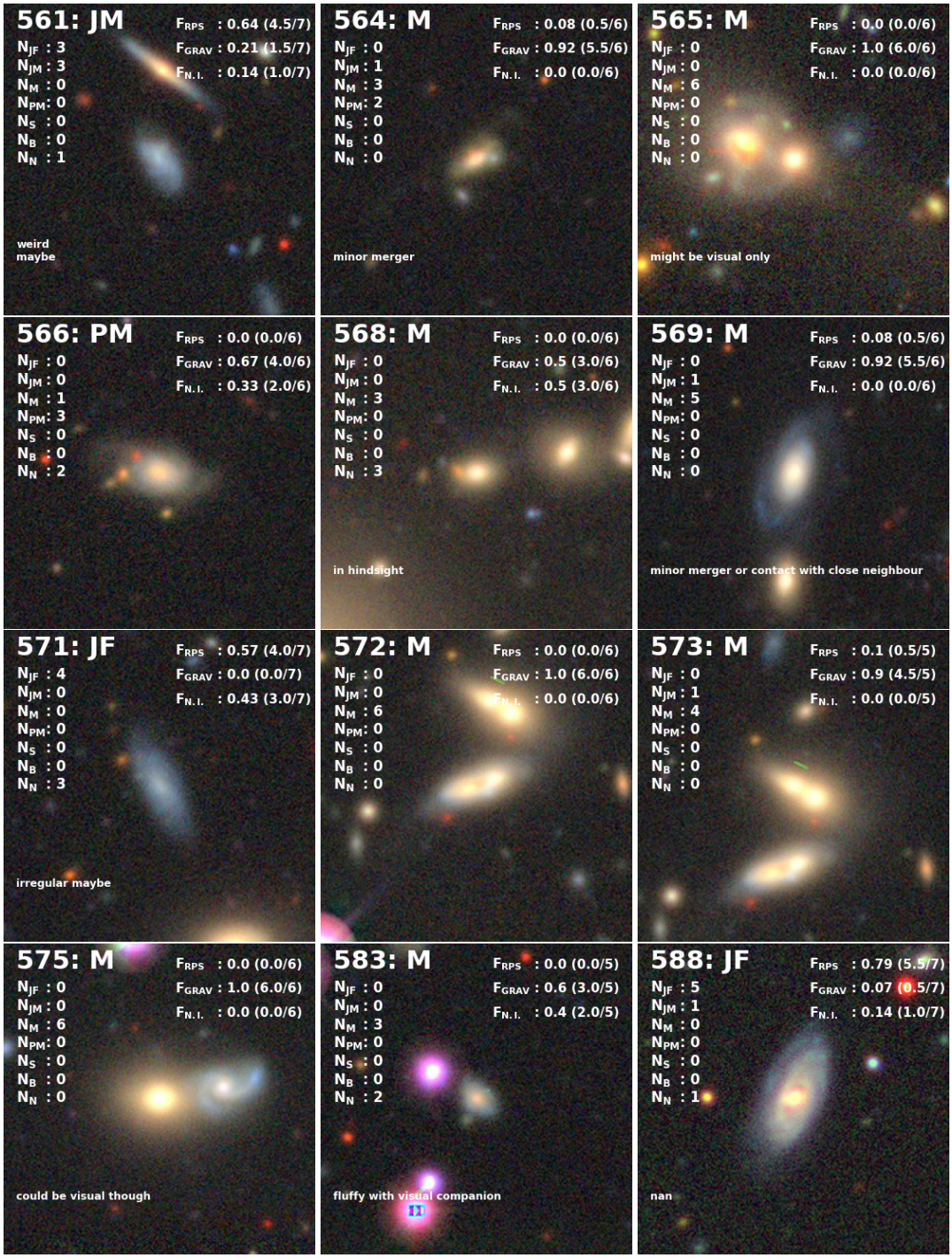

Figure B.1: Continued

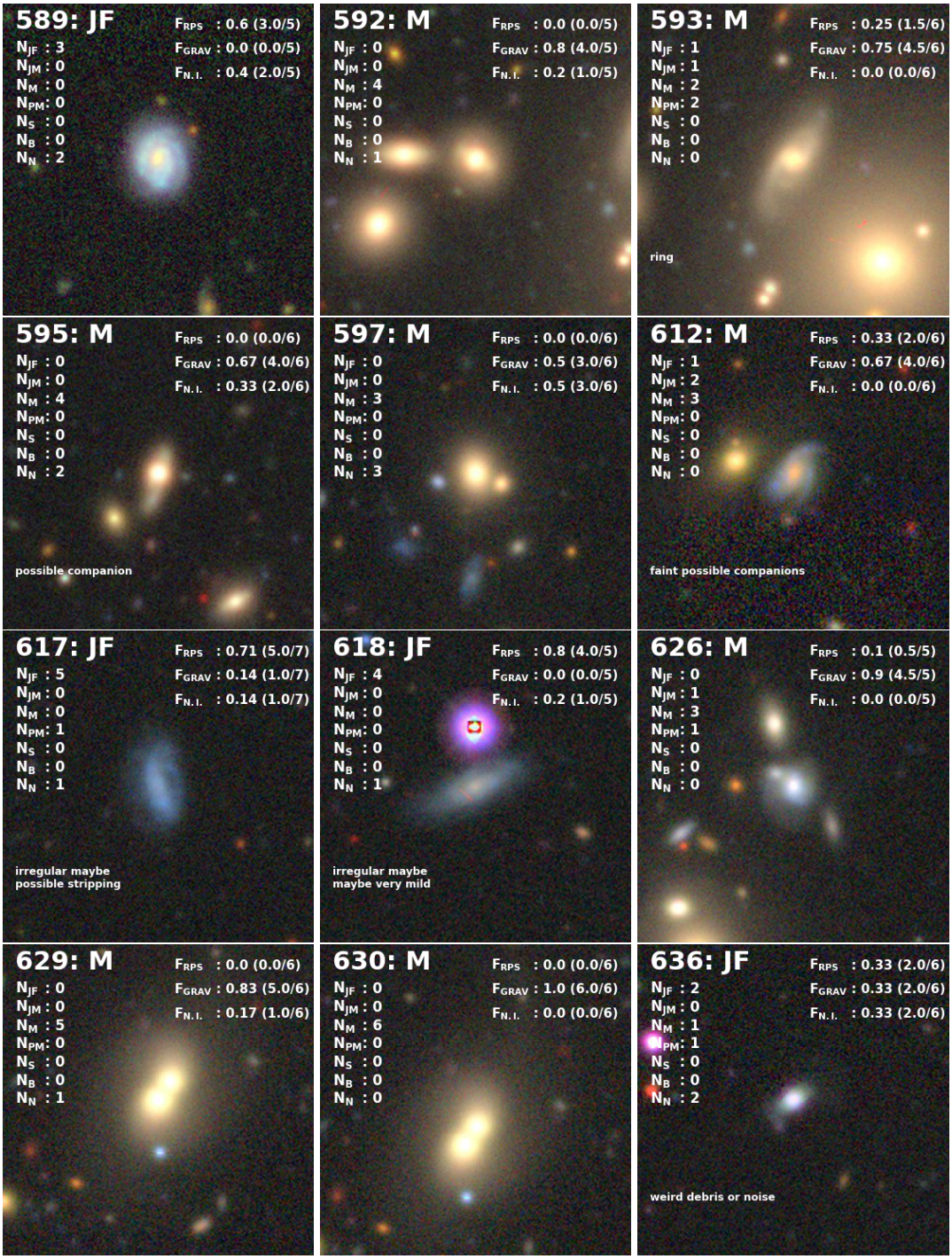

Figure B.1: Continued

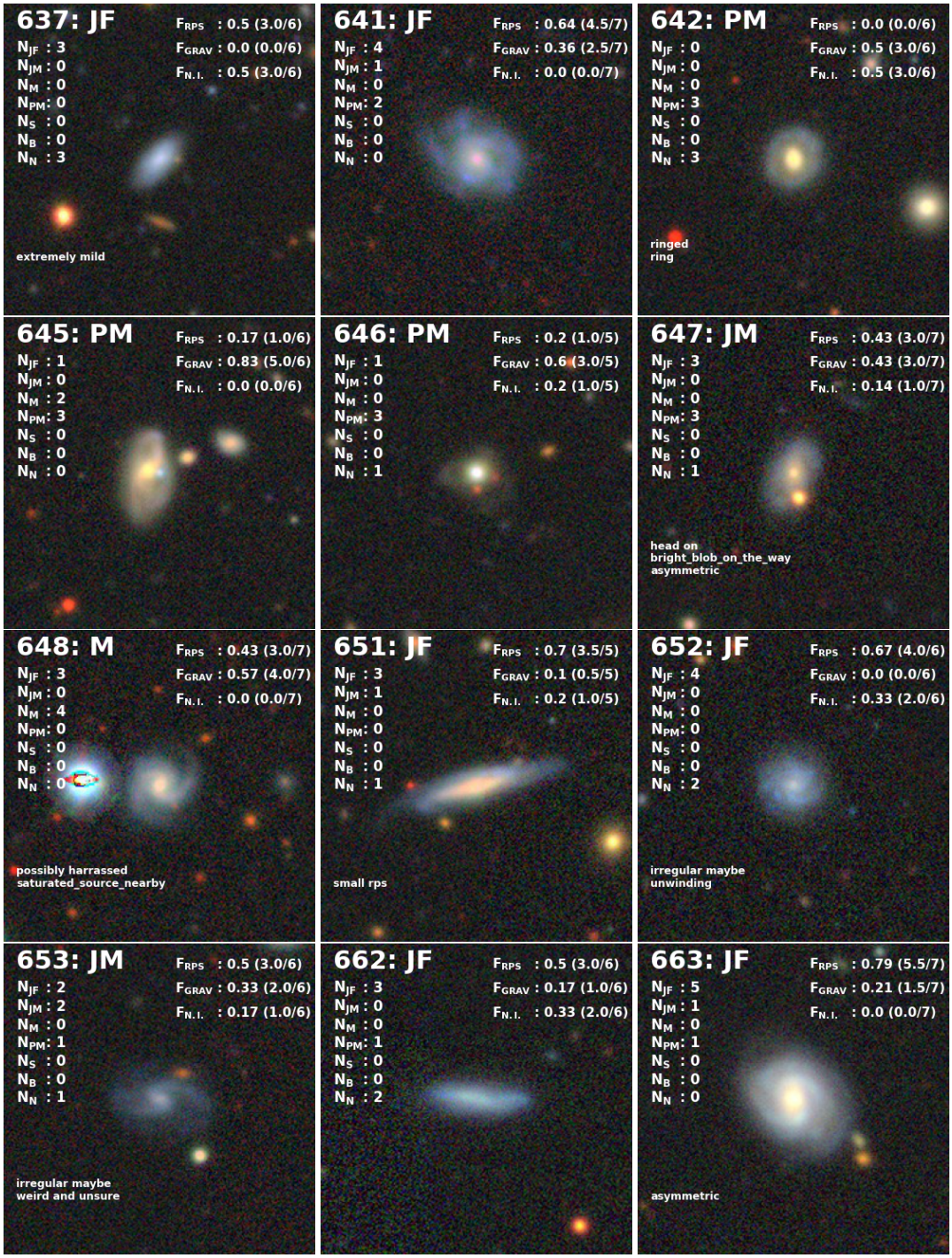

Figure B.1: Continued

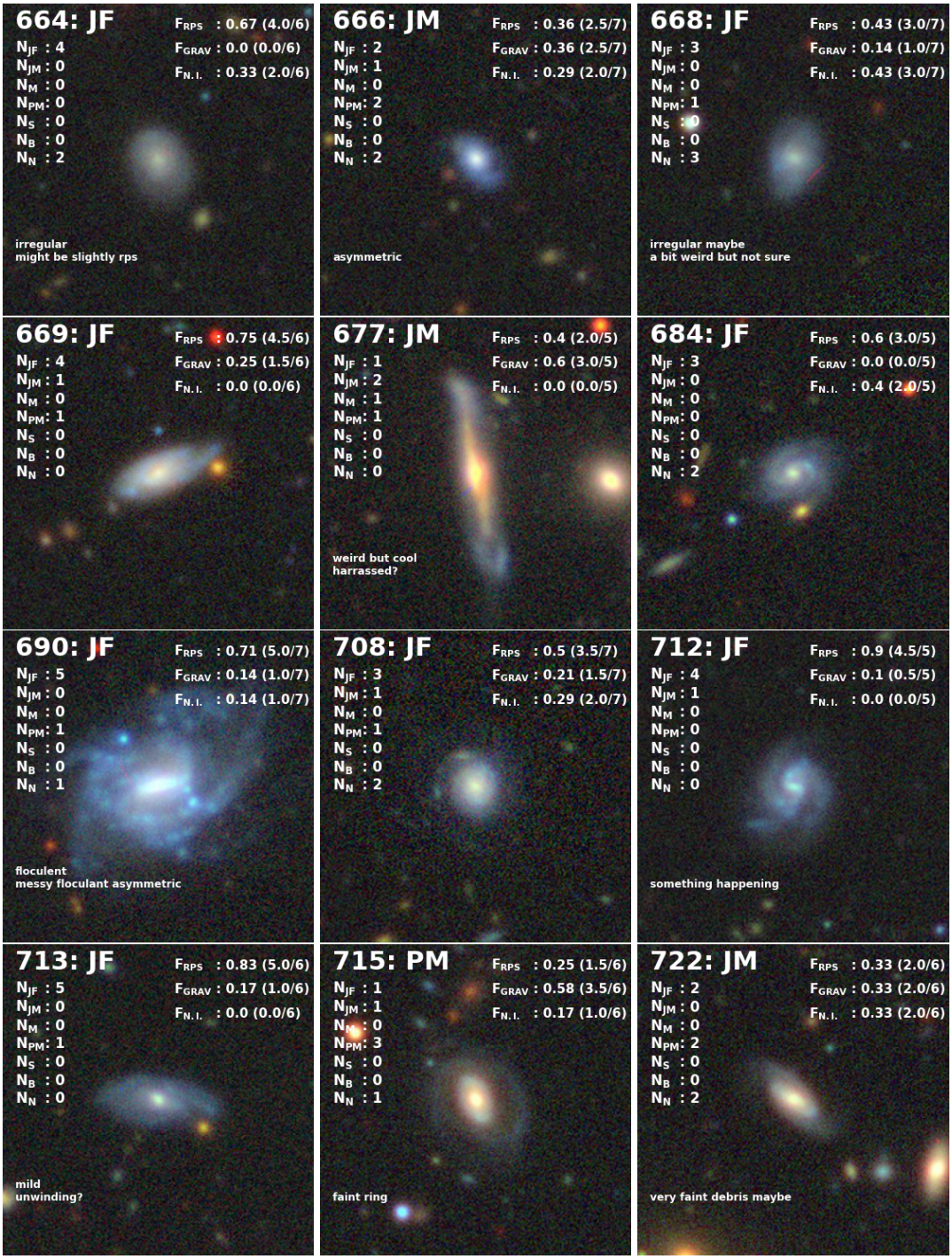

Figure B.1: Continued

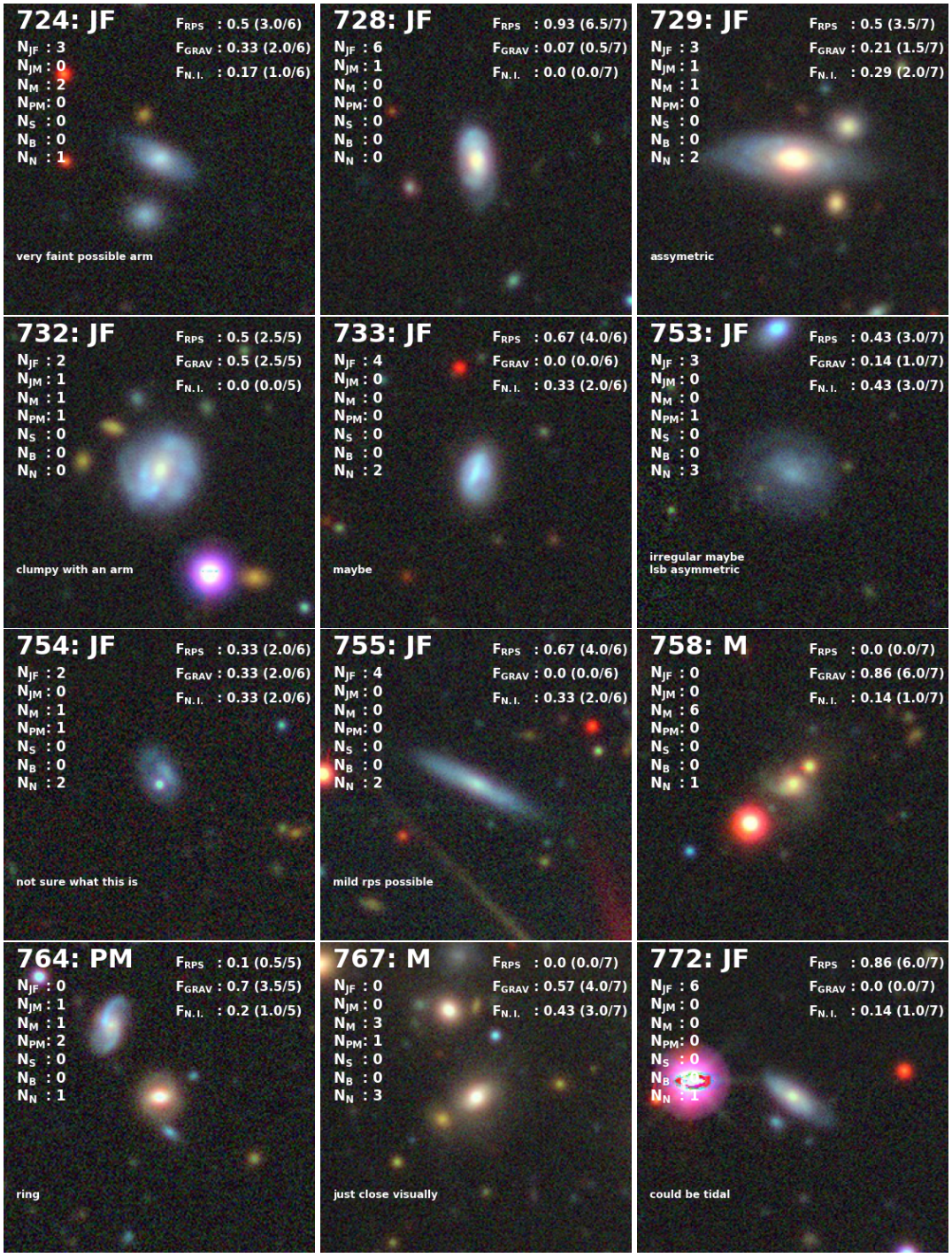

Figure B.1: Continued

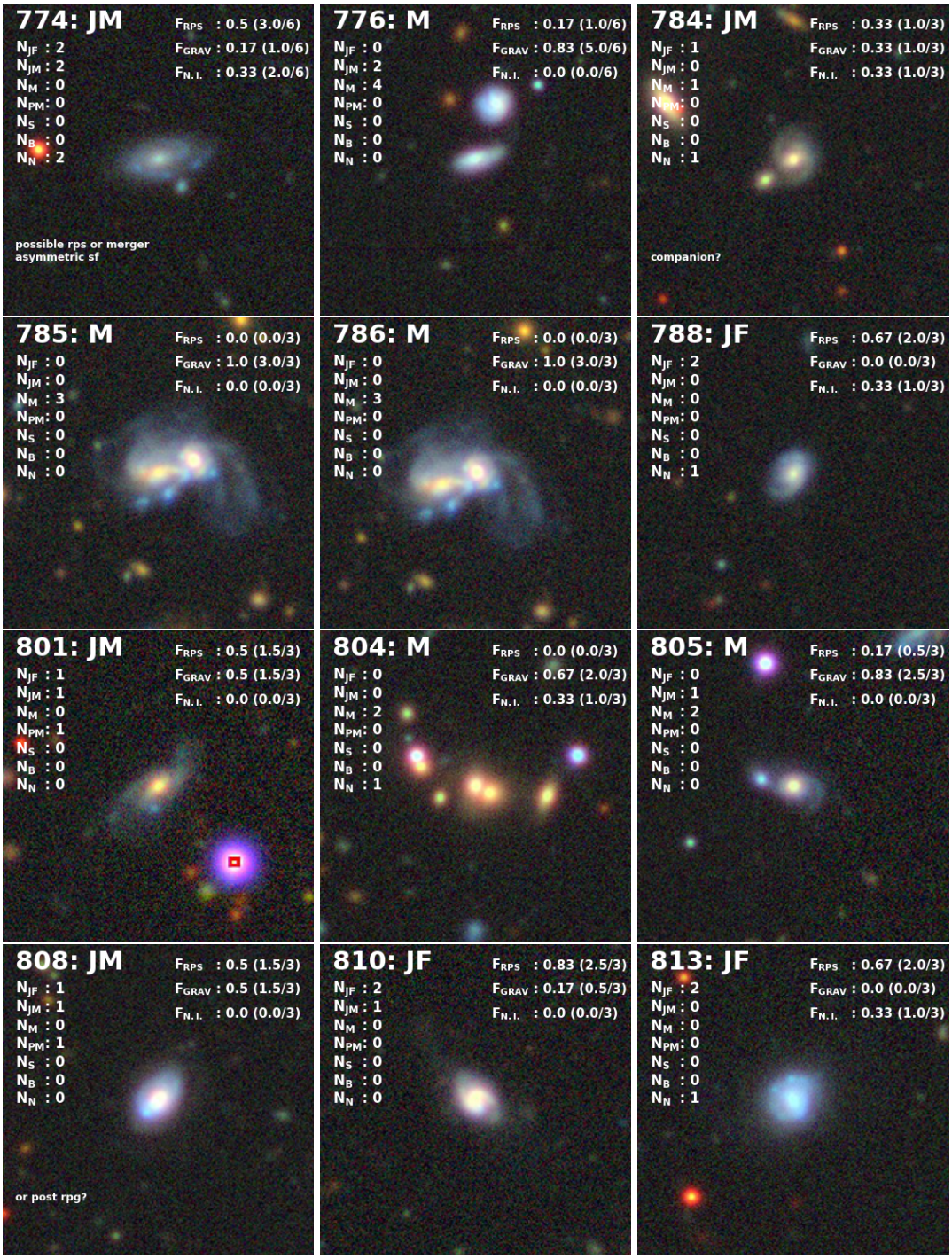

Figure B.1: Continued

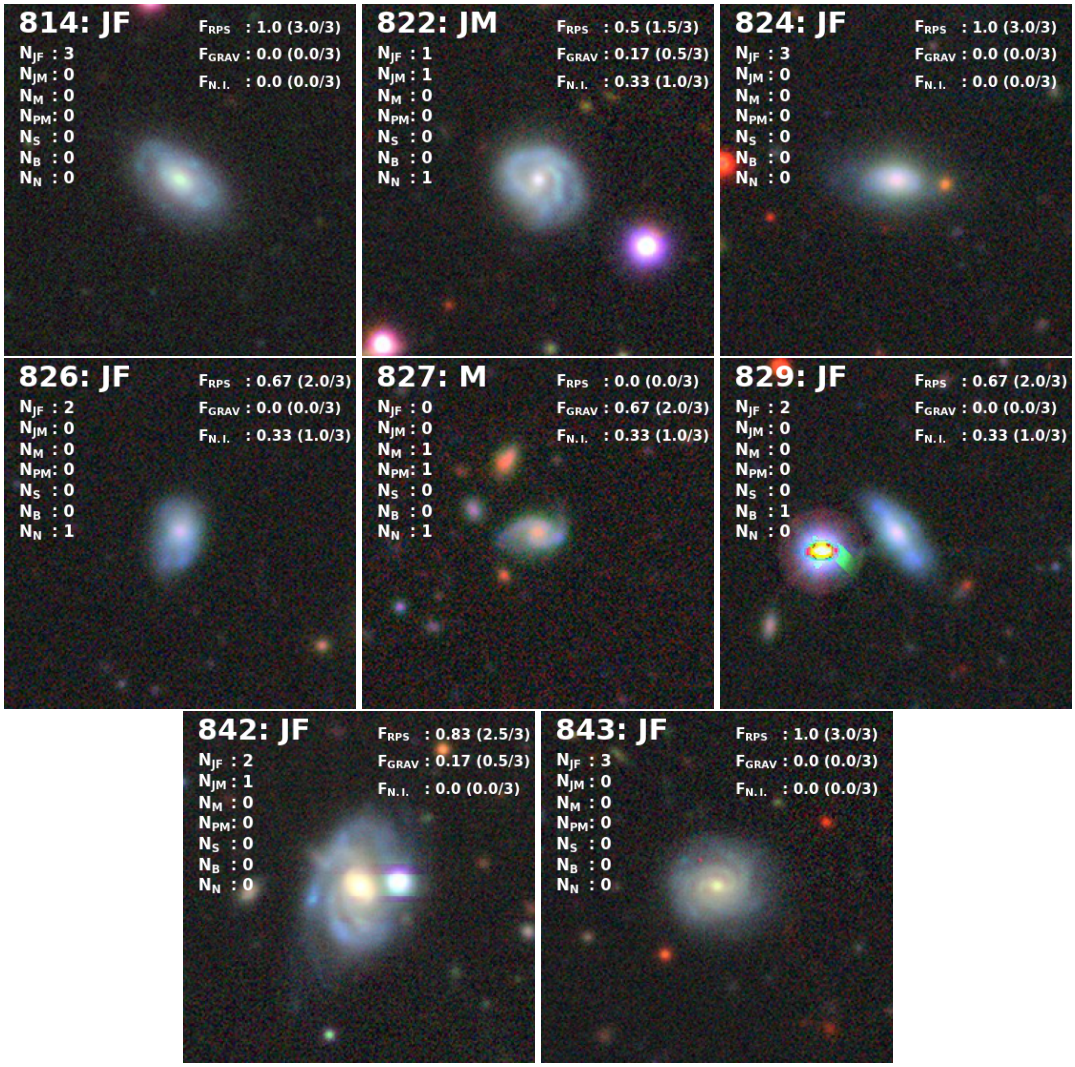

Figure B.1: Continued

Appendix C

Definition of blue and red galaxies

In this appendix, we can visualize the colour-magnitude diagram for the photometric cluster members (Figure C.1). The colour bimodality is defined by the separation between the red sequence and the blue cloud, which is composed of all of these galaxies located 1σ below the red sequence line (black line), yielding a total of 441 blue galaxies. If we restrict the sample to $1 \times R_{200}$, it yields a total of 53 blue galaxies.

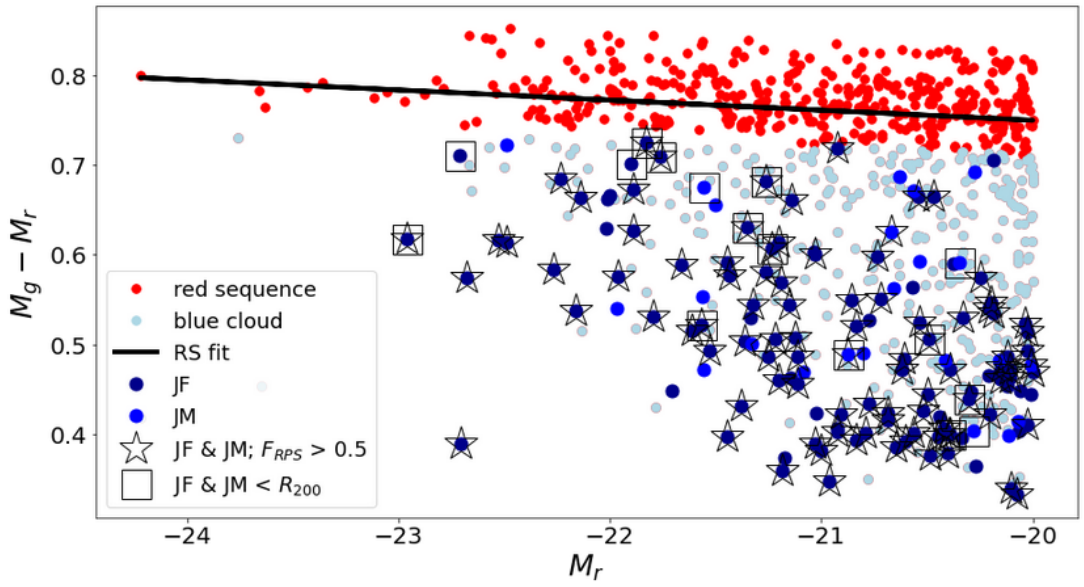

Figure C.1: Color magnitude diagram for the photometric cluster members. The red sequence is shown by the black line. The separation between *red sequence* (red dots) and the *blue cloud* (blue markers) galaxies is defined by the 1σ line below red sequence as in (Vulcani et al., 2022). The *blue cloud* is composed both by galaxies suffering gravitational interaction or non-interacting (light blue dots), galaxies that were classified as JF (dark blue dots), and galaxies that were classified as JM (blue dots). The blue galaxies classified both as JF and JM with vote fraction $F_{\rm RPS} > 0.5$ are plotted as stars and those that are located to ¡ R_{200} are plotted as squares. Our results show that between $\sim 22-32\%$ of the blue members of A2670 are being affected by RPS and if we restrict the sample to $1 \times R_{200}$ (closer to the area explored by Vulcani et al., 2022) the fraction of blue RPS candidates decrease only very mildly ($21-30\%$).

Bibliography

Ahn C. P. et al., 2012, ApJS, 203, 21

Bahé Y. M., McCarthy I. G., Balogh M. L., Font A. S., 2013, MNRAS, 430, 3017

Bellhouse C. et al., 2021, MNRAS, 500, 1285

Bianconi M., Smith G. P., Haines C. P., McGee S. L., Finoguenov A., Egami E., 2018, MNRAS, 473, L79

Binney J., Tremaine S., 1987, Galactic dynamics

Boselli A., Gavazzi G., 2006, PASP, 118, 517

Boselli A. et al., 2014, A&A, 570, A69

Buitinck L. et al., 2013, in ECML PKDD Workshop: Languages for Data Mining and Machine Learning, p. 108

Chilingarian I. V., Melchior A.-L., Zolotukhin I. Y., 2010, MNRAS, 405, 1409

Chilingarian I. V., Zolotukhin I. Y., 2012, MNRAS, 419, 1727

Chung A., van Gorkom J. H., Kenney J. D. P., Crowl H., Vollmer B., 2009, AJ, 138, 1741

Clowe D., Gonzalez A., Markevitch M., 2004, ApJ, 604, 596

Cortese L., Catinella B., Smith R., 2021, , 38, e035

Cortese L., Gavazzi G., Boselli A., Franzetti P., Kennicutt R. C., O'Neil K., Sakai S., 2006, A&A, 453, 847

Dey A. et al., 2019, AJ, 157, 168

Diaferio A., Kauffmann G., Balogh M. L., White S. D. M., Schade D., Ellingson E., 2001, MNRAS, 323, 999

Domainko W. et al., 2006, A&A, 452, 795

Dressler A., 2004, in Diaferio A., ed, IAU Colloq. 195: Outskirts of Galaxy Clusters: Intense Life in the Suburbs, p. 341

Dressler A., Oemler J., Augustus, Poggianti B. M., Gladders M. D., Abramson L., Vulcani B., 2013, ApJ, 770, 62

Dressler A., Shectman S. A., 1988, AJ, 95, 985

Ebeling H., Kalita B. S., 2019, ApJ, 882, 127

Ebeling H., Stephenson L. N., Edge A. C., 2014, ApJ, 781, L40

Einasto M. et al., 2012a, A&A, 542, A36

Einasto M. et al., 2012b, A&A, 540, A123

Farouki R., Shapiro S. L., 1981, ApJ, 243, 32

Fujita Y., 2004, PASJ, 56, 29

Fujita Y., Sarazin C. L., Sivakoff G. R., 2006, PASJ, 58, 131

Fujita Y., Takizawa M., Nagashima M., Enoki M., 1999, PASJ, 51, L1

Fumagalli M., Fossati M., Hau G. K. T., Gavazzi G., Bower R., Sun M., Boselli A., 2014, MNRAS, 445, 4335

Goto T., Yamauchi C., Fujita Y., Okamura S., Sekiguchi M., Smail I., Bernardi M., Gomez P. L., 2003, MNRAS, 346, 601

Gunn J. E., Gott J. R. I., 1972, ApJ, 176, 1

Haines C. P. et al., 2015, ApJ, 806, 101

Hobbs I. S., Willmore A. P., 1997, MNRAS, 289, 685

Hou A., Parker L. C., Harris W. E., 2014, MNRAS, 442, 406

Hou A. et al., 2012, MNRAS, 421, 3594

Hudson D. S., Mittal R., Reiprich T. H., Nulsen P. E. J., Andernach H., Sarazin C. L., 2010, A&A, 513, A37

Hwang H. S., Lee M. G., 2009, MNRAS, 397, 2111

Jaffé Y. L. et al., 2018, MNRAS, 476, 4753

Jaffé Y. L. et al., 2019, MNRAS, 482, 3454

Jaffé Y. L., Poggianti B. M., Verheijen M. A. W., Deshev B. Z., van Gorkom J. H., 2013, MNRAS, 431, 2111

Jaffé Y. L., Smith R., Candlish G. N., Poggianti B. M., Sheen Y.-K., Verheijen M. A. W., 2015, MNRAS, 448, 1715

Jaffé Y. L. et al., 2016, MNRAS, 461, 1202

Kapferer W., Sluka C., Schindler S., Ferrari C., Ziegler B., 2009, A&A, 499, 87

Kass R. E., Raftery A. E., 1995, Journal of the American Statistical Association, 90, 773

Kass R. E., Wasserman L., 1995, Journal of the American Statistical Association, 90, 928

Katayama H., Hayashida K., Takahara F., Fujita Y., 2003, ApJ, 585, 687

Kelkar K. et al., 2020, MNRAS, 496, 442

Kleiner D., Pimbblet K. A., Owers M. S., Jones D. H., Stephenson A. P., 2014, MNRAS, 439, 2755

Kolcu T., Crossett J. P., Bellhouse C., McGee S., 2022, MNRAS, 515, 5877

Kormendy J., Bender R., 1996, ApJ, 464, L119

Kormendy J., Bender R., 2012, ApJS, 198, 2

Larson R. B., Tinsley B. M., Caldwell C. N., 1980, ApJ, 237, 692

López-Gutiérrez M. M. et al., 2022, MNRAS, 517, 1218

Lourenço A. C. C. et al., 2020, MNRAS, 498, 835

Ma C. J., Ebeling H., Marshall P., Schrabback T., 2010, MNRAS, 406, 121

Makino J., Hut P., 1997, ApJ, 481, 83

McGee S. L., Balogh M. L., Bower R. G., Font A. S., McCarthy I. G., 2009, MNRAS, 400, 937

McPartland C., Ebeling H., Roediger E., Blumenthal K., 2016, MNRAS, 455, 2994

Mihos C., Hernquist L., 1994, arXiv e-prints, astro

Monteiro-Oliveira R., Doubrawa L., Machado R. E. G., Lima Neto G. B., Castejon M., Cypriano E. S., 2020, MNRAS, 495, 2007

Monteiro-Oliveira R., Morell D. F., Sampaio V. M., Ribeiro A. L. B., de Carvalho R. R., 2022, MNRAS, 509, 3470

Moore B., Governato F., Quinn T., Stadel J., Lake G., 1998, ApJ, 499, L5

Moore B., Katz N., Lake G., Dressler A., Oemler A., 1996, Nature, 379, 613

Moore B., Lake G., Quinn T., Stadel J., 1999, MNRAS, 304, 465

Navarro J. F., Frenk C. S., White S. D. M., 1996, ApJ, 462, 563

Owers M. S., Couch W. J., Nulsen P. E. J., Randall S. W., 2012, ApJ, 750, L23

Pallero D., Gómez F. A., Padilla N. D., Bahé Y. M., Vega-Martínez C. A., Torres-Flores S., 2022, MNRAS, 511, 3210

Pallero D., Gómez F. A., Padilla N. D., Torres-Flores S., Demarco R., Cerulo P., Olave-Rojas D., 2019, MNRAS, 488, 847

Pedregosa F. et al., 2011, Journal of Machine Learning Research, 12, 2825

Peng Y., others , 2010, ApJ, 721, 193

Poggianti B. M. et al., 2016, AJ, 151, 78

Poggianti B. M. et al., 2017, ApJ, 844, 48

Raouf M., Smith R., Khosroshahi H. G., Dariush A. A., Driver S., Ko J., Hwang H. S., 2019, ApJ, 887, 264

Rawle T. D. et al., 2014, MNRAS, 442, 196

Roberts I. D., Parker L. C., 2020, MNRAS, 495, 554

Roberts I. D., van Weeren R. J., McGee S. L., Botteon A., Ignesti A., Rottgering H. J. A., 2021, A&A, 652, A153

Roman-Oliveira F. V., Chies-Santos A. L., Rodríguez del Pino B., Aragón-Salamanca A., Gray M. E., Bamford S. P., 2019, MNRAS, 484, 892

Ruggiero R., Machado R. E. G., Roman-Oliveira F. V., Chies-Santos A. L., Lima Neto G. B., Doubrawa L., Rodríguez del Pino B., 2019, MNRAS, 484, 906

Sanderson A. J. R., Edge A. C., Smith G. P., 2009, MNRAS, 398, 1698

Scrucca L., Fop M., Murphy T. B., Raftery A. E., 2016, The R Journal, 8, 289

Sheen Y.-K. et al., 2017, ApJ, 840, L7

Sheen Y.-K., Yi S. K., Ree C. H., Lee J., 2012, ApJS, 202, 8

Sifón C., Hoekstra H., Cacciato M., Viola M., Köhlinger F., van der Burg R. F. J., Sand D. J., Graham M. L., 2015, A&A, 575, A48

Smith R., Davies J. I., Nelson A. H., 2010, MNRAS, 405, 1723

Spitzer J., Lyman, Baade W., 1951, ApJ, 113, 413

Stroe A., Oosterloo T., Röttgering H. J. A., Sobral D., van Weeren R., Dawson W., 2015, MNRAS, 452, 2731

Stroe A., Sobral D., Röttgering H. J. A., van Weeren R. J., 2014, MNRAS, 438, 1377

Vijayaraghavan R., Ricker P. M., 2013, MNRAS, 435, 2713

Vulcani B., 2021, in Extragalactic Spectroscopic Surveys: Past, Present and Future of Galaxy Evolution (GALSPEC2021), p. 34

Vulcani B. et al., 2020, ApJ, 892, 146

Vulcani B., Poggianti B. M., Smith R., Moretti A., Jaffé Y. L., Gullieuszik M., Fritz J., Bellhouse C., 2022, ApJ, 927, 91

West M. J., Bothun G. D., 1990, ApJ, 350, 36